UNIVERSITÁ DEGLI STUDI DI ROMA
"TOR VERGATA"

FACOLTÁ DI SCIENZE MATEMATICHE, FISICHE E NATURALI

TESI DI DOTTORATO IN FISICA
XIX ciclo

Microscopic dynamics and excited state properties of liquid water

Viviana Garbuio

Relatori
Prof. Carla Andreani
Prof. Rodolfo Del Sole
Dott. Olivia Pulci
Dott. Roberto Senesi

Coordinatore del dottorato
Prof. Piergiorgio Picozza

Contents

Preface

Water is the major chemical constituent of our planet's surface and it is essential for living organism survival. About 65% of the human body weight is due to water, some tissues such as brain and lung being composed of nearly 80% water. Many biochemical and industrial processes occur in aqueous solution and the role of the solvent in the reactions is crucial.

Due to its ubiquity, we tend to consider water as a simple common substance but, for such a seemingly elementary molecule, the complexity of behaviour is astonishing and water is still surprisingly poorly understood.

The comprehension of the chemical and physical nature of water has been a long-standing goal of science, and liquid water continues to attract intense interest and motivate a large number of experimental and theoretical studies.

Recently, however, the theoretical studies of water [1, 2, 3, 4, 5, 6, 7, 8, 9, 10] have mostly focused on its structure and ground state properties whereas less effort has been dedicated to its electronic structure and optical absorption spectrum. As a consequence, experimental data about excited states are not yet completely understood. One of the purposes of the present work is hence to solve these issues by carrying out *ab-initio* many-body calculations of the electronic and optical properties of water.

Simultaneously, in the last years, great attention has been devoted to the study of water confined in different nanoporous systems, or in proximity of macromolecules and surfaces, because of its biological and technological importance (water in biology is always confined) [11, 12, 13, 14, 15, 16, 17, 18, 19, 20, 21, 22, 23]. It is well assessed that microscopic properties of confined water molecules differ from those in the bulk phase and the competition between water-water and water-confining medium interactions leads to the appearance of new interesting physical properties. Moreover, changes in both structural and dynamical properties occur. Up to now, however, there is no general theory predicting the behavior of confined liquids or the relative importance of surface interaction versus confinement.

The present work focuses on two complementary aspects of water: its excited state properties, very important in many chemical reactions and therefore fundamental to advance in many research fields, and the proton microscopic dynamics in confined water, which is interesting for many biological processes such as catalysis, protein folding

or ionic transport in membranes. These topics are faced with different investigative approaches, both theoretical and experimental. The electronic and optical properties of liquid water are studied with *ab-initio* theoretical calculations, taking into account both self-energy and excitonic effects in the framework of many-body perturbation theory. The study of the proton microscopic dynamics of confined water has been instead made with deep inelastic neutron scattering experiments, performed at the ISIS spallation neutron source.

This thesis is organized as follows: in the first chapter a brief introduction on water, with an overview of its principal properties and anomalies and their importance for life development and survival, is presented. Chapters 2-4 are devoted to the *ab-initio* study of the excited state properties of liquid water; in the second chapter we describe the theoretical methods at the base of our simulations, from Density Functional Theory to Many-Body perturbation theory and some hints on Time Dependent-Density Functional Theory. In chapter 3 we illustrate how to apply these methods to a liquid disordered system, such as water, and which approximations have been necessary. Chapter 4 is at last devoted to the presentation and discussion of the results obtained for electronic and optical properties of liquid water. Chapters 5-7 are instead related to the experimental work for the study of the proton microscopic dynamics in confined water. In chapter 5 we describe both the theoretical base for Deep Inelastic Neutron Scattering, especially the Impulse Approximation, and the experimental technique. In the sixth chapter we present the experiments performed on water confined in xerogel nanopores, looking at the sample properties and at the experimental instrumentation. Finally, in chapter 7, we show and discuss the results obtained for the proton momentum distribution in confined water. A conclusive chapter closes the thesis.

Chapter 1

Introduction

Water is one of the most common substances on earth, so familiar that it is often perceived as pretty ordinary. Despite the simplicity of its molecule (few molecules are smaller), it presents some fascinating unusual properties which seem to fit perfectly all the requirements for carbon-based life development and survival. In this chapter we will describe both the single water molecule, H_2O, and the properties and anomalies of liquid water, emphasizing their role in our planet balance.

1.1 Water molecule

The isolated water molecule is composed of two hydrogen atoms and one oxygen atom and has a very simple molecular formula: H_2O.

Its structure, schematically shown in figure 1.1, is non-linear with a bonding angle $\theta = 104.45°$; the O-H bonds length is $r_{OH} = 0.957\,\text{Å}$.

The molecular orbital configuration of water in its ground state is

$$(1a_1)^2(2a_1)^2(1b_2)^2(3a_1)^2(1b_1)^2 \tag{1.1}$$

where $1a_1$ corresponds to the oxygen 1s orbital and the others are mixed molecular orbitals; the lowest unoccupied molecular orbitals are the σ antibonding orbitals $4a_1$ and $2b_2$.

The water molecule is usually considered to have four sp^3-hybridized electron pairs, arranged in an approximately tetrahedral structure. Two of them are shared along the O-H bonds while the other four electrons form two lone pair orbitals on the oxygen atom, schematically depicted as grey clouds in figure 1.2. The strong repulsion among these two negative lone pairs give rise to the bending of the molecule, pushing the hydrogen atoms closer each other, and resulting in a bonding angle $\theta = 104.45°$ smaller than the perfect tetrahedral angle of 109.47 °. In the figure it is also shown that, due to these four unshared electrons, the water molecule has a negative charge near the

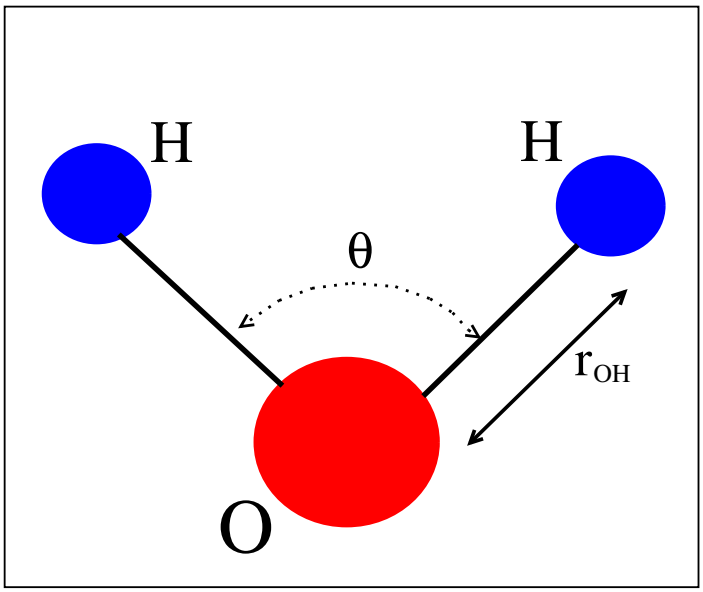

Figure 1.1: Schematic view of the isolated water molecule.

oxygen atom and a positive charge near the hydrogens. The uneven distribution of electron density makes the water molecule polar, with a dipole moment $\mu = 1.854$ D[1].

1.2 Liquid water

In order to describe liquid water, we have first to define the hydrogen bond. In general terms, we can say that a specific attraction is found between an electronegative atom (such as nitrogen, oxygen, fluorine and chlorine) and an hydrogen (or deuterium) atom, particularly when the latter is itself chemically bonded to other electronegative atoms. Hydrogen bonds have a strength (≈ 0.22 eV per atom) intermediate between covalent and van der Waals interactions and are strongly directional, meaning that the hydrogen bond, between one electronegative atom and one hydrogen atom, tend to be collinear with the bond between the hydrogen and the second electronegative atom. This is schematically shown, for the case of water molecules, in figure 1.3.

The water molecule, containing two hydrogen and one oxygen atoms in a non-linear arrangement, is ideally suited to engage in hydrogen bonding, with the possibility to act both as a donor and as an acceptor and hence with the potentiality to form four

[1] 1 D = 1 Debye = 3.3356 x 10^{-30}Cm

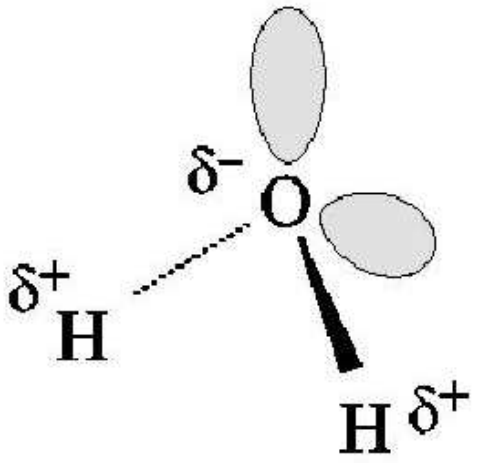

Figure 1.2: Schematic view of the water molecule; grey clouds are the lone pair orbitals. The partial charge transfer from the hydrogens to the oxygen atom is also indicated.

hydrogen bonds for each molecule, two from the hydrogens and two from the oxygen. Both in the liquid and in the solid phases, water molecules present two types of O-H interactions: strong covalent bonds within the single molecule and weaker hydrogen bonds between the molecules. Since the strength of the hydrogen bonds is about a tenth of the strength of the covalent ones, they are constantly broken and reformed in liquid water and a wide three-dimensional random network of hydrogen bonds, continuously changing, is formed (see the example in figure 1.3).

The striking number of unusual properties of liquid water may be largely ascribed exactly to its ability to form hydrogen bonds. Some of the more notable physical properties displayed by liquid water are the following:

1. negative volume of melting and density maximum along the coexistence curve at 4°C;

2. anomalously high specific heat;

3. anomalously high boiling point and evaporation heat, as shown in figures 1.4 and 1.5;

4. high dielectric constant and high mobility for H^+ and OH^- ions transport.

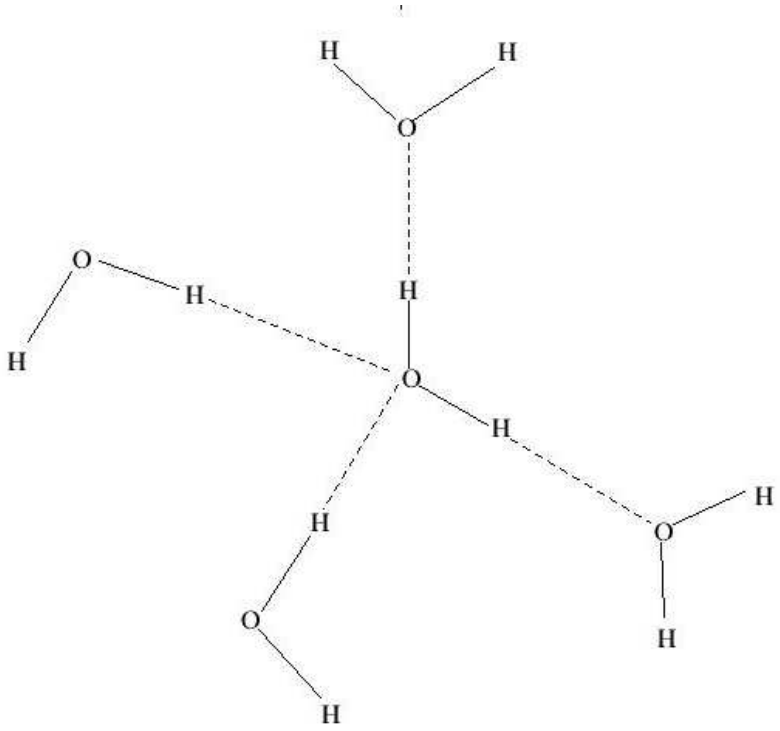

Figure 1.3: Example of hydrogen bonds network among water molecules. Continuous lines represent O-H covalent bonds within the H_2O molecules while dashed lines are O-H hydrogen bonds between water molecules.

In what follows, we describe the meaning and consequences of these properties:

1. Almost in all substances, the average distance among first neighbours tends to increase with increasing temperature and the solid phase has in general a higher density than the liquid one. This is not true for water/ice; due to the hydrogen bonds among molecules, both water and ice tend to have a tetrahedral structure. When ice is melting, this structure partially breaks and some water molecules can insert in the holes which are developing in this structure. Therefore with increasing temperature there are two opposite effects: the approach of the molecules causing an increase of the density and the usual increase of the average distance among neighbours which tend to decrease the density. Up to 4°C the first effect is dominant and the most evident consequence is that ice float on top of water. In nature, this property is fundamental because it allows ponds, lakes and seas to freeze on the top and to offer hospitable underwater conditions for aqueous life form.

2. The specific heat of water, 1.01 cal/g, is one of the highest among organic compounds. It is defined as the energy that has to be furnished to 1 g of matter to increase its temperature of 1 degree. This energy is generally used to break the bonds among molecules, but hydrogen bonds are stronger than van der Waals interactions and require a greater amount of energy. The high specific heat of water enables the oceans to stabilize the world's climate, because a great amount of heat is needed to change their temperature of just 1 degree.

3. Water has an anomalously high boiling point, 100 °C, and the highest evaporation heat of all known substances, 538 cal/g. This is again due to the strength of the hydrogen bonds among the molecules and makes water an excellent cooler. This property is also exploited by human body through the perspiration.

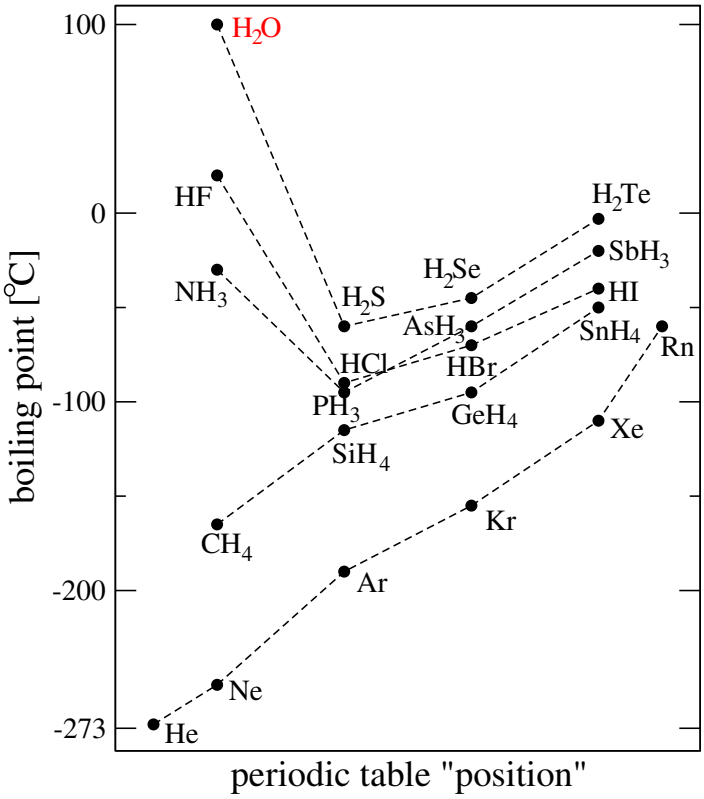

Figure 1.4: Boiling point of various RH_n molecules and of noble gases, as a function of the horizontal position of R in the periodic table.

4. The dielectric constant of liquid water, 81, is one of the highest among pure

liquids (except for formamide and cyanidric acid) and this allows the easy dissociation of polar molecules in solution. This property is mainly due to the polarity of the water molecule, with a partial charge transfer from the hydrogens to the oxygen. Related to the high value of the dielectric constant, water tends also to ionize giving rise to H_2OH^+ and OH^- ions and promoting the mobility of ions and the occurance of chemical reactions.

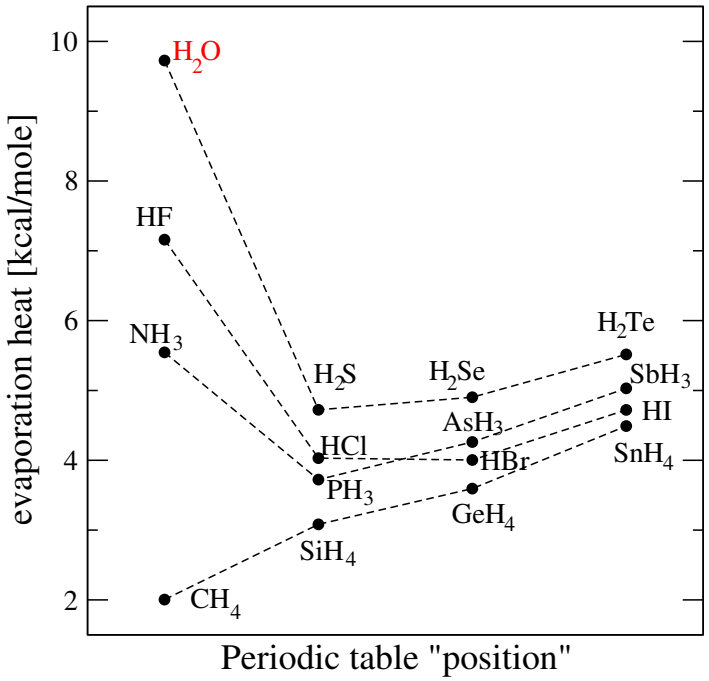

Figure 1.5: Evaporation heat of various RH_n molecules and of noble gases, as a function of the horizontal position of R in the periodic table.

Many other singular properties, together with their importance for life on our planet, make water a fascinating substance but, in spite of much work, many of these properties are still puzzling and lots of work, both theoretical and experimental is still to be done. The aim of the thesis is to do some of this work by studying the proton microscopic dynamics of confined water by neutron scattering experiments and the excited state properties of liquid water by theoretical *ab-initio* calculations.

Chapter 2

First principles theoretical methods

In this chapter we review the theoretical methods employed in this thesis work for the calculations of the excited state properties of liquid water. We will first describe the density functional theory which is an exact theory for ground state calculations but is also a common starting point for other ab-initio methods. Then we will show the need to go beyond density functional theory in order to describe excitations in materials. We will illustrate the many body perturbation theory, from the basic Green's functions formalism, through the so-called GW approximation, up to the Bethe-Salpeter equation, which gives good results for neutral excitation spectra. At the end of the chapter, we will also introduce the time-dependent density functional theory, that represents an alternative method to obtain excited state properties, computationally less expensive but not yet as reliable as many body perturbation theory.

2.1 Density functional theory

Density Functional Theory (DFT) aims to solve the many-body ground state problem in terms of the one-particle electronic density alone. The first attempts to study solid state problems focusing the attention on density functionals are ascribed to Thomas and Fermi [24]-[25] and date back to 1927-1928.
The seminal paper of Hohenberg and Kohn [26] of 1964 and the following work of Kohn and Sham [27] of 1965 lay the foundations for the density functional theory and in 1998 the importance of their work was acknowledged with the nobel prize for chemistry to Kohn. For a detailed review on DFT see, for example, [28].

2.1.1 The many-body problem

A system of interacting particles, both electrons and ions, in the non-relativistic regime (relativistic effects are negligible in the range of energy of interest), is described by the many-body Hamiltonian (in atomic units $e = m = \hbar = 1$):

$$H = \sum_I -\frac{1}{2}\nabla_I^2 + \sum_i -\frac{1}{2}\nabla_i^2 + \frac{1}{2}\sum_{I\neq J}\frac{Z_I Z_J}{|\mathbf{R}_I - \mathbf{R}_J|} + \frac{1}{2}\sum_{i\neq j}\frac{1}{|\mathbf{r}_i - \mathbf{r}_j|} + \sum_{i,I}\frac{-Z_I}{|\mathbf{r}_i - \mathbf{R}_I|}, \quad (2.1)$$

where the capital indices refer to ions and the small ones refer to electrons. The terms of this Hamiltonian represent, in the order, the kinetic energies of the ions and electrons and the interaction among the ions, among the electrons and between ions and electrons. The knowledge of the eigenvalues and eigenstates of this Hamiltonian is a very complex task, impracticable for realistic systems.
The first important simplification comes from the Born-Oppenheimer approximation [29]: being the ion masses much greater (three orders of magnitude) than the electron ones, for each ionic configuration electrons can be considered in their ground state. In other words, the dynamic of ions and electrons is in well separated range of energies and therefore the ionic and electronic degrees of freedom can be decoupled. This leads to a simplified electronic Hamiltonian of the form:

$$H = \sum_i -\frac{1}{2}\nabla_i^2 + V_{ext}(\mathbf{r}_i, \{\mathbf{R}_I\}) + \frac{1}{2}\sum_{i\neq j}\frac{1}{|\mathbf{r}_i - \mathbf{r}_j|} = T + V_{ext} + W_{e-e}; \quad (2.2)$$

we still have the electrons kinetic energy and the electron-electron interaction while the other terms are grouped in the external potential where the ionic coordinates appear just as parameters.
Anyway, finding eigenvalues and eigenstates of this Hamiltonian is still an impossible task for complex systems, out of the present computers power. In order to obtain some knowledge about the many-body problem it is therefore required to introduce some other approximation. One appealing approach is to reduce the problem to the study of a single particles Hamiltonian. In this context we have the Hartree [30] and the Hartree-Fock [31] methods. Also the density functional theory, which is an exact theory for ground state calculations, can be considered in this single particles framework.

2.1.2 Hohenberg and Kohn theorem

The basis of density functional theory are in the Hohenberg and Kohn theorem [26]. It was originally formulated for a many fermions system subject to local, spin-independent external potentials and for non-degenerate ground states. It affirms that, for a non-relativistic, time independent Hamiltonian of the form

$$H = T + V + W, \quad (2.3)$$

the external potential is a unique functional of the electronic density and therefore, once the mutual interaction among electrons is fixed, citing the original words of Hohenberg and Kohn,

the full many particle ground state is a unique functional of $n(\mathbf{r})$.

To sum up, we will prove that the ground state density determines the entire Hamiltonian of the system and that the energy functional, once the external potential is fixed, has its minimum just at the ground state density.
The demonstration of this statement is now given only for the case of a non degenerate ground state; an extension to degenerate ground states can be found in [28].

Let's assume that in the Hamiltonian given by eq.(2.3), the external potential V belongs to a set of local, one-particle potentials, $\mathcal{V}$, that lead to non-degenerate ground states for the problem

$$H|\psi\rangle = E_{gs}|\psi\rangle. \tag{2.4}$$

If we collect all the ground states in the set Ψ, we can define, through the solution of eq.(2.4), a map between the sets $\mathcal{V}$ and Ψ

$$C : \mathcal{V} \to \Psi; \tag{2.5}$$

this map is surjective by construction.
Then we can calculate the ground state densities $n(\mathbf{r})$ for each element of the set Ψ by

$$n(r) = N \int \psi^*(r, r_2, ..., r_N)\psi(r, r_2, ..., r_N)dr_2...dr_N, \tag{2.6}$$

and collect them in a new set $\mathcal{N}$; trivially we can define a second surjective map

$$D : \Psi \to \mathcal{N}. \tag{2.7}$$

To affirm that the ground state density univocally determines the Hamiltonian of the system we have to demonstrate that the two maps C and D are also injective and, hence, fully invertible.
Let's start by proving the invertibility of the map C; we can suppose that two different potentials (that differ by more than a constant) lead to the same ground state:

$$\begin{gathered} V \neq V' + \text{const} \\ H|\psi\rangle = (T + W + V)|\psi\rangle = E_{gs}|\psi\rangle \\ H'|\psi\rangle = (T + W + V')|\psi\rangle = E'_{gs}|\psi\rangle. \end{gathered} \tag{2.8}$$

Since the potentials are just multiplicative operators and the states ψ are not zero on a set of positive measure[1], by subtraction we obtain

$$(V - V')|\psi\rangle = (E_{gs} - E'_{gs})|\psi\rangle \Rightarrow V - V' = E_{gs} - E'_{gs} \tag{2.9}$$

or rather that the potentials differ just for a constant, in contradiction with our hypothesis. This proves that C is invertible.
We have now to prove that also the map D is fully invertible; we will start from the hypothesis $\psi \neq \psi'$ and show that $n(r)$ must be different from $n(r')$.
From the variational principle we have

$$E_{gs} = \langle\psi|H|\psi\rangle < \langle\psi'|H|\psi'\rangle = \langle\psi'|H' + V - V'|\psi'\rangle = E'_{gs} + \int n'(r)(v(r) - v'(r))d^3r$$
$$\Downarrow$$
$$E_{gs} < E'_{gs} + \int n'(r)(v(r) - v'(r))d^3r. \tag{2.10}$$

In the same way, starting with E'_{gs}, we get:

$$E'_{gs} < E_{gs} + \int n(r)(v'(r) - v(r))d^3r. \tag{2.11}$$

If we assume that different states $\psi \neq \psi'$ lead to the same electronic density $n(r) = n'(r)$, by adding term by term eq.(2.10) and (2.11), we obtain

$$E_{gs} + E'_{gs} < E'_{gs} + E_{gs} \tag{2.12}$$

that is an obvious contradiction.
We have just demonstrated that the electronic density of the system determines the external potential and thus, since the kinetic energy and the electron-electron interaction are specified, the entire Hamiltonian.

The second part of the Hohenberg and Kohn theorem establishes the variational character of the energy functional: since the map D between the densities and the eigenfunctions, does not depend on the external potential, if V_0 is the potential of a system with ground state energy E_0 and ground state density $n_0(r)$, the variational principle guarantees that

$$E_0 = E_{V_0}[n_0] < E_{V_0}[n] \qquad \text{for} \quad \text{each} \qquad n \neq n_0; \tag{2.13}$$

the ground state energy can therefore be obtained by minimizing the energy functional over all the possible densities

$$E_0 = \min_{n \in \mathcal{N}} E_{V_0}[n]. \tag{2.14}$$

[1]This is valid for well behaved potentials; rigorously on the Hilbert space of potentials $\mathcal{V} = L^{3/2} + L^{\infty}$ [32].

There is also another consequence of the independence of the map D from the external potential: the energy functional can in fact be divided in two parts

$$E_{v_0}[n] = \langle\psi[n]|T + W|\psi[n]\rangle + \int V_0(r)n(r)d^3r = F_{HK}[n] + \int V_0(r)n(r)d^3r; \quad (2.15)$$

the last part of the Hohenberg and Kohn theorem affirms that F_{HK} is a universal functional of the density, n, independent on the fixed external potential V_0.

The three fundamental assertions of the theorem concern the invertibility, the variational character of the energy functional and the universality of the functional F_{HK}; however, for many-body realistic systems, this functional is not known and its explicit construction is only possible with some approximations.

2.1.3 Thomas-Fermi equation

We pointed already out that the main limit of the Hohenberg and Kohn theorem is that the energy functional $E[n]$ is not explicitly known. In this section we will show how a particular choice of the energy functional leads to the Thomas-Fermi equation. In the Thomas-Fermi approximation we neglect the exchange and correlation effects in the electron-electron interaction, and consider the kinetic energy of the system as that of a free-electron gas:

$$W = \frac{1}{2}\int \frac{n(\mathbf{r})n(\mathbf{r}')}{|\mathbf{r}-\mathbf{r}'|}d\mathbf{r}d\mathbf{r}', \quad (2.16)$$

$$T = C\int [n(\mathbf{r})]^{5/3}d\mathbf{r}, \quad (2.17)$$

with $C = \frac{3}{10}(3\pi^2)^{2/3}$.
By minimizing the total energy functional $E_V[n] = T + V + W$ with the constraint of constant number of particles (through the Lagrange multiplier μ)

$$\delta\left(E_V[n] - \mu\int n(\mathbf{r})d\mathbf{r}\right) = 0, \quad (2.18)$$

we obtain the Thomas-Fermi equation

$$\frac{5}{3}C(n(\mathbf{r}))^{2/3} + V(\mathbf{r}) + \int d\mathbf{r}'\frac{n(\mathbf{r}')}{|\mathbf{r}-\mathbf{r}'|} - \mu = 0. \quad (2.19)$$

The Thomas-Fermi theory is based on the "right" variable, that is the electronic density, but it is not able to bind atoms in molecules nor to describe their shell structure and therefore it is not usable for realistic system calculations.

2.1.4 Kohn and Sham single particle equations

One year after the publication of the Hohenberg and Kohn work, Kohn and Sham proposed a single particle scheme to obtain the ground state density and total energy [27]. Using the Hohenberg and Kohn approach they obtained a set of self-consistent single particle equations where the various contributions to the total energy are separated and the only approximation must be introduced for the exchange and correlation interaction.
We can start the derivation of the Kohn and Sham equations by separating the total energy functional contribution

$$E_I[n] = T_I[n] + \int d\mathbf{r} n(\mathbf{r}) v_I(\mathbf{r}) + W[n] = \int d\mathbf{r} n(\mathbf{r}) v_I(\mathbf{r}) + E_H[n] + G[n], \tag{2.20}$$

where E_H is the Hartree energy and the index I refers to the fact that we are dealing with interacting particles; for the moment $G[n]$ is just an unknown functional.
Let's now introduce an auxiliary system of non-interacting (index NI) particles, described by the Hamiltonian

$$H_{NI} = T_{NI} + V_{NI}, \tag{2.21}$$

having the same density of the interacting system. According to the Hohenberg and Kohn theorem, there will exist just one external potential of the non-interacting system leading to a ground state density equal to the one of the interacting system:

$$V_{NI} \rightarrow \psi_{i(NI)} \rightarrow n_{NI} = \sum_i |\psi_{i(NI)}|^2 = n_I. \tag{2.22}$$

In the Kohn and Sham scheme we exploit the kinetic energy of the non-interacting system to separate also the functional $G[n]$ in two contribution:

$$E_I[n] = \int d\mathbf{r} n(\mathbf{r}) v_I(\mathbf{r}) + E_H[n] + T_{NI}[n] + E_{xc}[n]; \tag{2.23}$$

E_{xc} contains the difference between the kinetic energies of the interacting and non-interacting systems and the exchange and correlation contributions to the total energy. However, for an arbitrary system, E_{xc} is unknown and must be approximated in some way.
Following the Hohenberg and Kohn variational principle we can now minimize the energy functional with respect to the density:

$$\frac{\delta E_I}{\delta n} = v_I + \frac{\delta E_H}{\delta n} + \frac{\delta T_{NI}}{\delta n} + \frac{\delta E_{xc}}{\delta n}. \tag{2.24}$$

Defining the exchange and correlation potential $v_{xc} = \frac{\delta E_{xc}}{\delta n}$ and the Hartree potential $v_H = \frac{\delta E_H}{\delta n}$, we obtain the Kohn and Sham set of self-consistent equations

$$[-\tfrac{1}{2}\nabla^2 + v_I + v_H + v_{xc}]\phi_i(\mathbf{r}) = \varepsilon_i \phi_i(\mathbf{r}), \tag{2.25}$$

$$n(r) = \textstyle\sum_i f_i |\phi_i(\mathbf{r})|^2, \tag{2.26}$$

where f_i is the occupation number of the state i.
The main idea of the Kohn and Sham scheme is therefore to replace the problem of an interacting particles system with a simpler fictitious non-interacting system whose Hamiltonian is characterized by a potential

$$v_{KS} = v_I + v_H + v_{xc}. \tag{2.27}$$

It's important to stress that this potential depends on the density, hence the equations (2.25) and (2.26) must be solved in a self-consistent way.

2.1.5 Approximations for the exchange-correlation energy

In the previous section we derived the Kohn and Sham equations characterized by the potential (2.27); we also said that, for an arbitrary system, E_{xc} and hence v_{xc} are unknown and must be approximated in some way. We will now describe two possible approximations for the exchange and correlation potentials, that have been used in this thesis: the local density approximation (LDA), first proposed in the original work of Kohn and Sham [27], and the generalized gradient approximation (GGA) [33]-[34].

In the local density approximation, the exchange and correlation energy is given by

$$E_{xc}^{LDA} = \int d\mathbf{r}\; n(\mathbf{r})\; \epsilon_{xc}^{heg}(n(\mathbf{r})), \tag{2.28}$$

where ϵ_{xc}^{heg} is the exchange and correlation energy per electron of an homogeneous electron gas of density $n(\mathbf{r})$; we see that, in this approximation, the exchange and correlation potential depends only on the local value of the density.
In actual calculations ϵ_{xc}^{heg} is taken from tables obtained with accurate Monte Carlo simulations of the homogeneous electron gas for different constant densities $n(\mathbf{r})$ [35],[36].

The local density approximation is valid, in principle, only for systems with slowly varying densities however, surprisingly, it turns out to be accurate and to give favorable ground-state results also for highly inhomogeneous systems such as atoms and molecules or even more complex systems. This can be partially attributed to the fact that it satisfies the correct sum rule for the exchange and correlation hole[2](for a detailed derivation see [28]).

[2]The exchange and correlation hole represents a negative electronic density corresponding to the fact that each electron repels the others creating a sort of hole around itself.

One can imagine that a way to improve the local density approximation is to consider also the variations of the density by adding gradient corrections. Unfortunately this approximation, known as Gradient Expansion Approximation [37], yields worse results than LDA because its exchange and correlation functionals do not obey the sum rule for the exchange and correlation hole [38]. To go beyond LDA, we can introduce new functionals, called Generalized Gradient Approximation functionals, of the form

$$E_{xc}^{GGA} = \int d\mathbf{r} f(n(\mathbf{r}), \nabla_r n), \tag{2.29}$$

that are built taking care that the sum rule for the exchange and correlation hole is satisfied. For many realistic systems, the use of these functionals turns out in an appreciable improvement of the results of calculations, particularly for lattice constants estimation. Anyway, this is not always the case and there are some systems, for instance graphite, which are better described by LDA potentials.

2.1.6 Further approximations

When performing real calculations, further approximations must be introduced.
The electronic wavefunctions of a periodic system can be expressed, thanks to the Bloch theorem [39], as a sum of plane waves of the form

$$\psi_{n,\mathbf{k}}(\mathbf{r}) = \sum_{\mathbf{G}} c_{n,\mathbf{k}+\mathbf{G}}\ e^{i(\mathbf{k}+\mathbf{G})\mathbf{r}}, \tag{2.30}$$

where $\mathbf{k}$ is a vector of the reciprocal lattice that covers the first Brillouin zone and $\mathbf{G}$ is a reciprocal lattice vector.
In principle, both the $\mathbf{k}$ points and the $\mathbf{G}$ vectors must be infinite but it is obviously impossible in real calculations.
What is done in practice is to perform a summation just on a finite number of $\mathbf{k}$-points, "representative" of the entire Brillouin zone, and to limit the summation over the $\mathbf{G}$ vectors up to a fixed value.
To illustrate the first point we can imagine that the wavefunctions for $\mathbf{k}$-points close to each other in a region of the Brillouin zone are almost identical and can therefore be replaced by just one wavefunction for the entire region. Obviously a good convergency on the $\mathbf{k}$-points set has to be reached. Fortunately, there are some special sets that, thanks to the symmetry of the system, well represent all the first Brillouin zone, even with a small number of $\mathbf{k}$-points [40]-[41].
To limit the summation over the $\mathbf{G}$ vectors we take advantage from the fact that the most important contributions in the wavefunction expansion come from the plane-waves with the smaller kinetic energy associated. We therefore truncate the expansion by introducing an energy cut-off E_{cut} and considering just the plane-waves with kinetic

energy below this threshold

$$\frac{1}{2}|\mathbf{k}+\mathbf{G}|^2 \leq E_{cut}. \tag{2.31}$$

With a careful **k**-point sampling and the introduction of the energy cut-off E_{cut}, the Kohn and Sham equations seem to be tractable. Unfortunately there is also another practical problem: a plane-waves basis set is in fact unsuitable for describing the rapidly oscillating wavefunctions of the core electrons. Anyway, the most physical properties of solids come from the valence electrons rather than the inner ones, and the core wavefunctions are almost the same in different chemical frameworks. For this reason, it is possible to introduce a further approximation that is the use of pseudopotentials[3]: we replace the core electrons and the strong nuclear potential with a weaker effective pseudopotential of the positive ion and, in this way, we simultaneously get rid of the singularity of the nuclear potential, of the very localized core electrons and also of the nodes of the valence wavefunctions (otherwise needed for the orthogonality to the core wavefunctions).
Pseudopotentials are usually constructed through the inversion of the Schrödinger equation for the pseudo-atom and must obey some conditions:

1. beyond a certain 'core' radius r_c, the original potential must be recovered,
2. beyond the same r_c, the valence pseudo-wavefunctions must be equal to the ones of a reference configuration, such as the neutral free atom,
3. below r_c the pseudo-wavefunctions must not have any node,
4. the valence states energies must be equal for the pseudo-atom and the real atom,
5. the pseudopotential must be transferable, i.e. it has to represent the valence electrons for different chemical environments.

2.1.7 Excited states in DFT

A last comment about density functional theory regards the fact that, after solving the Kohn-Sham equations, one can be tempted to give a physical interpretation both to the Kohn and Sham orbitals and eigenvalues as excited states and excitation energies of the real system. This is not the case, in fact the Kohn and Sham eigenvalues in eq.(2.25) are just Lagrange multipliers and their interpretation as excitation energies of the real system has no foundation.
In spite of this, Kohn and Sham solutions are often used to have a first insight on the excited state properties of real systems. This leads to the well known band gap problem

[3]This kind of effective potentials first appear in 1934 [42] and 1959 [43]; for details on "modern" pseudopotential see [44]-[45].

of DFT: the band gaps predicted by the theory are typically 30-50% (sometimes even more) smaller then the experimental ones. For what concern the absorption spectra, we can use the Kohn and Sham solutions through the one-electron approximation of the Fermi's golden rule:

$$\varepsilon_2 \propto \sum_{v,c} |\langle \phi_c | e^{i\mathbf{qr}} | \phi_v \rangle|^2 \delta(\omega - (\varepsilon_c - \varepsilon_v)). \tag{2.32}$$

This approximation, in spite of its simplicity, can sometimes lead to descriptions of the electronic spectra in qualitative and quantitative agreement with the experimental ones (especially for electron energy loss spectra[46]); more often it provides just a first indication on the absorption spectra of materials.

2.2 Many body Green's functions approach

In the previous section we have described the density functional theory which is a very powerful tool to study ground state properties. However, if we want to interpret or even predict spectroscopic experiment results, we have to study the system in its excited states. Photoemission (both direct and inverse), electron-energy loss and optical absorption will be the reference experiments we would like to describe.
In direct photoemission an electron is ejected from the system and, if one considers this electron as being completely decoupled from the sample, from the energy and momentum conservation one can obtain information about the energy level that "was occupied" by that electron, i.e. the energy level of the hole. On the contrary, inverse photoemission yields information about the unoccupied states. In absorption experiments there is not a change in the total number of electrons: the excited electron remains inside the system and interacts with the hole; hence the two particles cannot be treated separately and the joint density of states must be considered. Also in electron-energy loss experiments the electrons impinge on the sample and lose their energy by exciting electron-hole pairs, plasmons and other high-order multipair excitations. Therefore, all these spectroscopic techniques, excite the system and look at its response.

In the last paragraph, we have emphasized the necessity to go beyond DFT in order to successfully describe excited state properties of materials. This is exactly the aim of Time Dependent Density Functional Theory (TDDFT), which will be described in the following section, and of Green's functions theory that is the matter of this section (details on this technique can be found in many textbooks[47]-[48] and reviews[49],[50]).

2.2.1 The Green's functions: basic theory

The single particle Green's function is defined as

$$G(1,2) = -i\langle N|\mathcal{T}\{\widehat{\psi}(1)\widehat{\psi}\dagger(2)\}|N\rangle, \tag{2.33}$$

where $|N\rangle$ is the ground state of a N particles system, $\mathcal{T}$ is the time ordering operator, $\widehat{\psi}(i)$ $(i = 1, 2)$ are field operators in the Heisenberg picture and in the index i are included the five coordinates (position $\mathbf{r_i}$, spin σ_i and time t_i; x_i includes both the position and the spin coordinates) of the i-th particle.
$\widehat{\psi}\dagger(i)|N\rangle$ represents a $(N+1)$-particles system in which an electron has been added in $\mathbf{r_i}$ at time t_i; the Green's function is also called propagator because for $t_1 > t_2$ it gives the probability amplitude to find an electron in $\mathbf{r_1}$ at time t_1 when an electron has been added to the system in $\mathbf{r_2}$ at time t_2 and viceversa, for $t_2 > t_1$, it represents the propagation of a hole.

Depending on the time ordering, we can insert a complete set of $(N+1)$ or $(N-1)$ particles states and perform a Fourier transform in time domain. In this way we obtain the Lehmann representation of the Green's function:

$$G(x_1, x_2, \omega) = \sum_s \frac{f_s(x_1) f_s^*(x_2)}{\omega - \epsilon_s - i\eta \mathrm{sgn}(\mu - \epsilon_s)}, \tag{2.34}$$

where μ is the Fermi energy of the system, s runs over the $(N+1)$ or $(N-1)$ particles excited states and

$$\begin{cases} f_s(x_i) = \langle N|\widehat{\psi}(x_i)|N+1, s\rangle & \text{and} \quad \epsilon_s = E(N+1, s) - E(N) \quad \text{when} \quad \epsilon_s > \mu \\ f_s(x_i) = \langle N-1, s|\widehat{\psi}(x_i)|N\rangle & \text{and} \quad \epsilon_s = E(N) - E(N-1, s) \quad \text{when} \quad \epsilon_s < \mu \end{cases} \tag{2.35}$$

η is an infinitesimal positive number needed for the convergence of the Fourier transform.
In this representation it can be seen that the poles of the Green's function are exactly the electron addition and removal energies, that is the energy levels of unoccupied and occupied states respectively.

2.2.2 Quasi-particle equation

We can now start from the Lehmann representation of the Green's function given in eq.(2.34) and take just its imaginary part; we obtain the so called *spectral function*:

$$A(x_1, x_2, \omega) = \left|\frac{1}{\pi}\mathcal{I}m(G(x_1, x_2, \omega))\right| = \sum_s f_s(x_1) f_s^*(x_2)\delta(\omega - \epsilon_s). \tag{2.36}$$

In the case of non-interacting particles only the states $|N+1, s\rangle = c_s^\dagger |N\rangle$ (where $c_s^\dagger$ is a creation operator) give non-zero Lehmann amplitudes and the spectral function consists in a series of δ-functions in correspondence of the Lehmann energies, i.e. at the eigenvalues of the non-interacting Hamiltonian. Each peak hence corresponds to a single particle state.
For interacting systems the states $|N+1, s\rangle$ or $|N-1, s\rangle$ are instead linear combinations of many one-electron wavefunctions and there will be more non-vanishing contributions to the spectral function. However, these contributions merged together can form, also for interacting systems, some kind of structure, as shown in fig. 2.1. These structures

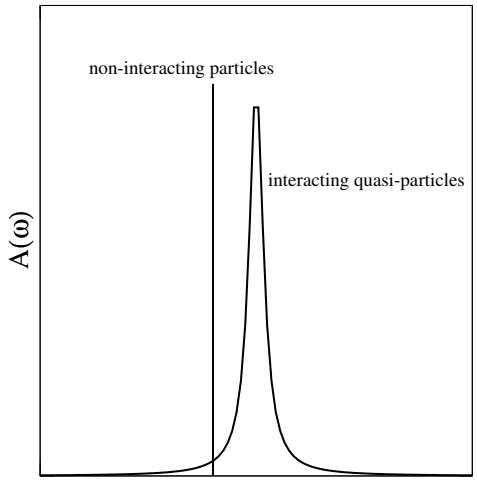

Figure 2.1: Schematic view of the spectral functions for a non-interacting system (the δ-peak) and for an interacting one. The quasi-particle peak has a different position (the energy of the quasi-particle) and a finite width (linked to the finite lifetime of the quasi-particle).

can be thought to derive from the δ-functions of the non-interacting system but they have different positions and a finite width. In this case we still are in a particle-like framework and we talk of *quasi-particles*. Quasi-particles can be thought as real particles plus a cloud of electron-hole pairs surrounding them and screening the mutual interaction; they are not eigenstates of the real Hamiltonian and hence they have finite lifetimes (connected to the finite width of the relative peak).
The differences between "bare" particles (subject only to the Hartree potential) and quasi-particles can be accounted for by a new operator, called self-energy, Σ. It is a non-local, non-hermitian, energy-dependent operator which includes the Fock exchange and all the remaining correlation effects.
If we consider the Hartree Hamiltonian as the non-interacting Hamiltonian H_0 and

suppose to know the new operator Σ, we can write a Schrödinger-like equation for the quasi-particles:

$$H_0(x_1)\psi_n(x_1,\omega) + \int dx_2 \Sigma(x_1,x_2,\omega)\psi_n(x_2,\omega) = E_n(\omega)\psi_n(x_1,\omega), \tag{2.37}$$

where $H_0(x_1) = -\frac{1}{2}\nabla_1^2 + V_{ext}(x_1) + V_H(x_1)$.
The Green's function can be written as:

$$G(x_1,x_2,\omega) = \sum_n \frac{\psi_n(x_1,\omega)\psi_n^*(x_2,\omega)}{\omega - E_n(\omega)}; \tag{2.38}$$

its poles are at the energies that obey the equation $E_n(\omega) = \omega$ and can be obtained by solving eq.(2.37).
We have achieved a single-particle picture to solve the interacting problem but at the price of the introduction of a non-local, non-hermitian, energy-dependent operator. This means that the entire Hamiltonian is not hermitian, hence the $\psi_n(x_1,\omega)$ form a complete set but are energy-dependent and not necessarily orthogonal; moreover the $E_n(\omega)$ are in general complex.

As a last comment, we want to stress that the quasi-particle equation reduces to the Hartree equations for Σ=0, to the Hartree-Fock equation for $\Sigma = iGV$, and to the Kohn-Sham equation when Σ is replaced by $V_{xc}^{KS}(r)$. This last consideration can explain the qualitative agreement between DFT results and experimental energy levels: Kohn-Sham equations already take into account exchange and correlation effects, even if in an approximate way, and the exchange and correlation potential, $V_{xc}^{KS}(r)$, can be a good approximation for Σ.

2.2.3 Hedin's equations

We just said that we have achieved a single-particle equation to solve the interacting problem but at the price of the introduction of a non-local, non-hermitian, energy-dependent operator, Σ. Now we have to find an adequate expression for this operator.

From the Heisenberg equation of motion for the field operator $\hat{\psi}$

$$i\frac{\partial\hat{\psi}}{\partial t} = [\hat{\psi}, H] \tag{2.39}$$

we can derive the equation of motion for the Green's function:

$$\left[i\frac{\partial}{\partial t_1} - H_0(1)\right] G(1,2) - \int d3\ \Sigma(1,3)G(3,2) = \delta(1,2) \tag{2.40}$$

where H_0 is the Hamiltonian of eq. (2.37).
In the same way, for the non-interacting system we have

$$\left[i\frac{\partial}{\partial t_1} - H_0(1)\right] G_0(1,2) = \delta(1,2). \tag{2.41}$$

From the equations (2.40) and (2.41) it can be derived a Dyson like equation for the Green's function:

$$G(1,2) = G_0(1,2) + \int d(34)\; G_0(1,3)\Sigma(3,4)G(4,2). \tag{2.42}$$

This is the first equation of a close set of five equations proposed by Hedin[51],[52] in 1965, which allow to obtain the self-energy in an iterative way and to solve exactly (at least in principle) the many-body problem.
The other four coupled integral equations are:

$$\Sigma(1,2) = i \int d(34)\; G(1,3)\Gamma(3,2,4)W(4,1^+); \tag{2.43}$$

$$W(1,2) = V(1,2) + \int d(34)\; W(1,3)P(3,4)V(4,2); \tag{2.44}$$

$$P(1,2) = -i \int d(34)\; G(1,3)G(4,1^+)\Gamma(3,4,2); \tag{2.45}$$

$$\Gamma(1,2,3) = \delta(1,2)\delta(1,3) + \int d(4567)\; \frac{\delta\Sigma(1,2)}{\delta G(4,5)}\; G(4,6)G(7,5)\Gamma(6,7,3); \tag{2.46}$$

where 1^+ stands for $(\mathbf{r}_1, \sigma_1, t_1 + \delta)$ and δ is an infinitesimal positive number. Together with the Green's function and the self-energy operator, this set of equations involve also the time ordered polarization operator $P(1,2)$, the dynamical screened Coulomb interaction $W(1,2)$ and the vertex function $\Gamma(1,2,3)$.

The Hedin's equations have the appealing characteristic to highlight the important ingredients of the many-body physics. In fact, the response of the system to the addition or removal of one particle is given by the polarization operator which contains two Green's functions (pairs of particle-hole) but contains also the vertex function, Γ. The vertex function yields information about the interaction between the particle and the hole and it is determined by the change of the "induced potential" Σ with respect to G.
Also the use of a screened potential is physically more adequate then using the potential V: a perturbative expansion in terms of the bare Coulomb potential will lead to convergency problems which arise from the strength of this kind of interaction while the effective screened potential W, by which the particles interact, is much weaker and does not lead to this kind of convergency problems.

2.2.4 The GW approximation

The Hedin's equations together with the Dyson's one for the Green's function form a set of equations that must be solved self-consistently. This leads in principle to the

exact solution, but it is practically impossible for realistic systems and one has to face the problem of finding some simplifications of the Hedin's equations. The simplest approximation consists in starting with a non-interacting system by putting $\Sigma = 0$; in this case the Green's function is simply G_0, the vertex correction are neglected with $\Gamma(1,2,3) = \delta(1,2)\delta(2,3)$ and the irreducible polarizability is given by non-interacting quasi-electron quasi-hole pairs $P(1,2) = -iG_0(1,2)G_0(2,1^+)$ (this independent particle polarizability is also called Random Phase Approximation (RPA) polarizability). With this first iteration step the self-energy becomes

$$\Sigma(1,2) = iG_0(1,3)W_0(3,1); \tag{2.47}$$

this is the so-called GW approximation which was firstly introduced by Hedin[51] in 1965. The Green's function can now be evaluated from the Dyson's equation (2.42). In principle more iterations should be performed but real calculations usually stop at this first step.

As a starting point for self-energy calculation, instead of using the Hartree Green's function G_0 and screening W_0, the most common choice is the use of Kohn and Sham results; the Green's function is therefore given by:

$$G_0(x_1, x_2, \omega) = \sum_{n,k} \frac{\phi^{KS}_{nk}(x_1)\phi^{*KS}_{nk}(x_2)}{\omega - \varepsilon^{KS}_{nk} + i\eta \mathrm{sgn}(\varepsilon^{KS}_{nk} - \mu^{KS})}. \tag{2.48}$$

Once G_0 has been obtained, we can calculate the RPA polarizability P_0 and screening W_0 and the self-energy Σ from eq. (2.47). This self-energy can hence be used in the quasi-particle equation (2.37).
The similarity of equations (2.37) and (2.25) leads to treat the problem in a perturbative way respect to the difference between the self-energy and the Kohn and Sham exchange and correlation potential and to consider, at the first order, the quasi-particle energies as[4]:

$$E_n(\omega) = \varepsilon_n + \langle \phi^{KS}_n | \Sigma(E_n) - v^{KS}_{xc} | \phi^{KS}_n \rangle. \tag{2.49}$$

Then the usual way to proceed is to expand the self-energy at the first order around ε_n:

$$\langle \Sigma(E_n) \rangle = \langle \Sigma(\varepsilon_n) \rangle + (E_n - \varepsilon_n) \left\langle \frac{\partial \Sigma(\omega)}{\partial \omega} \right\rangle_{\omega = \varepsilon_n} + \dots \tag{2.50}$$

and calculate the GW corrections to the Kohn and Sham energies:

$$E_n - \varepsilon_n = \Delta\varepsilon^{QP}_n = \frac{\langle \Sigma(\varepsilon_n) \rangle - \langle v^{KS}_{xc} \rangle}{1 - \left\langle \frac{\partial \Sigma(\omega)}{\partial \omega} \right\rangle_{\omega = \varepsilon_n}}. \tag{2.51}$$

[4]It has been shown [53],[54] that the quasi-particle wavefunctions and the Kohn and Sham ones are similar for many materials; however this is not true for some cases like the (110) surface of GaAs [55], or SiH_4, [56] and particular care must be taken for every non-bulk system[49].

To summarize, the usual way to calculate electronic excitation energies consists of three steps:

1. DFT calculations of ground state energies and wavefunctions;
2. construction of G_0^{KS} and calculations of the RPA polarizability P_0, of the screening W_0 and of the self-energy Σ_{GW};
3. calculation of the GW corrections to obtain the quasi-particle energies.

This is the standard GW approximation and, even if it is just the first iteration of Hedin's equation, quite accurate results for one-particle excitations are obtained and the underestimation of the band gap, peculiar of DFT, is usually removed, as shown in fig. 2.2.

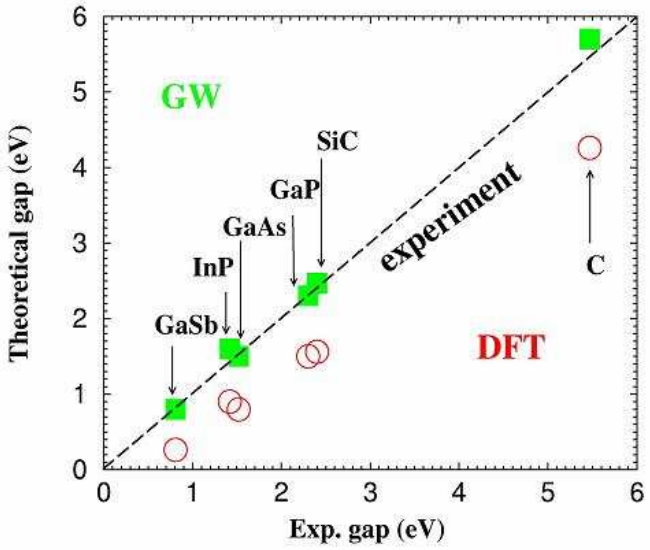

Figure 2.2: DFT (red circles) and GW (green squares) band gaps of different materials, in units of the experimental gap. The DFT underestimation of the gap is removed by the GW corrections.

2.2.5 The plasmon pole approximation

The screening Coulomb potential is obtained through the calculation of the inverse dielectric function. In reciprocal space, we can express it as

$$W_{\mathbf{G},\mathbf{G}'}(\mathbf{q},\omega) = \varepsilon^{-1}_{\mathbf{G},\mathbf{G}'}(\mathbf{q},\omega)V(\mathbf{q}+\mathbf{G}'), \tag{2.52}$$

where $\mathbf{G}$ and $\mathbf{G}'$ are reciprocal lattice vectors and $\mathbf{q}$ belongs to the first Brillouin zone[5]. $\varepsilon^{-1}_{\mathbf{G},\mathbf{G}'}(\mathbf{q},\omega)$ is the dielectric function and it is therefore a frequency dependent matrix; its inversion, for each frequency, is a very heavy part of the calculation. Nevertheless we can observe that the the inverse dielectric function is in general a peaked function in ω and can be approximated by

$$\epsilon^{-1}_{\mathbf{G},\mathbf{G}'}(\mathbf{q},\omega) = \delta_{\mathbf{G},\mathbf{G}'} + \frac{\Omega^2_{\mathbf{G},\mathbf{G}'}(\mathbf{q})}{\omega^2 - \tilde{\omega}^2_{\mathbf{G},\mathbf{G}'}(\mathbf{q})}, \tag{2.56}$$

where Ω and $\tilde{\omega}$ are parameters linked to the strength and the position of the peaks. They can be obtained by imposing the fulfillment of particular sum rules [53] or by calculating the inverse dielectric matrix just for two chosen frequencies along the imaginary energy axis, usually $\omega = 0$ and ω greater than the plasma frequency. This is the so called plasmon pole approximation, that has been used thorough all this thesis. For a detailed description of this approximation see [57].

2.2.6 Beyond GW

In the previous paragraphs, we have seen that, despite its apparent simplicity, the GW approach gives band gaps in quite good agreement with the experimental ones and accurate results for one-particle electronic excitations are generally obtained. However, we are dealing with a set of equations which have to be solved iteratively and hence one should calculate the vertex Γ by using G_0 and Σ_{GW} and then upgrade the polarizability and so on so forth until convergency is reached. This is out of today calculators possibility for every realistic system.
Another kind of self-consistency could be tempted that is to iterate the calculations

[5]In real space, the screened Coulomb interaction, given in term of the microscopic dielectric function $\varepsilon(\mathbf{r}_1,\mathbf{r}_2;\omega)$ and of the bare Coulomb interaction $V(\mathbf{r}_1,\mathbf{r}_2)$ is:

$$W(\mathbf{r}_1,\mathbf{r}_2;\omega) = \int d\mathbf{r}'\varepsilon^{-1}(\mathbf{r}_1,\mathbf{r}';\omega)V(\mathbf{r}',\mathbf{r}_2). \tag{2.53}$$

If we look at the Hedin's equation (2.44), we see that the microscopic dielectric function is connected to the irreducible polarizability P by:

$$\varepsilon(\mathbf{r}_1,\mathbf{r}_2;\omega) = \delta(\mathbf{r}_1-\mathbf{r}_2) - \int d\mathbf{r}'P(\mathbf{r}_1,\mathbf{r}';\omega)V(\mathbf{r}',\mathbf{r}_2). \tag{2.54}$$

We can also introduce the reducible polarizability P_{red} which is connected to the irreducible polarizability by a Dyson like equation $P_{red} = P + PVP_{red}$; the inverse of the microscopic dielectric function is now given by

$$\varepsilon^{-1}(\mathbf{r}_1,\mathbf{r}_2;\omega) = \delta(\mathbf{r}_1-\mathbf{r}_2) + \int d\mathbf{r}'V(\mathbf{r}_1,\mathbf{r}')P_{red}(\mathbf{r}',\mathbf{r}_2;\omega). \tag{2.55}$$

of the Green's function and of the self-energy, but keeping the vertex fixed, equal to identity. There are many other possibility to operate in order to obtain self-consistent results: i.e. to update just the Green's function and not the screened potential or to update also the wavefunctions; in any case this kind of calculations are much more cumbersome from the computational point of view and the results are sometimes even worse than those obtained within the non-self-consistent GW approximation. An example of self-consistent GW calculations can be found in [58] and reference therein.

The simplest way to improve the GW approximation through the inclusion of the vertex correction is the so-called GWΓ approximation [59]. This is based on the consideration that the DFT exchange and correlation potential can be view as a quite good approximation for the self-energy; the vertex Γ is hence expressed as a functional derivative of this potential with respect to the density

$$\Gamma = \frac{1}{1 - f_{xc} P_0} \qquad \text{where} \qquad f_{xc} = \frac{\delta v_{xc}^{KS}}{\delta n}. \tag{2.57}$$

This approximation corrects the quasi-particle energies but there is no significant improvement in the electronic gaps which remain close to the simple GW values.

A last comment regards the use of the GW approximation scheme to calculate neutral excitation spectra, like the absorption one, through the use of the quasi-particle energies instead of the Kohn and Sham eigenvalues. In these cases the calculated spectra generally show a blue-shift with respect to the DFT-independent particle ones (but also with respect to the experimental ones) and the lineshape are not improved at all.

2.2.7 Neutral excitation spectra

As already mentioned, the GW quasi-particles energies and states are not adequate to calculate neutral excitation spectra. The failure of this approach can be simply explained: in the GW approximation we describe excitations which involve a change in the total number of particles (addition or removal of one electron) while in order to describe neutral excitations, like excitons or plasmons, we need to consider two-particles excitations. Excitons are bounded electron-hole pairs and are mainly detected by optical absorption experiments; plasmons instead can be considered as coherent oscillations of electronic charge and can be observed by electron energy loss (EEL) experiments. In eq. (2.52) we have introduced the microscopic dielectric matrix. It can be shown[6] that the optical absorption spectra are proportional to the imaginary part of the **macroscopic** dielectric function while the EEL spectra, in the limit of vanishing momentum transfer, are proportional to the imaginary part of the inverse of the **macro-**

[6]Details about the link between microscopic properties of materials and experimental macroscopic quantities can be found in [49], [58] and references therein.

scopic dielectric function:

$$EEL \propto Im\Big\{\frac{1}{\varepsilon_M}\Big\} \qquad Abs \propto Im\Big\{\varepsilon_M\Big\}. \tag{2.58}$$

According to refs. [60],[61] the macroscopic dielectric function can be directly related to the microscopic dielectric matrix of eq. (2.52) by:

$$\varepsilon_M(\omega) = \lim_{\mathbf{q}\to 0} \frac{1}{\varepsilon^{-1}_{\mathbf{G},\mathbf{G}'}(\mathbf{q},\omega)|_{\mathbf{G}=0,\mathbf{G}'=0}}. \tag{2.59}$$

If $\varepsilon_{\mathbf{G},\mathbf{G}'}(\mathbf{q},\omega)$ is a diagonal matrix in $\mathbf{G}$ and $\mathbf{G}'$, the macroscopic dielectric function is simply

$$\varepsilon_M(\omega) = \lim_{\mathbf{q}\to 0} \varepsilon_{\mathbf{G},\mathbf{G}'}(\mathbf{q},\omega)|_{\mathbf{G}=0,\mathbf{G}'=0}. \tag{2.60}$$

This is the case of the homogeneous electron gas; on the contrary, for non-homogeneous systems, the microscopic dielectric function depends on both $\mathbf{r_1}$ and $\mathbf{r_2}$ and not only on their difference and this leads, in reciprocal space, to a dielectric matrix whose off-diagonal elements are not zero. This reflects the so-called local field effects that are as much important as the system under study is non-homogeneous on microscopic scale. To calculate the inverse of the microscopic dielectric matrix, one can use the reducible polarizability P_{red} through the equation $\varepsilon^{-1} = 1 + VP_{red}$ (as introduced in the note of section 2.2.5.). However, a different formulation of the macroscopic dielectric function can be used, which is more convenient because it allows the direct inclusion of excitonic effects [49]. By introducing a modified reducible polarizability, $\overline{P}$, we can rewrite the ε_M as:

$$\varepsilon_M(\omega) = 1 - \lim_{\mathbf{q}\to 0} V(\mathbf{q})_0 \overline{P}(\mathbf{q},\omega)|_{\mathbf{G}=0,\mathbf{G}'=0}. \tag{2.61}$$

The modified polarizability obeys a Dyson-like equation respect to the irreducible polarizability:

$$\overline{P} = P + P\overline{V}\,\overline{P}, \tag{2.62}$$

where $\overline{V}$ is a modified Coulomb interaction defined as:

$$\overline{V}(\mathbf{q})_{\mathbf{G}} = \begin{cases} 0 & \text{if } \mathbf{G}=0 \\ V(\mathbf{q})_{\mathbf{G}} & \text{else} \end{cases}. \tag{2.63}$$

The *only* difference between the bare Coulomb interaction and this modified Coulomb interaction is in the $\mathbf{G}=0$ component. It's worthwhile to notice that $\overline{V}$ is a correction term entirely responsible for the local field effects: neglecting this interaction is in fact equivalent to neglect the off-diagonal elements in the dielectric matrix and to use equation (2.60) to compute ε_M.
In conclusion, both the optical and EEL spectra are related to the macroscopic dielectric function which can be computed in terms of the reducible or the modified

polarizability. In both cases a Dyson-like equation links these quantities to the irreducible polarizability ($\overline{P} = P + P\overline{V}\,\overline{P}$ and $P_{red} = P + PVP_{red}$), which can be obtained through the Hedin's equations, at different levels of approximation. In particular, by neglecting the vertex corrections as in the GW approximation, we obtain the RPA dielectric matrix which is unable to reproduce the neutral excitation spectra.

2.2.8 Bethe-Salpeter equation

In the previous section we emphasized how, in order to describe optical and EEL spectra, we need to consider two-particles excitations. The importance of the interactions between holes and electrons in the polarization process of the system leads to the duty to include vertex corrections. In fact, if we assume $\Gamma(1,2,3) = \delta(1,2)\delta(2,3)$, we obtain the RPA irreducible polarizability, given by non-interacting particles pairs $P(1,2) = -iG_0(1,2)G_0(2,1^+)$. The inclusion of the vertex correction can be achieved through a second iteration of the Hedin's equations. By using $\Sigma = iGW$ and approximating $\delta\Sigma/\delta G = iW$, we obtain, from (2.46), an integral equation for the vertex:

$$\Gamma(123) = \delta(12)\delta(13) + iW(1^+2)\int d(67)\; G(16)\; G(72)\Gamma(673). \tag{2.64}$$

We now define a generalized three point polarizability

$$^3P(312) \equiv -i\int d(67)G(16)G(72)\Gamma(673), \tag{2.65}$$

and, by multiplying equation (2.64) on the left with $-iG(41)G(25)$ and integrating over $d(12)$, we obtain:

$$^3P(345) = -iG(43)G(35) + i\int d(12)G(41)G(25)W(1^+2)\,^3P(312). \tag{2.66}$$

Since the kernel of the integral equation (2.66) is a four-point function, it is convenient to introduce also a four-point screened interaction,

$$^4W(1234) = W(12)\delta(13)\delta(24), \tag{2.67}$$

and obtain the four-point integral equation for the irreducible polarizability ^4P:

$$^4P =^4 P_0 +^4 P^4W^4P_0. \tag{2.68}$$

We can also generalize the equation for the modified reducible polarizability in terms of four-point quantities:

$$^4\overline{P}(1234) =^4 P(1234) + \int d(5678)\,^4P(1256)\delta(56)\delta(78)\overline{V}(57)\,^4\overline{P}(7834). \tag{2.69}$$

From equations (2.68) and (2.69) the Bethe-Salpeter equation for ${}^4\overline{P}$ can be derived:

$$ {}^4\overline{P} = {}^4P_0 + {}^4P_0 K {}^4\overline{P}, \tag{2.70}$$

where the kernel K is made of two terms, the electron-hole exchange contribution coming from $\overline{V}$ and the electron-hole attraction due to $-W$,

$$ K(1234) = \delta(12)\delta(34)\overline{V}(13) - \delta(13)\delta(24)W(12). \tag{2.71}$$

A similar equation can be also obtained for a four-point reducible polarizability ${}^4P_{red}$, where V instead of $\overline{V}$ appears.

2.2.9 Two-particles Hamiltonian

In order to compute neutral excitation spectra, one should hence invert equation (2.70) for each frequency, contract the indices of the four point polarizability and finally obtain the macroscopic dielectric function. However, this procedure is a very demanding task and in general is not performed in real calculations. Instead, an effective two-particles excitonic Hamiltonian can be constructed which also carries much more information regarding the excitonic eigenstates and eigenvalues. Details of its derivation can be found in [49] and in [58]. Before writing down the Hamiltonian, we want to define the projection of a four-point quantity into the transition space (that is a basis constituted by couples of single quasi-particle states, usually labeled by a band and a wave vector indices grouped in the index n_i,); for a generic four-point operator, O(1234), its projection is given by

$$ O_{(n_1n_2)(n_3n_4)} = \int d\mathbf{r}_1 d\mathbf{r}_2 d\mathbf{r}_3 d\mathbf{r}_4 \, O(1234)\phi_{n_1}(\mathbf{r}_1)\phi^*_{n_2}(\mathbf{r}_2)\phi^*_{n_3}(\mathbf{r}_3)\phi_{n_4}(\mathbf{r}_4). \tag{2.72}$$

The two particle Hamiltonian will be given by

$$ H^{2p}_{(n_1n_2)(n_3n_4)} = (\epsilon^{QP}_{n_2} - \epsilon^{QP}_{n_1})\delta_{n_1n_3}\delta_{n_2n_4} - (f_{n_2} - f_{n_1})K_{(n_1n_2)(n_3n_4)}. \tag{2.73}$$

This Hamiltonian has two contributions: the first one contains just the energy difference between a conduction and a valence state while the second one describes the electron-hole interaction through the kernel K. With this Hamiltonian we can express the four-point modified polarizability as:

$$ \overline{P}_{(n_1n_2)(n_3n_4)} = [H^{2p} - I\omega]^{-1}_{(n_1n_2)(n_3n_4)}(f_{n_3} - f_{n_4}); \tag{2.74}$$

therefore, we still have to invert the excitonic Hamiltonian for each frequency. To overcome this bottleneck of the calculations we exploit the spectral representation of the inverse of an operator obtaining

$$ [H^{2p} - I\omega]^{-1}_{(n_1n_2)(n_3n_4)} = \sum_{\lambda\lambda'} \frac{A^{n_1n_2}_{\lambda} S^{-1}_{\lambda\lambda'} A^{*n_3n_4}_{\lambda'}}{E^{exc}_{\lambda} - \omega}, \tag{2.75}$$

where $A_\lambda^{n_1 n_2}$ and E_λ are solutions of the eigenvalue problem:

$$H^{2p}_{(n_1 n_2)(n_3 n_4)} A_\lambda^{n_3 n4} = E_\lambda A_\lambda^{n_1 n_2}, \tag{2.76}$$

and S is the overlap matrix, which differs from identity because of the non-hermitianicity of the two-particles Hamiltonian and is given by:

$$S_{\lambda\lambda'} = \sum_{n_1 n_2} A_\lambda^{*n_1 n_2} A_{\lambda'}^{n_1 n_2}. \tag{2.77}$$

The factor $(f_{n_3} - f_{n_4})$ in equation (2.74) allows to consider only the matrix elements of H^{2p} for which n_3 and n_4 have different occupation ($\{n_3 n_4\} = \{\text{valence conduction}\} = \{vc\}$ or $\{n_3 n_4\} = \{cv\}$); within this subspace the two-particles excitonic Hamiltonian will have the form:

$$H^{2p}_{(n_1 n_2)(n_3 n_4)} = \begin{pmatrix} H^{res}_{(vc)(v'c')} & \bar{K}_{(v,c)(c'v')} \\ -\bar{K}_{(c,v)(v'c')} & -H^{res}_{(cv)(c'v')} \end{pmatrix}. \tag{2.78}$$

$H^{res}_{(vc)(v'c')}$ involves only positive frequency transition and is called resonant term; it is given by:

$$H^{res}_{(vc)(v'c')} = (\epsilon_c^{QP} - \epsilon_v^{QP})\delta_{vv'}\delta_{cc'} + K_{(vc)(v'c')}. \tag{2.79}$$

The fourth term, $-H^{res}_{(cv)(c'v')}$, is called anti-resonant term and involves only negative frequency transitions while, in the off-diagonal blocks, positive and negative frequency transitions are mixed and the two $\bar{K}$ terms are called coupling terms.
If one considers only the resonant part of the excitonic Hamiltonian, the operator becomes hermitian (if the quasi-particle energies are assumed to be real) and its eigenstates will be orthogonal. In this case a simple expression for the macroscopic dielectric function can be written:

$$\varepsilon_M(\omega) = 1 - \lim_{\mathbf{q}\to 0} V(\mathbf{q}) \sum_\lambda \frac{\left| \sum_{(n_1 n_2)} \langle n_1 | \exp^{-i\mathbf{qr}} | n_2 \rangle A_\lambda^{n_1 n_2} \right|^2}{E_\lambda - \omega - i\eta}. \tag{2.80}$$

It is worth to point out two important characteristic of equation (2.80): first of all the poles of the dielectric function are at the eigenvalues of the excitonic Hamiltonian and are not given anymore by simple differences of occupied and unoccupied states; this moves the positions of the structures in the spectra with respect to the RPA case. Moreover, different independent transitions are mixed, each one contributing with a weight given by the coefficients $A_\lambda^{n_1 n_2}$, this mixing can cause a strong modification of the spectra lineshape.

2.2.10 Calculations in practice

Before concluding this section, we want to summarize all the steps which lead to the determination of neutral excitations spectra through the Bethe-Salpeter equation, and to stress all the approximations that have been used in this thesis work.

1. **DFT**
   The first step consists in a DFT ground state calculation in order to obtain Kohn-Sham eigenvalues ε_i^{KS} and eigenfunctions ϕ_i^{KS}. In these calculations, many approximations are yet introduced (see also section 2.1.5 and 2.1.6):

   - use of pseudopotentials,
   - approximated exchange and correlation potential,
   - finite sampling of the Brillouin zone,
   - introduction of an energy cutoff,
   - finite number of conduction states considered.

2. **Many body initial ingredients**
   From the Kohn-Sham energies and wavefunctions, the independent particle polarizability (P_0) is calculated together with the non-interacting Green's function (G_0) and the dielectric function, ε_{RPA}^{-1}.

   - In this step the dielectric matrix is calculated within the RPA, without local fields effects.

3. **GW approximation**
   The energy levels are then corrected within the GW approximation. Some other approximations are introduced in this step (see also section 2.2.4 and 2.2.5):

   - just one iteration of the Hedin's equations: $\Sigma = iG_0W_0$,
   - use of Kohn-Sham wavefunctions to calculate the corrections to the energies in a perturbative approach,
   - use of the plasmon-pole model to take into account the frequency dependence of the dielectric function.

4. **Bethe-Salpeter equation ingredients**
   From the Kohn-Sham wavefunctions and the GW-corrected energies, the independent quasi-particle polarizability (P_{IQP}) and the Bethe-Salpeter kernel ($K = \overline{V} - W$) are calculated.

5. **Bethe-Salpeter calculation**
   The Bethe-Salpeter calculation is finally performed:

- in this final step, just the resonant part of the excitonic Hamiltonian is often considered.

To summarize, lots of approximations are introduced in a complete calculation, but nevertheless very good results have been obtained through the Bethe-Salpeter method for a large variety of systems. On the other hand, this kind of calculations are computationally very cumbersome and this have yielded to the research of alternative and less heavy approaches, like Time Dependent Density Functional Theory which will be briefly introduced in the next section.

2.3 Time Dependent Density Functional Theory

In the first part of this chapter we described the density functional theory, which is a time-independent theory and therefore is not able to manage with excited state properties of materials. The generalization of the Hohenberg-Kohn-Sham theory to arbitrary time dependent systems was given by Runge and Gross[62], in 1984, and opened the way to Time Dependent DFT calculations. In this section we just want to describe the basic formalism of TDDFT; several reviews of this theory can be found [63]-[64] and a comparison with the many body perturbation theory is in [49].

2.3.1 TDDFT theorems

The Hohenberg and Kohn theorem in DFT establishes that, for a time independent Hamiltonian of the form $H = T + V + W$, the external potential is a unique functional of the electronic density. Now we have to consider a time dependent Hamiltonian

$$H(t) = T + W + V(t) \tag{2.81}$$

given by the kinetic term, T, the mutual electron-electron interaction, W, and a time-dependent single-particle external potential, $V(t)$; the system will be described by a time-dependent Schrödinger equation

$$H(t)\phi(t) = i\frac{\partial}{\partial t}\phi(t), \text{ with initial state } \phi(\mathrm{t_0}) = \phi_0. \tag{2.82}$$

The first theorem shown by Runge and Gross, analogue to the Hohenberg and Kohn theorem, assesses that for every single-particle potential $V(\mathbf{r}, t)$, expandable into a Taylor series around t_0, a corresponding density $n(\mathbf{r}, t)$ can be found and the map $G : V(\mathbf{r}, t) \rightarrow n(\mathbf{r}, t)$ is invertible up to an additive purely time-dependent function, $c(t)$, in the potential. At the same time, the time-dependent wavefunctions are unique functionals of the density, up to a purely time-dependent phase:

$$\phi(t) = e^{-i\alpha(t)}\phi[n, \phi_0](t), \tag{2.83}$$

which cancels out when taking the expectation value of an operator, $\widehat{O}(t)$, which does not contain derivative or integral operators on t:

$$\langle\phi(t)|\widehat{O}(t)|\phi(t)\rangle = O[n](t). \tag{2.84}$$

The second part of the Hohenberg and Kohn theorem is based on the research of the ground state exact density through the minimum principle for the total energy. A similar theorem has been established by Runge and Gross for the time dependent case but, since no minimum principle is now available, it refers to the stationary principle of the Hamiltonian action integral. The time dependent Schrödinger equation (2.82) corresponds to a stationary point of the action integral

$$A = \int_{t_0}^{t_1} dt\langle\phi(t)|i\frac{\partial}{\partial t} - H(t)|\phi(t)\rangle, \tag{2.85}$$

where A is a functional of the density, $A[n]$. The exact time-dependent density is now related to a stationary point of this action integral and can be computed from the Euler equation

$$\frac{\delta A[n]}{\delta n(\mathbf{r},t)} = 0. \tag{2.86}$$

In the last part of the Hohenberg and Kohn theorem the universal functional $F_{HK}[n]$ was introduced. In this case, if all the time dependence is contained in the potential $V(t)$, the action can be written as:

$$A[n] = B[n] - \int_{t_0}^{t_1} dt \int d\mathbf{r}\, n(\mathbf{r},t)V(\mathbf{r},t), \tag{2.87}$$

where $B[n]$ is a universal function of the density and is given by:

$$B[n] = \int_{t_0}^{t_1} dt\langle\phi(t)|i\frac{\partial}{\partial t} - T - W|\phi(t)\rangle. \tag{2.88}$$

The last analogy between the stationary and the time dependent DFT concerns the introduction of an auxiliary non-interacting particle system with the same density of the interacting one, as in the Kohn and Sham scheme. The time-dependent density can hence be computed from

$$n(\mathbf{r},t) = \sum_i \varphi_i^*(\mathbf{r},t)\varphi_i(\mathbf{r},t), \tag{2.89}$$

where the single particle orbitals $\varphi_i(\mathbf{r},t)$ obey the equation:

$$[i\frac{\partial}{\partial t} + \frac{1}{2}\nabla^2]\varphi_i(\mathbf{r},t) = V_{eff}(\mathbf{r},t)\varphi_i(\mathbf{r},t). \tag{2.90}$$

The effective potential is given by

$$V_{eff}(\mathbf{r},t) = V(\mathbf{r},t) + \int d\mathbf{r}' W(\mathbf{r},\mathbf{r}') n(\mathbf{r}',t) + V_{xc}(\mathbf{r},t), \tag{2.91}$$

where $V_{xc} = \frac{\delta A_{xc}}{\delta n(\mathbf{r},t)}$ has to be approximated in some way, as for the stationary exchange and correlation potential in DFT.

2.3.2 Exchange and correlation kernel

When dealing with time dependent linear response theory it is useful to introduce also the exchange and correlation kernel

$$f_{xc}(\mathbf{r},\mathbf{r}',t,t') = \frac{\delta V_{xc}(\mathbf{r},t)}{\delta n(\mathbf{r}',t')}. \tag{2.92}$$

Of course, both the exchange and correlation potential and kernel are unknown.

A common approximation is the adiabatic local density approximation (ALDA) which consider the f_{xc} as the functional derivative of the static LDA exchange and correlation potential (introduced in section 2.1.5):

$$f_{xc}^{ALDA}(\mathbf{r},\mathbf{r}') = \delta(\mathbf{r}-\mathbf{r}') \frac{\partial V_{xc}^{LDA}(n(\mathbf{r}),\mathbf{r})}{\partial n(\mathbf{r})}. \tag{2.93}$$

Results obtained within this approximation can be quite good or rather bad regarding optical absorption spectra of molecules and small clusters, while ALDA systematically fails for solids and in the description of Rydberg states.

This is partially due to the incorrect asymptotic behaviour of the ALDA exchange and correlation potential tail, which decays exponentially instead of the correct $1/r$ behaviour. One can therefore try to use a simpler static kernel, known as RORO kernel, with the proper asymptotic behaviour, i.e

$$f_{xc}(\mathbf{r},\mathbf{r}') = -\frac{\alpha}{|\mathbf{r}-\mathbf{r}'|}, \tag{2.94}$$

where α is a constant to be determined [65]. The constant α depends on the material considered and there is no simple recipe to calculate it. As proposed in [66, 67] for semiconductors with weak excitonic effects, the constant α can be chosen following the relation

$$\alpha = 4.615\, \varepsilon_\infty^{-1} - 0.213, \tag{2.95}$$

but this formula is not expected to work for bound excitons.

Since the main problems related to TDDFT is in the choice of the exchange and correlation kernel, in the last years, several attempts to correct these problems have been proposed and great deal of effort has been devoted to the research of more efficient approximations for the exchange and correlation potential and kernel [66, 68, 69, 70].

Chapter 3

Application to water and calculation details

This short chapter is divided into two parts. In the first one, we show how to apply the ab-initio methods described in the previous chapter to a liquid, that is a complex and disordered system. In particular we also illustrate how plane waves codes can be used also for these kind of systems. In the second part of the chapter we present the convergence tests that have been performed in order to choose the simulation parameters and the approximations which have characterized the subsequent calculations of this thesis work.

3.1 The unit cell

All the calculations presented in this thesis work are performed using codes which employ plane wave basis set. This kind of basis set allows for the intensive use of fast algorithms such as fast Fourier transforms (FFT) and moreover allows a systematic check on the convergence of the calculation. However plane waves are suited to describe periodic systems in which a certain unit cell is repeated in space, like for bulk crystals. Anyway, also lower dimensionality systems such as surfaces, nanowires, and molecules can be studied within the same scheme, even if special care has to be put in order to avoid spurious effects due to the interactions between images of the cell. A similar difficulty has to be faced when studying a liquid system such as water.

3.1.1 Molecular dynamics snapshots

The main problem regarding the study of liquids relies on the fact that, in order to simulate a complex disordered system, one should in principle use a very large unit cell, which could represent all the possible configuration; this would obviously have a prohibitive computational cost. In order to avoid this, we try a different approach, in-

spired by the ergodic hypothesis, i.e. that time average and average over the statistical ensemble are the same.

In order to study liquid water, instead of using a huge unit cell, we decided to exploit several molecular dynamics snapshots in a smaller unit cell and to average the resulting electronic and optical results over these configurations. This approach is schematically shown in figure 3.1. In particular, we use 20 configurations of 17 water molecules in a cubic unit cell with 15 a.u. side. They will be denoted by the marks $E01 \dots E20$, ordered for increasing total energy.

The water configurations have been obtained by sampling every 2 ns a 40 ns long classical molecular dynamics simulation trajectory. A TIP3P water model potential [71] has been used to represent the water molecules in our simulation box. Equations of motion have been integrated numerically using a time-step of 1 fs. The MD run has been done in the NVT ensemble, where thermal equilibrium at 298 K has been achieved applying a Nosé-Hoover thermostat [72, 73]. Electrostatic interactions were treated using the particle mesh Ewald method; all Van der Waals interactions between non-bonded atom pairs were included.
Some configurations with 32 water molecules in a cubic unit cell with 18.27 a.u. side have also been considered to test the convergence on the system size. All the molecular dynamics simulations have been performed by Dr. Michele Cascella, researcher at École Polytechnique Fédérale de Lausanne.

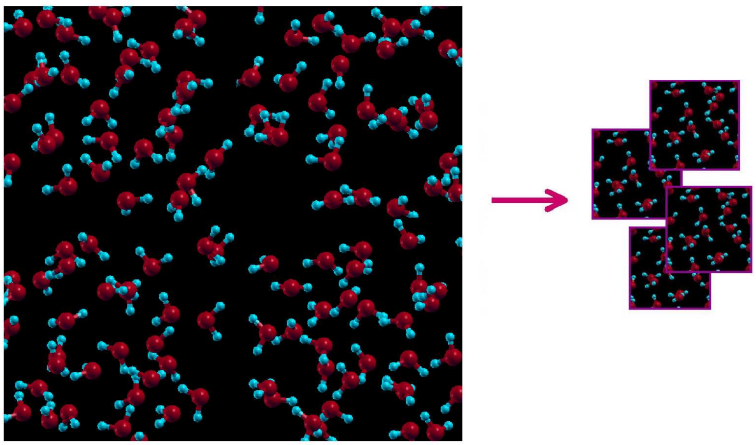

Figure 3.1: To simulate a liquid system such as water, instead of using a huge unit cell, we exploit several molecular dynamics snapshots in a smaller unit cell and average the results over these configurations.

3.1.2 Radial distribution functions

We have used 20 configurations of 17 water molecules in a cubic box with 15 a.u. side and sampled the Brillouin zone with 8 special k-points [41]. For calculations of a periodic system, in order to perform an accurate integration over the Brillouin zone, it is equivalent to increase the k-point sampling or to use larger supercells. For disordered non-periodic systems, these two approaches are no longer equivalent and more accurate results can be achieved by increasing the cell size. For the case of liquid water, 17 molecules and 8 k-points is a quite small combination; still, the computational effort of the many-body calculations for all the configurations would have been almost prohibitive and just thank to some discovered short cuts, that will be illustrated in the following, the calculations become feasible with a reasonable effort. In any case, the results obtained for 17 molecules, averaged over several snapshots, well compare with experiments as shown in the next chapter.

In particular, at the beginning of the work, we checked the adequacy of our input geometries, i.e. the 20 molecular dynamics snapshots, looking at the oxygen-oxygen and oxygen-hydrogen radial distribution functions; they are defined as the probability to find an oxygen or hydrogen atom, respectively, at a certain distance from a second oxygen atom belonging to another molecule. The resulting radial distribution functions are in very good agreement with the experimental ones [74], as it is shown in figure 3.2. This confirms that we are using good input geometries for the excited state calculations, despite of the small size of our system.

3.2 Calculation details and convergence tests

In this section we specify the characteristics of the calculations, the codes exploited, the approximations considered and a list of parameters which have been selected in the various cases, through lots of convergence tests. All the results shown in the next chapter, except if else specified, have been obtained within these approximations and using these simulation parameters.

3.2.1 DFT calculations

All DFT calculations have been performed through the use of the FHI98MD code [75], which is a plane wave basis set code.

The input geometry of the water molecules have been taken from the molecular dynamics snapshots (see previous section).

We used norm conserving pseudopotentials; first calculations have been performed in the Local Density Approximation; then we changed to the Generalized Gradient Approximation, using Perdew-Wang functionals [76, 34], that gives similar optical spectra

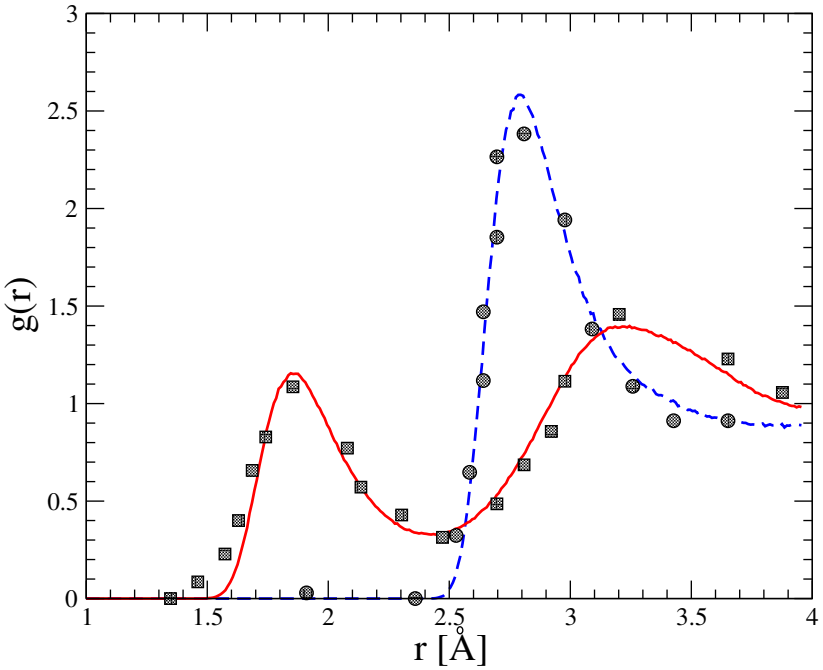

Figure 3.2: Oxygen-oxygen (blue dashed line) and oxygen-hydrogen (red continuous line) radial distribution functions, averaged over the 20 molecular dynamics snapshots, compared to experimental data [74] (circles and squares, respectively).

and slightly larger energy transitions. This can be seen in figure 3.3 where the independent particles DFT optical absorption spectra, averaged over the 20 configurations, obtained within LDA and GGA are shown together with the experimental one [77, 78]. Except if otherwise specified, all DFT results shown in the next chapter refer to GGA calculations.

It has been shown [41, 10] that the choice of the Γ point (k=(0,0,0)) as a single sampling point has a particularly slow convergence with respect to cell size. The interaction between neighboring cells leads to a k dependence of the electronic bands related to cos(**kR**). In order to minimize this effect, it is necessary to consider a finite set of k-points which zero the cosine for at least the nearest-neighbor cells. To this aim, we sampled the first Brillouin zone with 8 k-points:

$$k_1 = \left(\frac{1}{4}, \frac{1}{4}, \frac{1}{4}\right),\ k_2 = \left(-\frac{1}{4}, \frac{1}{4}, \frac{1}{4}\right),\ k_3 = \left(\frac{1}{4}, -\frac{1}{4}, \frac{1}{4}\right),\ k_4 = \left(\frac{1}{4}, \frac{1}{4}, -\frac{1}{4}\right)$$

and those obtained by inversion, in units of $2\pi/a$.

As explained in section 2.1.6, when using plane wave basis set, we have to truncate

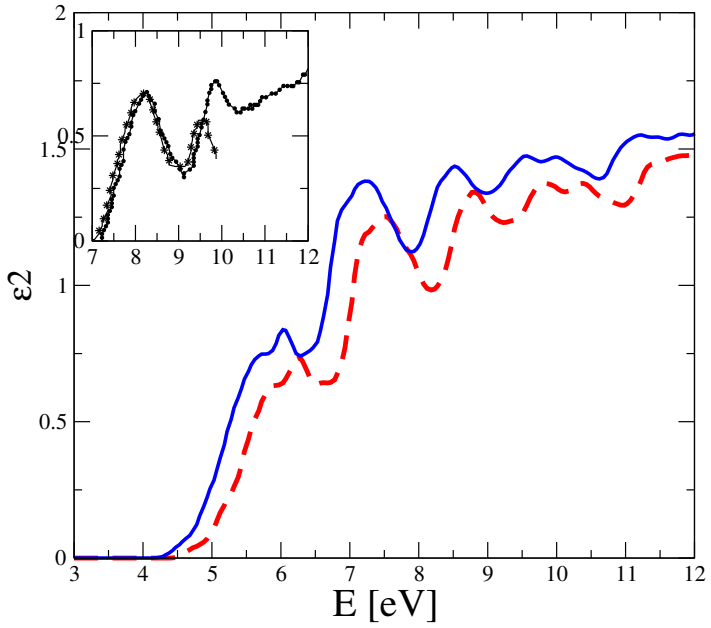

Figure 3.3: Independent particles DFT optical absorption spectra, averaged over the 20 configurations, obtained within LDA (blue continuous line) and GGA (red dashed line). The experimental spectrum is also shown in the inset [77](squares),[78](stars).

an otherwise infinite summation over the **G** vectors and to limit the wavefunctions expansion by introducing an energy cut-off. After some convergence tests both on electronic and optical properties, we decided for a kinetic energy cut-off $E_{cut} = 50Ry$ (where not else specified). Results of these convergence tests are shown in table 3.1 and in figure 3.4. In the table, the electronic gap, difference between the Highest Occupied Molecular Orbital (HOMO) and the Lowest Unoccupied Molecular Orbital (LUMO) energies, calculated for the molecular configuration E19, is reported for different values of the kinetic energy cutoff, E_{cut}. In figure 3.4 we show the independent particles DFT optical absorption spectrum, calculated for the snapshot E19, for different values of E_{cut}.

We have 17 water molecules in the unit cell, thus we have to arrange 136 valence electrons in 68 occupied "bands". We perform the calculations on all the configurations considering also 100 unoccupied bands which is a good number for the optical absorption spectra convergence, up to ~ 15 eV. Convergency tests on the number of unoccupied levels have been performed, for the molecular dynamics configuration E19, using just the Γ point to sample the Brillouin zone. Results are shown in figure 3.5.

Kinetic energy cutoff $[Ry]$	HOMO-LUMO gap $[eV]$
30	4.37
50	4.84
60	4.86

Table 3.1: Electronic gap, calculated for the snapshot E19, for different values of the kinetic energy cutoff.

For some configurations, DFT wavefunctions and eigenvalues have to be used as inputs for the calculation of the many-body screening and of the GW corrections[1]; in these cases a larger number of unoccupied levels is needed, as shown in table 3.2 in the next section, and therefore, for these configurations, we considered 600 unoccupied bands.

We have also tested the cell size convergence looking at the density of states. In ref. [10], it is emphasized that simulations of liquid water are accurate enough if one uses unit cells with 32 H_2O molecules and samples the Brillouin zone with 8 k-points or equivalently considers just the Γ point but has unit cells with 256 water molecules. We sampled the Brillouin zone with 8 k-points, but our unit cells contains "just" 17 molecules. We have hence calculated the Density of States (DoS) of our system averaging the results obtained both for the 20 molecular dynamics configurations with 17 molecules and for other 20 configurations with 32 molecules. Results are shown in figure 3.6. It can be seen the the density of occupied states is well converged already for unit cells with 17 water molecules while there are some discrepancies in the higher energy region of the DoS. However, as already mentioned, the computational effort of the many-body calculations for all the configurations with 17 molecules, has been almost prohibitive and the same calculations for 32 molecules configurations would not be feasible.

However, in order to check the sensibility of the optical properties of liquid water with respect to the cell size, it is more adequate to look at the joint density of states (JDOS). In this case, the electronic transition from valence to conduction states are considered instead of the single energy levels. Thus, the convergence of the JDOS with respect to the number of molecules in the molecular dynamics configurations can be considered as a first estimate of the optical absorption spectrum convergence. In figure 3.7 we show the JDOS calculated by averaging the DFT results over the 20 snapshots and over the k-points, both for the snapshots with 17 molecules and with 32 molecules.

[1]We will demonstrate in the following that the calculation of the screening and of the GW corrections, which are the most cumbersome parts of the work, can be restricted to just one configuration.

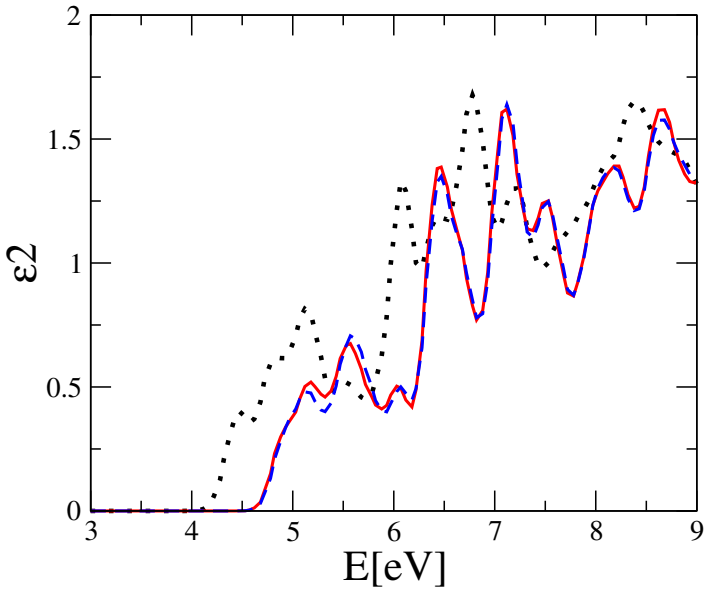

Figure 3.4: Independent particles DFT optical absorption spectrum, calculated for the molecular dynamics configuration E19, for different values of the kinetic energy cutoff: 30 Ry (black dottes line), 50 Ry (red continuous line) and 60 Ry (blue dashed line).

We note that no pronounced differences are present; this gives a first indication that unit cells with 17 water molecules, together with sampling of the Brillouin zone with 8 k-points and average over several configurations are already sufficiently large for this purpose.

3.2.2 GW calculations

The second step in our work consists in the calculation of the GW corrections to the Kohn and Sham eigenvalues. This part has been faced within a first order perturbative approach, as explained in section 2.2.4, exploiting the "Nanoquanta"-GW code.

First of all, the screened Coulomb interaction has been calculated. Starting from a DFT calculation performed on a cubic unit cell with 15 a.u. side and with a kinetic energy cut-off of 50 Ry, we have to manage with 20163 G vectors; we calculated the screening, ε^{-1}, using just a fraction of all these plane waves: 13997. The screened potential W has been obtained within the plasmon pole model and 600 empty states have been considered. In table 3.2 we show the results of the GW convergence tests for the number of unoccupied levels, i.e. the GW corrections obtained, to the HOMO

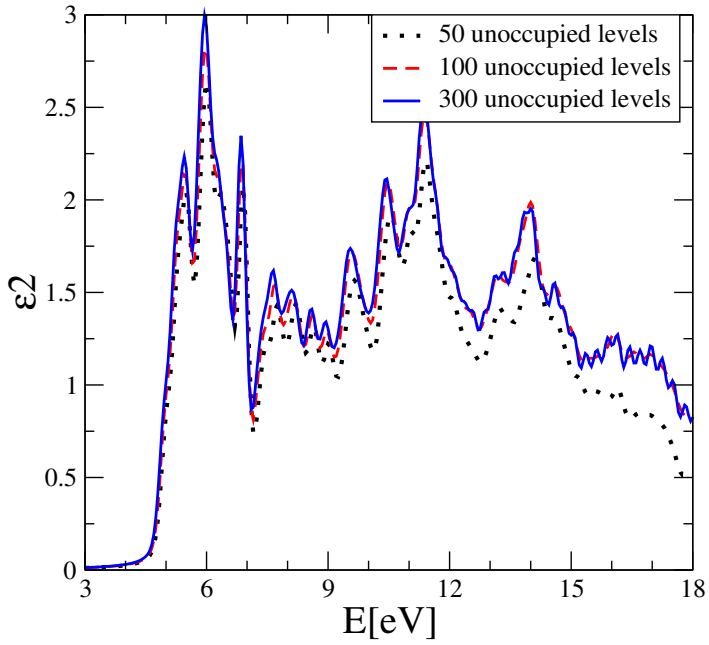

Figure 3.5: Independent particles DFT optical absorption spectrum, calculated for the snapshot E19, for different numbers of unoccupied levels: 50 levels (black dotted line), 100 levels (red dashed line) and 300 levels (blue continuous line). These calculations have been realized using just one k-point, Γ.

and LUMO energy levels, for different numbers of empty states. These convergence tests have been performed for the snapshot E19, with a kinetic energy cutoff of 30 Ry and using just 1021 G vectors.

Then we use the screened interaction in order to obtain the GW correction to the Kohn and Sham energies. We calculate the correlation part of the self-energy using 13997 plane waves while, for the exchange term of the self-energy, we exploit 19933 plane waves. Exact GW corrections have been calculated for the last 10 occupied states and for the first 10 unoccupied states. Anyway, we corrected all the filled bands and 100 of the empty ones by interpolating the GW corrections. As shown in table 3.3, where the GW corrections to the HOMO and LUMO energy levels and to the gap calculated for three different molecular dynamics snapshots are reported, these corrections result to be independent on the configuration and it has been possible to calculate the self-energy just for one configuration, reducing considerably the computational work.

GW corrections [eV]			
Empty states	ΔHOMO	ΔLUMO	Δgap
300	-0.3	2.4	2.7
500	-0.2	2.2	2.4
600	-0.2	2.2	2.4

Table 3.2: GW corrections to the HOMO and LUMO energy levels and to the electronic gap, for different numbers of empty states. These tests have been performed for the snapshot E19, with a reduced kinetic energy cutoff of 30 Ry and using just 1021 G vectors.

GW corrections [eV]			
Configuration	ΔHOMO	ΔLUMO	Δgap
E19	-2.02	1.83	3.85
E01	-2.03	1.82	3.85
E14	-2.04	1.82	3.86

Table 3.3: GW corrections to the HOMO and LUMO energy levels and to the electronic gap, for three different molecular dynamics snapshots (E19, E01, E14). These values have been calculated with a kinetic energy cutoff of 50 Ry, 600 conduction levels, 13997 plane waves for the correlation self-energy and 19933 plane waves for the exchange part of the self-energy.

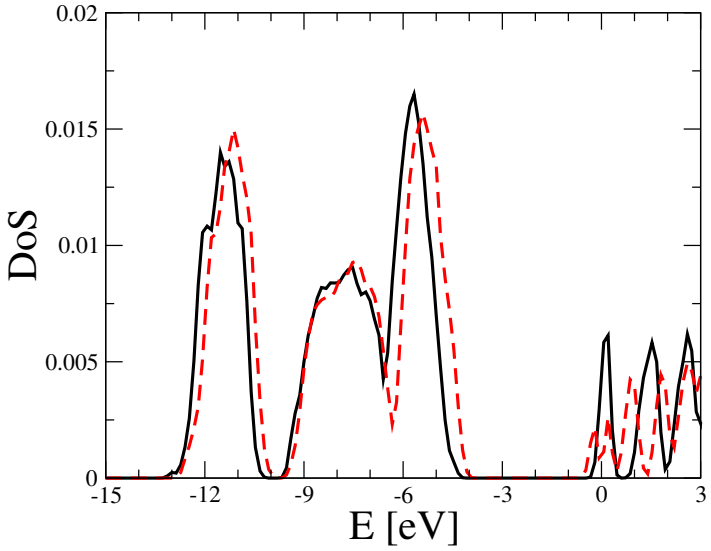

Figure 3.6: Density of States, averaged over 20 molecular dynamics configurations with 17 (black continuous lines) and 32 (red dashed lines) water molecules.

3.2.3 Optical absorption spectra calculations

The third step of the work has been the calculation of the optical absorption spectra through the solution of the Bethe-Salpeter equation; in this part of the work we exploit the EXC code[2]. In the previous section, we have said that the GW corrections are independent on the molecular dynamics configuration. In figure 3.8 we show the optical absorption spectra obtained for the snapshot E19, exploiting its own screening function and the screening functions calculated for the configurations E01 and E14. From the figure we cannot appreciate any difference between these three spectra. For this reason, the calculation of the optical absorption spectra of liquid water has been performed on all the 20 molecular dynamics snapshots by always exploiting the same screening and GW corrections.

We consider all the 68 occupied states and 100 unoccupied levels (in figure 3.5 we have just shown that convergence, up to 15 eV, is reached with this number of empty states). The resulting excitonic Hamiltonian is a matrix with size 54400x54400; this is a too large matrix to be diagonalized directly and to treat it we exploit the Haydock algorithm [79].

We tried also some calculations of the optical properties in the Time Dependent-DFT framework. In these simulations we try two different exchange and correlation

[2]EXC code - http://theory.polytechnique.fr/codes/exc and http://www.bethe-salpeter.org/

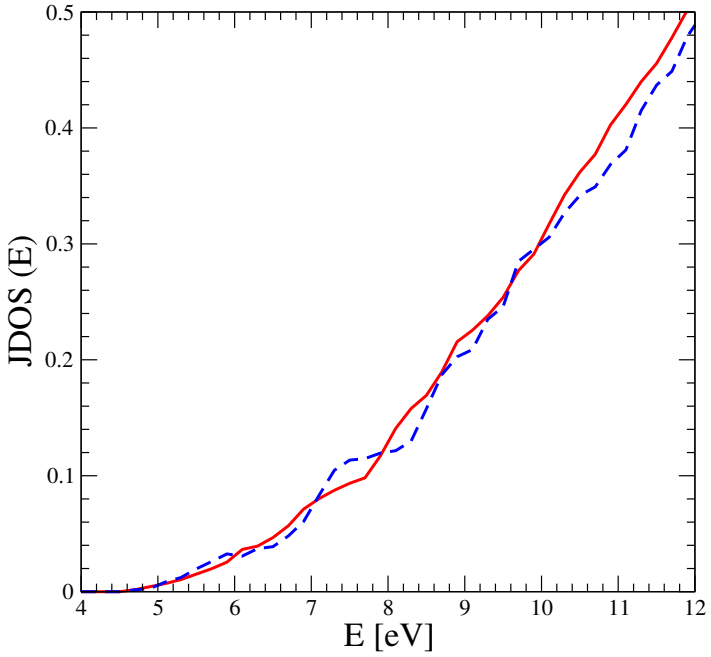

Figure 3.7: Joint density of States, averaged over 20 molecular dynamics configurations with 17 (blue dashed line) and 32 (red continuous line) water molecules.

kernels: the ALDA one and the RORO kernel, both described in section 2.3.2. We consider the same number of empty bands as in the case of the Bethe-Salpeter equation, i.e. 68 occupied bands and 100 unoccupied ones. To perform these calculations we exploit the code "dp"[3].

All the results will be shown in the following chapter.

[3]http://theory.polytechnique.fr/codes/dp/

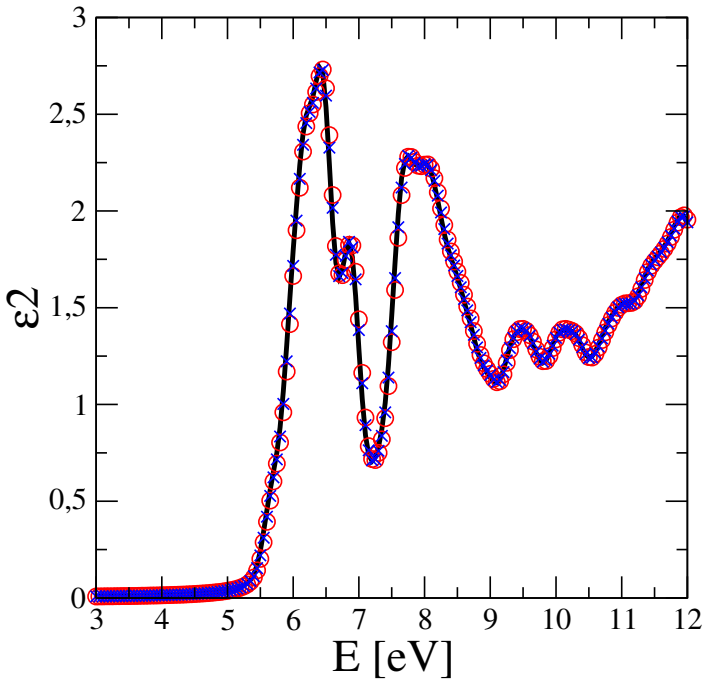

Figure 3.8: Optical absorption spectra of liquid water obtained for the snapshot E19, exploiting its own screening function (black line) and the screening functions calculated for the configurations E01 (red circles) and E14 (blue crosses).

Chapter 4

Excited state properties of liquid water

In this chapter we illustrate and discuss the results obtained in the study of the excited state properties of liquid water. We first show some results regarding electronic properties and electron energy loss spectrum of water. Then we describe the results obtained in the calculation of the optical absorption spectrum, both through the solution of the Bethe-Salpeter equation and with other techniques and approximations. We also present a comparison with recent results obtained for hexagonal ice by Hahn et al.[80]. The last part of the chapter is devoted to the illustration of the main methodological findings related to the study of the excited state properties of a liquid, hence disordered, system.

4.1 Electronic properties: results and discussion

We performed the electronic and spectroscopic calculations on various theoretical levels. We started with density functional theory (DFT) to obtain the Kohn-Sham (KS) eigenvalues and eigenvectors and the independent-particle (DFT-RPA) absorption spectrum. As expected, DFT energy levels are not in agreement with the experimental ones; therefore we corrected the Kohn-Sham energy levels using the Green's function perturbation approach, with the exchange-correlation self-energy calculated within the GW approximation: $\Sigma = iGW$. The quasi-particle (QP) energies (that is, the electronic 'band structure' of water), were calculated in first order perturbation theory, as explained in chapter 3.

Electronic gap [eV]					
Configuration	k_1	k_2	k_3	k_4	**Average**
E01	5.42	5.41	5.41	5.43	5.42
E10	5.27	5.28	5.27	5.29	5.28
E20	5.33	5.32	5.33	5.34	5.33

Table 4.1: DFT-GGA electronic gaps obtained for three configurations (as an example) for the k-points $k_1 = \left(\frac{1}{4}, \frac{1}{4}, \frac{1}{4}\right)$, $k_2 = \left(-\frac{1}{4}, \frac{1}{4}, \frac{1}{4}\right)$, $k_3 = \left(\frac{1}{4}, -\frac{1}{4}, \frac{1}{4}\right)$ and $k_4 = \left(\frac{1}{4}, \frac{1}{4}, -\frac{1}{4}\right)$, together with the average over these four k-points.

4.1.1 Electronic gap

DFT and GW results for the electronic 'band structure' of water are presented in this section. In table 4.1 we report the DFT electronic gaps obtained for three configurations (as an example) for the k-points

$$k_1 = \left(\frac{1}{4}, \frac{1}{4}, \frac{1}{4}\right),\ k_2 = \left(-\frac{1}{4}, \frac{1}{4}, \frac{1}{4}\right),\ k_3 = \left(\frac{1}{4}, -\frac{1}{4}, \frac{1}{4}\right),\ k_4 = \left(\frac{1}{4}, \frac{1}{4}, -\frac{1}{4}\right),$$

together with the average over all the k-points.

In table 4.2 we instead report the energy levels relative to the Highest Occupied Molecular Orbital (HOMO) and Lowest Unoccupied Molecular Orbital (LUMO) and the corresponding gaps, averaged over the 8 k-points, for each of the 20 molecular dynamics snapshots. These energy levels have been calculated, and hence are reported, both within DFT-LDA and DFT-GGA. A slightly better agreement in the peaks positions of the optical absorption spectrum is however obtained in GGA and, where not else specified, further results have to be regarded as relative to GGA calculations. DFT HOMO and LUMO energy levels for each of the 20 configurations are also shown in figure 4.1.

From both table 4.2 and figure 4.1, we can observe that the LUMO level is more stable with respect to changing of configuration and that the gap is larger within GGA.

Averaging over both the 8 k points and the 20 configurations, the DFT HOMO-LUMO gap turns out to be 5.09 eV in GGA, and 4.85 eV within LDA, in good agreement with previous DFT calculations [1] but strongly underestimating the experimental gap (8.7 ± 0.5 eV [81]), as expected in DFT. Values of the experimental gap are obtained from direct photoemission measurements for the determination of the HOMO level, and from work function measurements of charged water for the determination of the LUMO level [81, 1].

In order to correct the KS energy levels, one has in principle to calculate the GW corrections $\Delta\varepsilon_n^{QP}$ for *all* the 20 molecular dynamics configurations, followed by an average. Instead, as it has been illustrated and discussed in details in the previous chapter,

Electronic energies and gap, in eV, averaged over the k-points						
Configuration	HOMO LDA	HOMO GGA	LUMO LDA	LUMO GGA	Gap LDA	Gap GGA
E01	-5.08	-4.86	0.06	0.56	5.14	5.42
E02	-4.97	-4.75	0.06	0.53	5.03	5.28
E03	-4.82	-4.59	0.04	0.52	4.84	5.11
E04	-5.07	-4.85	0.11	0.56	5.18	5.41
E05	-4.87	-4.25	0.09	0.46	4.96	4.71
E06	-4.92	-4.70	0.08	0.56	5.00	5.26
E07	-4.87	-4.64	0.04	0.54	4.91	5.18
E08	-4.51	-4.27	-0.04	0.44	4.47	4.71
E09	-4.80	-4.58	0.09	0.55	4.89	5.13
E10	-4.97	-4.77	0.01	0.51	5.07	5.28
E11	-5.15	-4.92	0.00	0.50	5.15	5.42
E12	-4.44	-4.24	0.00	0.46	4.44	4.70
E13	-4.84	-4.64	0.04	0.51	4.88	5.15
E14	-4.56	-4.34	0.06	0.54	4.62	4.88
E15	-4.76	-4.55	-0.03	0.45	4.73	5.00
E16	-4.65	-4.43	-0.08	0.42	4.57	4.85
E17	-4.74	-4.52	-0.10	0.37	4.64	4.89
E18	-4.71	-4.51	-0.06	0.44	4.65	4.95
E19	-4.83	-4.63	0.02	0.47	4.85	5.10
E20	-5.05	-4.83	0.01	0.50	5.06	5.33

Table 4.2: DFT HOMO and LUMO energies and the corresponding electronic gaps, averaged over the k-points, obtained for each of the 20 configurations, both within LDA and GGA. The zero of the energy is arbitrarily chosen at the LUMO of E11 configuration.

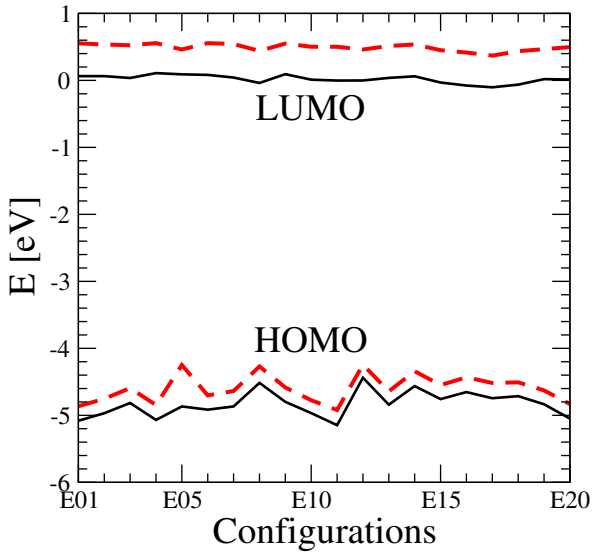

Figure 4.1: DFT HOMO and LUMO energies, both within LDA (black continuous line) and GGA (red dashed line), averaged over the 8 k-points, for each of the 20 molecular dynamics configurations.

GW corrections	
Energy level	GW correction [eV]
HOMO-1	-1.7
HOMO	-1.7
LUMO	+1.6
LUMO+1	+1.8

Table 4.3: GW corrections averaged over the k-points, calculated for the snapshot E19.

we found that the differences between DFT and GW energies are almost constant going from one snapshot to another. We could hence use the same corrections, $\Delta\varepsilon_n^{QP}$, for all the configurations. GW corrections to the last two occupied levels (HOMO-1 and HOMO) and to the first two unoccupied ones (LUMO and LUMO+1), averaged over the k-points, are reported in table 4.3. These corrections have been calculated for the snapshot E19 and applied to all the molecular dynamics configurations.

Starting from the GGA value of 5.09 eV, the GW corrections increase the electronic HOMO-LUMO gap up to 8.4 eV, well within the experimental range, (8.7 ± 0.5) eV [81]. The opening of the gap is also schematically illustrated in figure 4.2.

4.1.2 EELS

As explained in section 2.1.7, from the Kohn and Sham eigenvalues it is possible to obtain the DFT-independent particle absorption and electron energy loss spectra. While the optical absorption spectrum is generally not in agreement with the experimental one, the EELS spectrum is often well described within this approximation [46].

We have calculated the EELS spectra of liquid water at DFT-independent particle level for each of the 20 configurations, for a wavevector transfer $q = 0$. These calculations have been performed in the local density approximation, with an energy cut-off of 30 Ry. The averaged spectrum is shown in figure 4.3. The experimental spectra for finite wavevector transfers $q = 0.69$ a.u. and $q = 0.19$ a.u. are also shown for comparison [82]. We can note that a good agreement is reached for what concerns the peak position and lineshape even if, looking at the onset and in general at the low energy region of the spectrum, where excitonic effects are more important, the agreement is less satisfactory.

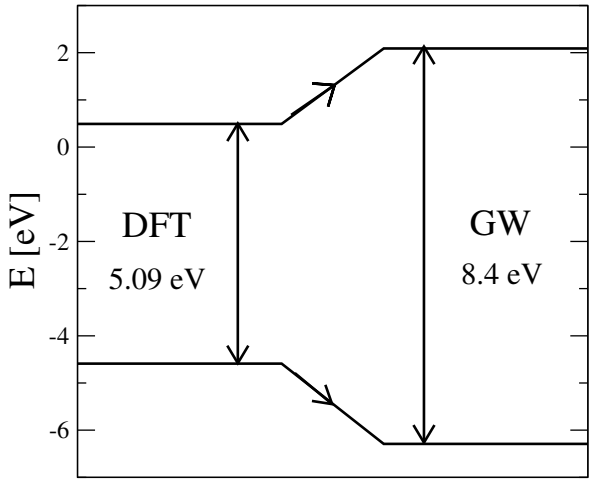

Figure 4.2: Schematic view of the HOMO-LUMO gap, calculated within DFT-GGA and GW, averaged over both the 8 k-points and the 20 configurations.

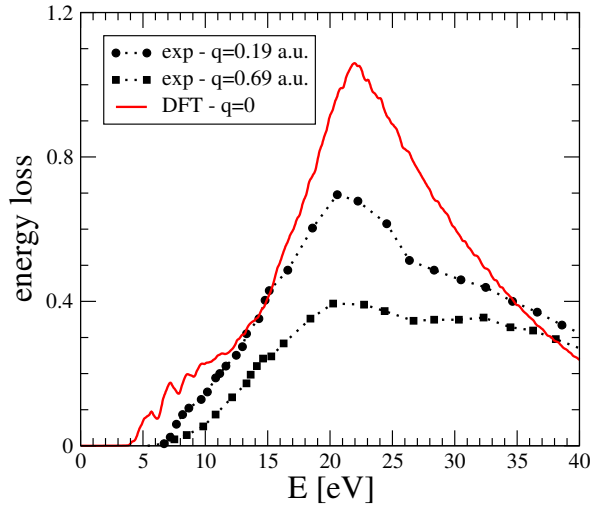

Figure 4.3: DFT-independent particle energy loss spectrum for liquid water, averaged over 20 configurations, for a wavevector transfer $q = 0$ (red line). The experimental spectra for finite wavevector transfers $q = 0.69$ a.u. and $q = 0.19$ a.u. are also shown (black circles and squares) [82].

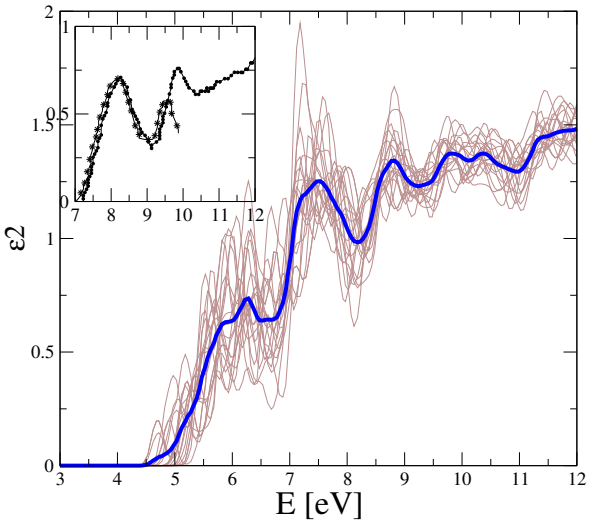

Figure 4.4: DFT-independent particle optical absorption spectra of liquid water, for each of the 20 configurations (brown lines) and their average (blue bold line). The experimental spectrum is also shown in the inset [77](squares),[78](stars).

4.2 Optical absorption spectrum: results and discussion

The optical absorption spectrum of liquid water has been calculated at different levels of approximation. We have first evaluated the DFT-independent particle absorption spectrum but, as expected, the results are not in agreement with experiments. Therefore we looked at the GW-independent particle spectrum with even worst results. Solving the Bethe-Salpeter equation we obtained at last a good optical spectrum. We also tried to reach similar good results with less expensive calculation methods, such as Time Dependent-DFT, without success.

4.2.1 Optical absorption spectrum - BSE calculation

First we performed the calculation of the optical absorption spectrum of liquid water at the DFT independent particles level. Results obtained for the 20 molecular dynamics snapshots, together with their average are shown in figure 4.4; the experimental absorption spectrum, obtained from reflectance measurements, is also reported in the inset [77, 78]. From the figure we can observe that the 20 absorption spectra and, more important, their average do not compare in a satisfactory way with the experi-

mental one: the onset of the absorption is strongly underestimated in our calculation, the peak positions are red-shifted in comparison with the experiment, and the relative intensities of the first two absorption peaks are not well reproduced.

Since the calculated GW shifts to the occupied and unoccupied energy levels are almost constant (see table 4.3), GW-independent particle optical spectra and their average show lineshapes very similar to DFT ones, but shifted to higher energies. This can be seen in figure 4.6, where both DFT (black dashed line) and GW (blue dotted line) averaged spectra are shown. The agreement with the experimental optical absorption spectrum is hence not at all improved, since the relative intensities of the two structures (seen in experiments at 8.3 eV and 9.6 eV) are still not reproduced, and their positions, from being red shifted in DFT calculations, are now strongly blue shifted.

We have hence clear hints that it is necessary to include the electron-hole interaction to describe the optical properties of water. To this end we solved the Bethe-Salpeter equation (derived in section 2.2.8), where electrons and holes interact through the screened Coulomb potential W. These cumbersome calculations have been done for all the 20 molecular dynamics configurations, but using always the same screening function (see sections 3.2.3 and 4.3). Results are shown in figure 4.5 for all the snapshots together with their average. The averaged spectrum is also reported in figure 4.6 (red continuous line), together with the DFT (black dashed line) and GW (blue dotted line) ones.

From these figures, it can be noted that dramatic many-body effects are present. The agreement with the experiment, both in energy peak positions and onset as well as in the relative intensities of the first two peaks, is significantly improved. The main remaining discrepancy is an overall red shift, that might be due to a residual error arising from the limited size of our cell, and to the fact that our GW calculations are not self-consistent but use DFT wavefunctions and energies.

The first peak in the spectrum turns out to be a bound exciton with a binding energy of 2.4 eV and large oscillator strength. These are a consequence of the weak electronic dielectric screening of water ($\epsilon_\infty \sim 1.8$). The second peak results from an excitonic enhancement of the oscillator strength of interband transitions with respect to the single quasi-particle case.

4.2.2 Optical absorption spectrum - other calculations

We also tried to obtain the optical absorption spectrum of liquid water with less expensive calculation methods.

Test calculations have been done, for one molecular dynamics snapshot (E01), using a *constant* value for ε^{-1}, in the screened potential W. The resulting spectrum for a value of $\varepsilon^{-1} = 1/1.7$ (near to the experimental macroscopic electronic value 1/1.8) is shown in figure 4.7 (blue continuous line), together with the absorption spectrum

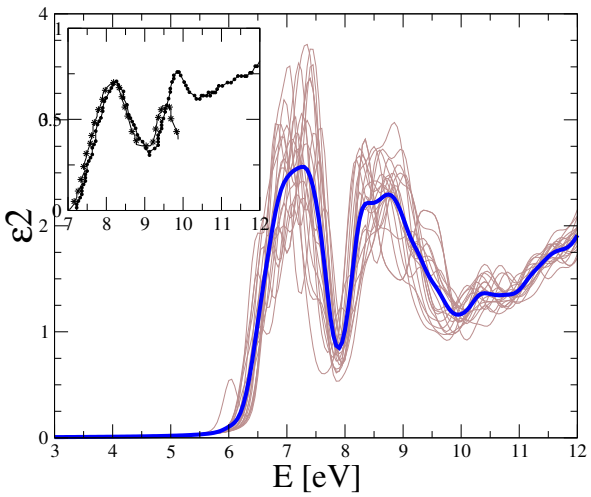

Figure 4.5: Optical absorption spectra of liquid water, for each of the 20 configurations (brown lines) and their average (blue bold line), obtained by solving the Bethe-Salpeter equation. The experimental spectrum is also shown in the inset [77](squares),[78](stars).

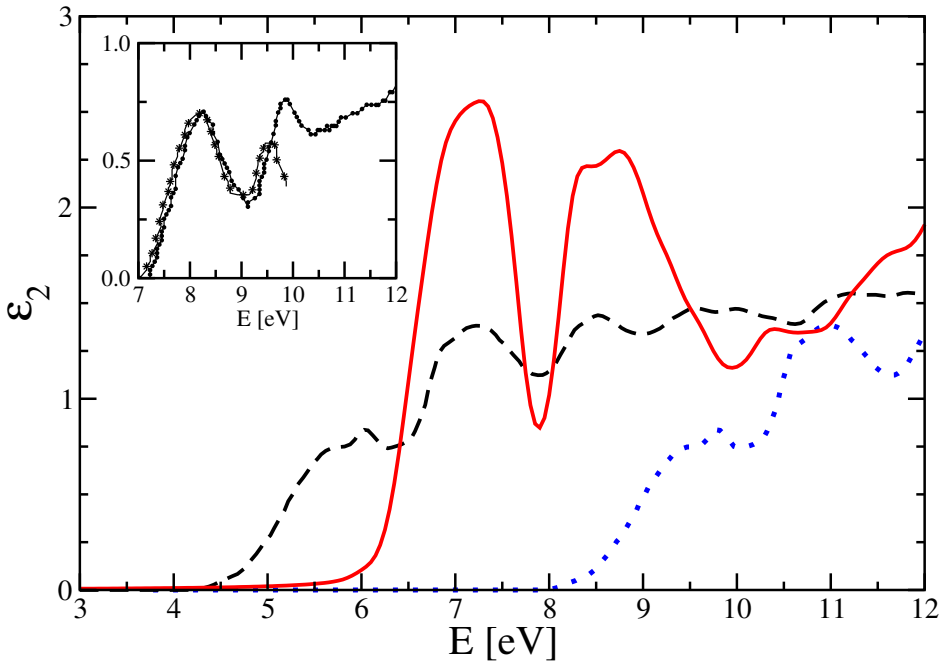

Figure 4.6: Optical absorption spectra of liquid water, averaged over the 20 configurations, calculated at DFT-independent particle level (black dashed line), GW-independent particle level (blue dotted line) and by solving the Bethe-Salpeter equation (red continous line). The experimental spectrum is also shown in the inset [77](squares),[78](stars).

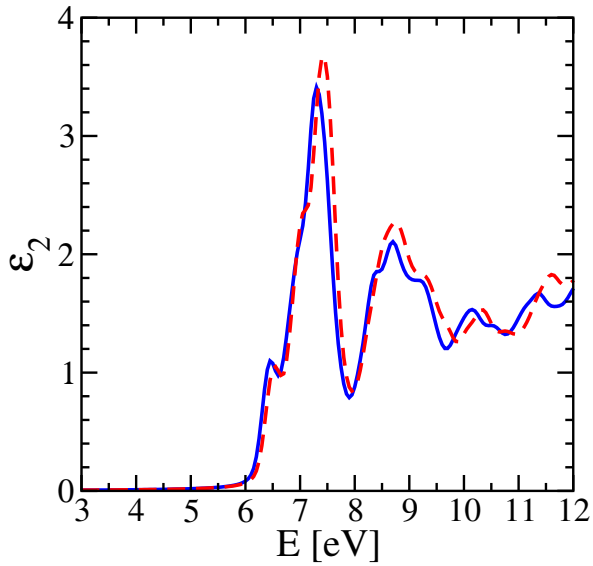

Figure 4.7: Optical absorption spectra of liquid water, calculated for the molecular dynamics configuration E01, using the full screened electron-hole interaction (red dashed line) and using for W a constant dielectric function $\varepsilon^{-1} = 1/1.7$ (blue continous line).

obtained, for the same configuration, with the full screened electron-hole interaction (red dashed line). We can observe that a good agreement is achieved and this can be interpreted as a further indication that the optical absorption spectrum is not particularly sensible to the details of the screening function.

The optical absorption spectrum of liquid water has been also calculated within Time Dependent-DFT. In principle this method represents an exact way to calculate optical spectra, but the quality of the results depends on the approximation used to describe exchange-correlation effects, i.e. on the choice of the exchange-correlation kernel. A widely used and computationally efficient approximation is the Adiabatic Local Density Approximation (ALDA), described in section 2.3.2. The optical spectrum obtained, for one molecular dynamics configuration (E01), with the ALDA kernel is shown in figure 4.8 together with the DFT-RPA spectrum for the same configuration; unfortunately the TD-LDA result shows no improvement with respect to the DFT independent-particles result. Long-range and/or dynamical effects that are missing in the ALDA kernel should hence be important for the absorption spectrum of water, and one has to resort to more elaborate (hence time-consuming) TDDFT approximations [66, 68, 69, 70].

Since one of the main problems related to the ALDA kernel is the incorrect asymp-

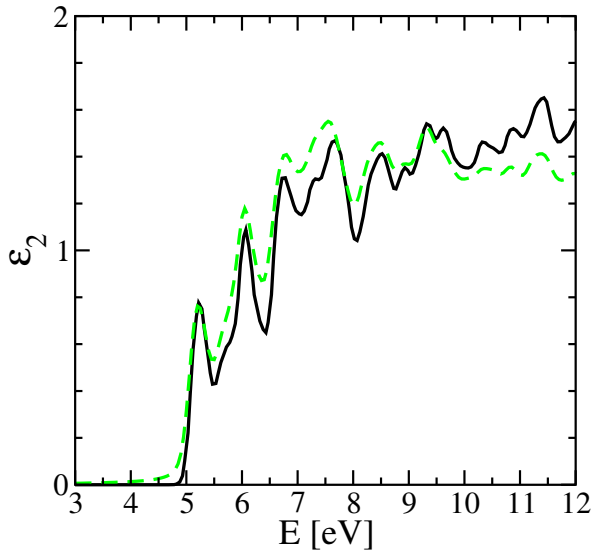

Figure 4.8: Optical absorption spectrum, for the molecular dynamics configuration E01, obtained within Time Dependent-DFT, with the ALDA kernel (green dashed line), and within the DFT-independent particle framework (black continous line).

totic behaviour of the exchange and correlation potential tail, which decays exponentially instead of the correct $1/r$, one can try to use a simpler static kernel, with the proper asymptotic behaviour, i.e

$$f_{xc}(\mathbf{r}, \mathbf{r}') = -\frac{\alpha}{|\mathbf{r} - \mathbf{r}'|}, \tag{4.1}$$

where α is a constant [65] to be determined; this is the so called "RORO" kernel. The constant α depends on the material considered and there is no simple recipe to calculate it. As proposed in [66, 67] for semiconductors with weak excitonic effects, the constant α can be chosen following the relation

$$\alpha = 4.615\, \varepsilon_{\infty}^{-1} - 0.213, \tag{4.2}$$

but this formula is not expected to work for bound excitons.

We tried to calculate the optical absorption spectrum of one molecular dynamics snapshot (E19) using this static kernel, for different values of α: from $\alpha = 2.3$, obtained from equation (4.2), to $\alpha = 12$. Results are shown in figure 4.9 together with the spectrum obtained by solving the Bethe-Salpeter equation; it can be seen that no agreement is achieved, whatever α is chosen: either the peak position is strongly blue shifted (for smaller values of α), or the peak intensity is enormously overestimated (for larger values of α).

4.2.3 Comparison with ice

In a recent paper [80], a similar work (excited state properties, from DFT to BSE) for hexagonal ice has been reported; we now discuss a comparison of the results.

Looking at the electronic gap, we found that the GW corrections increase the HOMO-LUMO gap to 8.4 eV; a larger gap, ~ 9.5 eV, is instead obtained for hexagonal ice. The gap reduction in the liquid phase is probably due to the disordered structure of liquid water with respect to the reference ordered system, i.e. ice; similar results are in fact found for semiconductor alloys where it has been shown that disorder can cause a decrease of the band gap [83].

The optical absorption spectra of hexagonal ice, obtained in the frameworks of the independent particle DFT and GW and by solving the Bethe-Salpeter equation, are shown in figure 4.10. From the comparison of the spectra of liquid water and hexagonal ice we can observe that the binding energy of the lower water exciton, although quite large (2.4 eV), is smaller than the value E_b= 3.2 eV found for ice. In fact, one can expect that the mixing of electron-hole pairs of different energy, which leads to the bound exciton, partially counterbalances the disorder effect on the quasi-particle gap [83]; hence excitons are less bound in disordered systems since they do not follow completely the decrease of the band gap. Moreover, the higher density in the liquid phase with respect to ice (around 7%), may also play a role in reducing the exciton binding energy, by allowing a greater mobility of electrons and holes.

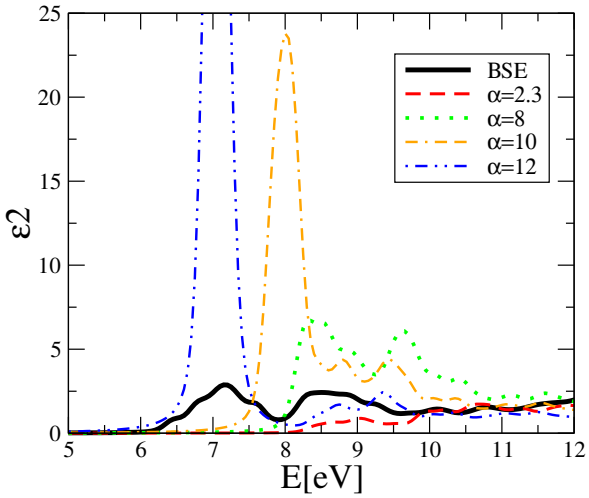

Figure 4.9: Optical absorption spectrum, for the molecular dynamics configuration E19, obtained with the kernel $f_{xc}(\mathbf{r},\mathbf{r}') = -\frac{\alpha}{|\mathbf{r}-\mathbf{r}'|}$, for different values of α (colored lines), and by solving the Bethe-Salpeter equation (black bold line).

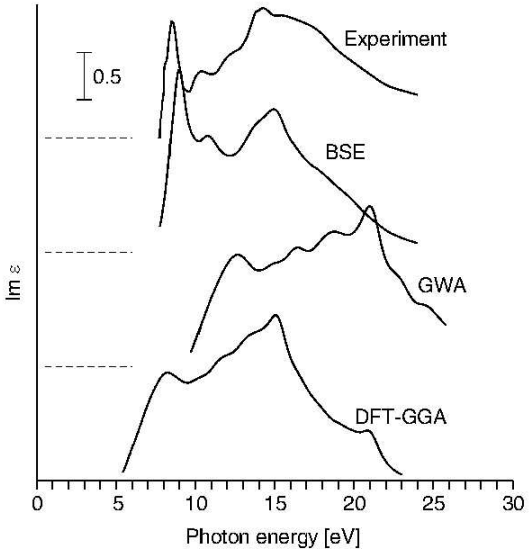

Figure 4.10: Optical absorption spectra of hexagonal ice, obtained within the frameworks of the independent particles DFT and GW and by solving the Bethe-Salpeter equation, from [80]. The experimental spectrum is also reported [84].

4.3 Methodological results

Due to the heaviness of this kind of calculations, it has been of fundamental importance to explore to which extent a detailed calculation of each single configuration was mandatory. We summarize here the main methodological results:

1. the effect of the electron-hole interaction does not depend significantly on details of the screened Coulomb interaction W, but rather on macroscopic averages [49] and therefore we could expect, as effectively found out, that the optical spectra of the various molecular dynamics snapshots can be calculated using the same screening obtained for any one of them. This has been explicitly proven in the previous chapter, in figure 3.8.

2. Gw corrections turn out to be independent on the molecular dynamics snapshot, as shown in the previous chapter, in table 3.3.

3. Another important test regards the number of configurations needed to obtain good averaged results. In figure 4.11 we report the optical absorption spectrum of liquid water obtained by averaging over different numbers of molecular dynamics snapshots, randomly chosen. We can note that a "good" absorption spectrum is found (in agreement with the average over all the configurations) already for a 5-snapshots average.

These two methodological findings can be very important for future calculations on similar disordered systems, since they allow to significantly reduce the computational cost of a work which otherwise will be almost prohibitive.

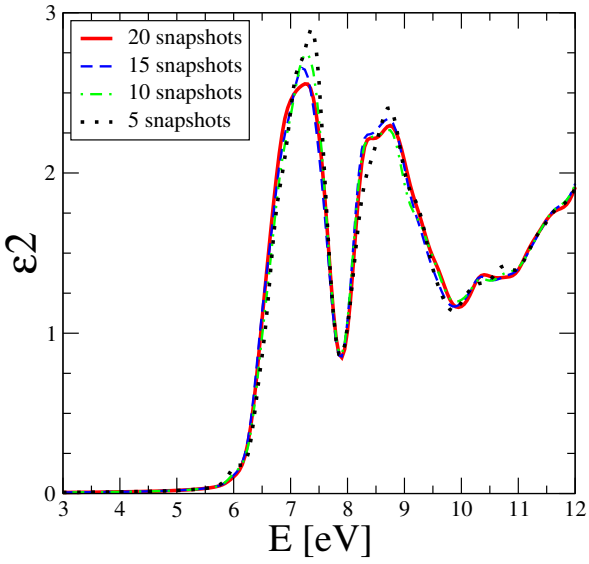

Figure 4.11: Optical absorption spectra of liquid water obtained by averaging over different numbers of molecular dynamics snapshots, randomly chosen.

Chapter 5

Deep Inelastic Neutron Scattering

In this chapter we will illustrate the basic theory and the experimental technique for Deep Inelastic Neutron Scattering. In the first part of the chapter we will introduce neutrons as a probe for spectroscopic studies of materials showing their properties, advantages and drawbacks. Then we will show the main ideas, assumptions and approximations involved in deep inelastic neutron scattering theory, with special regards to the Impulse Approximation. In the last part of the chapter, we will describe the whole neutron experiment instrumentation, from the neutron sources to the spectrometers and detectors.

5.1 The neutron probe

In 1994 the Nobel prize in physics was awarded to Brockhouse and Shull for their contributions to the development of neutron scattering techniques, both diffraction and spectroscopy, designing the path to answer the questions:

where atoms are and *what atoms do.*

Neutrons are electrically neutral subatomic particles that, together with protons, form nearly the entire mass of the atomic nuclei. Some of their properties are listed in table 5.1.

Mass	1.675 x 10^{-27} Kg
Charge	0
Spin	$\frac{1}{2}$
Magnetic moment	-9.66 x 10^{-27} JT^{-1}

Table 5.1: Main properties of neutrons

Neutrons are a powerful probe and present significant advantages over many other radiative probes. One of the reasons is that neutrons are uncharged particles and

therefore they interact with the nuclei of the atoms rather than their electronic clouds. Consequently the neutron scattering cross section of an atom is not at all related to its atomic number and this gives some interesting advantages over other spectroscopic techniques as X-rays and electron scattering. First of all, with neutron scattering experiments, it is possible to probe also light atoms, as hydrogen, in the presence of heavier ones too. Moreover, the neutron scattering cross sections can be substantially different for neighboring elements in the periodic table and also for isotopes of the same element. One drawback is that neutrons do not interact much with matter but, on the same time, this makes neutrons a highly penetrating and non-destructive probe, thus allowing the study of the bulk of materials and also of delicate biological systems.
Neutrons are fermions and their magnetic moment can couple with the magnetization of materials; moreover the magnetic scattering and the nuclear scattering cross sections are of the same order of magnitude. Because of these reasons, neutrons are an ideal probe also for the study of microscopic magnetism and general magnetic phenomena.

Standard nomenclature classifies neutrons in different categories depending on their energy, as shown in table 5.2. Neutron pulses from a spallation source, after passing a cold and/or hot moderator, have typical energies in the range from meV up to hundreds of eV; this is exactly the same scale of energies of the principal atomic and electronic processes, i.e. quantum tunneling, molecular translations, rotations and vibrations and also electronic transitions, thus allowing neutrons to answer the question

"What atoms do".

Moreover neutron wavelengths, in the range (0.05 - 20) Å, are similar to atomic spacings, allowing diffraction experiments both on periodic crystal structures and on macromolecules, hence answering the question

"Where atoms are".

	Energy (meV)	**Temperature** (K)
Ultracold	< 0.1	< 1
Cold	0.1 - 10	1 - 120
Thermal	10 - 100	120 - 1000
Hot	100 - 500	1000 - 6000
Epithermal	> 500	> 6000

Table 5.2: Neutron categories depending on their energy

5.2 Deep Inelastic Neutron Scattering theory

Deep Inelastic Neutron Scattering (DINS) was first proposed by Hohenberg and Platzmann [85], and Ivanov and Sayasov [86, 87], in 1966, to directly observe the distribution of atomic momentum in condensed matter systems. Presently, it represents the only effective technique to perform measurements of single-particle dynamical quantities, such as atomic momentum distribution and mean kinetic energy.

DINS events are characterized by large energy and momentum transfers and the method relies on the impulse approximation which considers the struck particle as a free particle.

5.2.1 The impulse approximation

The double differential cross section for neutron scattering by a system of N identical atoms can be simply expressed in terms of the dynamic structure factor, $S(\mathbf{q},\omega)$, via [88]:

$$\frac{d^2\sigma}{d\Omega dE_1} = \frac{N}{\hbar}\left(\frac{k'}{k}\right)\left[|b|^2 S(\mathbf{q},\omega) + (|b^2| - |b|^2) S_I(\mathbf{q},\omega)\right], \tag{5.1}$$

where b is the bound atomic scattering length, $\hbar\omega$ and $\hbar\mathbf{q}$ are the energy and momentum transferred by the neutron to the struck atom and k, k' are the incident and scattered neutron wave vectors respectively.
The dynamic structure factor is given by:

$$S(\mathbf{q},\omega) = \frac{1}{2\pi}\int_{-\infty}^{+\infty} dt\; e^{-i\omega t} F(\mathbf{q},t), \tag{5.2}$$

where $F(\mathbf{q},t)$ is related to the correlation function $Y_{i,j}(\mathbf{q},t)$ through

$$F(\mathbf{q},t) = \frac{1}{N}\sum_{i,j} Y_{i,j}(\mathbf{q},t), \tag{5.3}$$

where the indexes i,j run over all the nuclei and

$$Y_{i,j}(\mathbf{q},t) = \langle e^{-i\mathbf{q}\widehat{\mathbf{r}}_i(0)} e^{+i\mathbf{q}\widehat{\mathbf{r}}_j(t)}\rangle. \tag{5.4}$$

The brackets denote a thermodynamic average, and $\widehat{\mathbf{r}}$ is the position operator of nuclei in the Heisenberg representation.
In DINS experiments, the scattering geometry is chosen such that the wavevector transfer q is high enough to treat the problem in the incoherent approximation. Hence the interference effect in equation (5.3) can be neglected and the scattering event is

considered to occur from a single particle. In this case, just the incoherent dynamic structure factor has to be retained:

$$S_I(\mathbf{q},\omega) = \frac{1}{2\pi}\int_{-\infty}^{+\infty} dt\; e^{-i\omega t}\langle e^{-i\mathbf{q}\widehat{\mathbf{r}}(0)} e^{+i\mathbf{q}\widehat{\mathbf{r}}(t)}\rangle. \tag{5.5}$$

For high momentum transfers, the scattering event occurs in a time interval τ short enough that the scattering atom can be considered as it were a free particle. This is the Impulse Approximation (IA) (exactly valid for $q \to \infty$) and is based on the assumption that the interatomic forces among the scattering atom and the other ones can be neglected in its final state. Within this approximation we can replace $\widehat{\mathbf{r}}(t)$ by:

$$\widehat{\mathbf{r}}(t) = \widehat{\mathbf{r}}(0) + \frac{t}{M}\widehat{\mathbf{p}}(0), \tag{5.6}$$

where M is the mass of the scattering nucleus and $\widehat{\mathbf{p}}$ is the momentum operator. By exploiting standard commutation relations between position and momentum operators, the single particle correlation function can be expressed as [89]:

$$Y_{i,i}(\mathbf{q},t) = \exp\left(i\frac{\hbar}{2}\frac{tq^2}{M}\right)\left\langle \exp\left(\frac{it}{M}\mathbf{q}\cdot\widehat{\mathbf{p}}\right)\right\rangle. \tag{5.7}$$

We can now substitute the thermodynamic average with an integral over the momentum states

$$\left\langle \exp\left(\frac{it}{M}\mathbf{q}\cdot\widehat{\mathbf{p}}\right)\right\rangle = \int d\mathbf{p}\; n(\mathbf{p})\exp\left(\frac{it}{M}\mathbf{q}\cdot\mathbf{p}\right), \tag{5.8}$$

where $n(\mathbf{p})$ is the single particle momentum distribution; from equations (5.5), (5.7) and (5.8), by performing the integration over time t, the impulse approximation for the dynamic structure factor is simply obtained [88]:

$$S_{IA}(\mathbf{q},\omega) = \int d\mathbf{p}\; n(\mathbf{p})\delta\left(\omega - \omega_r - \frac{\hbar\mathbf{q}\cdot\mathbf{p}}{M}\right), \tag{5.9}$$

where $\hbar\omega_r = \frac{\hbar^2 q^2}{2M}$ is the recoil energy, i.e. the energy the struck particle would have providing it were stationary and absorbed all the momentum transferred by the neutron. It gives the center of the observed peak at a given q associated to the particle of mass M. Since the position of the peak depends on M, different mass particles in the sample can be distinguished in the observed spectrum. The δ-function in equation (5.9) represents the conservation of kinetic energy and momentum for the system neutron+particle.

5.2.2 Y-scaling

In 1975, in the framework of electron scattering, West introduced a scaling variable, y, which represents the component of $\mathbf{p}$ along the scattering direction [90]. This variable, known as West scaling variable, couples the two dynamic quantities q and ω through the relation:

$$y = \frac{M}{\hbar q}(\omega - \omega_r). \tag{5.10}$$

The dynamic structure factor of equation (5.9) can hence be written as:

$$S_{IA}(\mathbf{q}_\infty, \omega) = \frac{M}{\hbar q} J(y, \widehat{q}), \tag{5.11}$$

where $J(y, \widehat{q})$ is called neutron Compton profile and is formally the Radon transform of the momentum distribution [91]:

$$J(y, \widehat{q}) = \hbar \int d\mathbf{p} n(\mathbf{p}) \delta(\hbar y - \mathbf{p} \cdot \widehat{q}). \tag{5.12}$$

It represents the probability for an atom to have a momentum parallel to $\widehat{q}$ with magnitude between $\hbar y$ and $\hbar(y + dy)$. For an isotropic system like a liquid, the dependence from the direction $\widehat{q}$ is irrelevant and equation (5.12) becomes

$$J(y) = 2\pi\hbar \int_{|\hbar y|}^{\infty} dp\ p\ n(p). \tag{5.13}$$

By inverting this equation, from the neutron Compton profile of an isotropic system, the momentum distribution can be reconstructed by:

$$n(p) = -\frac{1}{2\pi\hbar^3 y} \frac{d}{dy} J(y)|_{y=p}. \tag{5.14}$$

The single particle mean kinetic energy, $\langle E_K \rangle$, is related to the second moment of the Compton profile via:

$$\int_{-\infty}^{+\infty} dy\ y^2\ J(y) = \sigma^2 = \frac{2M}{3\hbar^2} \langle E_K \rangle. \tag{5.15}$$

The properties of $J(y)$ when $q \to \infty$ are known as y-scaling and the presence or absence of y-scaling in the experimental data can be interpreted as a test for the validity of the impulse approximation. Some of these properties are now listed [92]:

- the magnitude of $S(\mathbf{q}, \omega)$ is proportional to $1/q$ for a fixed y,
- the width of $S(\mathbf{q}, \omega)$ is proportional to q,

- the physical interpretation of the $J(y)$ as a probability distribution for atomic momenta implies that $J(y)$ has to be an even function of y with its maximum value at $y = 0$.

We also recall a useful relation among the initial and final neutron velocities [92]:

$$\frac{v_1}{v_0} = \frac{\cos(2\theta) + [(\frac{M}{m})^2 - \sin^2(2\theta)]}{\frac{M}{m} + 1}, \tag{5.16}$$

where m and M are the neutron and the recoiling atom masses, respectively. It has to be noted that, scattering from hydrogen atoms, with $M = m$, occurs only in the angular range $2\theta < 90°$.

5.2.3 Limits of the Impulse Approximation and Final State Effects

Now we want to illustrate the physical meaning of the assumptions implicit in the IA and the range of validity of this approximation, which is exact for an infinite momentum transfer.

The applicability of the IA relies on two main assumptions:

1. the scattering is incoherent, i.e. the scattering is insensitive to correlation between neighboring atoms,

2. the struck atom behaves as a free recoiling particle.

The first assumption is valid provided the nearest-neighbor distance is much greater than $2\pi/q$, so that the interference of the scattering amplitudes from the atoms averages to zero. In typical experiments on VESUVIO, that is the spectrometer exploited for our measurements which will be described in the next section, this condition is well satisfied.
The second assumption is strictly related to the short time approximation in equation (5.6). A characteristic time τ is associated to the scattering event and, at high momentum transfer q, can be expressed by:

$$\tau = \frac{M}{q\Delta p}, \tag{5.17}$$

where Δp is the width of the momentum distribution of the struck particle. Detailed discussions about this "scattering time" can be found in [92, 93, 94]. Providing there are no significant deviations from a free motion in the time interval τ, then the IA will hold. In the case of molecular systems, if the characteristic times of the intra and inter molecular motions are well separated, two distinct regimes of validity for the IA can be considered:

- neutron energy larger than the average collective excitation energy, but smaller than the minimum internal single-particle excitation energy
- neutron energy larger than all the internal excitations of the molecules.

In the first case, the molecular system recoils with a mass equal to the mass of the molecule and the translational kinetic energy of the whole molecule can be measured. In the second regime, scattering occurs from the single nuclei of the molecule and both the translational kinetic energy of the whole molecule and the roto-vibrational motion of the nuclei within the molecule have to be considered.

Real experiments are always performed at finite wavevector transfers q, and some deviations from the IA occur; they are generally referred to as Final Sate Effects (FSE)[1]. These effects are due to the confinement of the recoiling particle by the surrounding atoms, through the inter-particle potential V, and make the neutron Compton profile dependent on the finite wavevector transfer q:

$$J(y, \widehat{q}) \rightarrow J(y, \mathbf{q}). \tag{5.18}$$

According to Sears [93], deviations from the IA can be accounted for through a series of powers of $1/q$:

$$J(y, \mathbf{q}) = J(y) - \frac{A_3}{q}\frac{d^3}{dy^3}J(y) + \frac{A_4}{q^2}\frac{d^4}{dy^4}J(y) + \dots \tag{5.19}$$

A_3 and A_4 are related to the inter-particle potential via [93]:

$$A_3 = \frac{M}{36\hbar^2}\langle \nabla^2 V \rangle \qquad \text{and} \qquad A_4 = \frac{M^2}{72\hbar^4}\langle (\overrightarrow{\nabla} V)^2 \rangle, \tag{5.20}$$

where the brackets stand for statistical averages. Considering typical values of condensed matter inter-particle potentials, FSE are strongly reduced if the wavevector transfer exceeds 20 Å^{-1} that is a regime easily attainable on the VESUVIO spectrometer.

5.2.4 Born-Oppenheimer potential

The momentum distribution is also a sensitive probe of the local environment of the scattering system, as explained in detail in [92, 96]. In some cases, when the temperature is low enough so that the target atom is in its ground state and surrounded by heavy nuclei, many body effects can be neglected and the environment can be described by an effective one-particle potential. It is then possible to reconstruct the

[1]The Impulse Approximation makes assumptions about the way in which is treated the initial state of the system too, as discussed in [95].

spatial wavefunction and the Born-Oppenheimer potential of the scattering atoms as follows [96]:

$$n(\mathbf{p}) = \frac{1}{(2\pi^3)} | \int d\mathbf{r}\psi(\mathbf{r}) \exp(i\mathbf{pr})|^2, \tag{5.21}$$

where $\psi(\mathbf{r})$ is the ground state wave function of the target nucleus. Under the assumption that the ground state momentum wave functions, $\psi(\mathbf{p})$, are real, they may be taken to be $\psi(\mathbf{p}) = \pm\sqrt{n(\mathbf{p})}$. The potential may then be found from:

$$V(r) = E - \frac{\int d\mathbf{p}\ \frac{p^2}{2M} \exp(i\frac{\mathbf{p}\cdot\mathbf{r}}{\hbar})\psi(\mathbf{p})}{\int d\mathbf{p}\ \exp(i\frac{\mathbf{p}\cdot\mathbf{r}}{\hbar})\psi(\mathbf{p})}. \tag{5.22}$$

5.3 Deep Inelastic Neutron Scattering technique

The instrumentation to perform neutron experiments is composed of several parts. The sources are divided in reactors and spallation sources, while the instruments can almost be grouped in diffractometers and spectrometers. Diffractometers look at neutrons that are scattered elastically from the sample; they are used to measure atomic structures of crystals or to study short-range order in disordered materials such as liquids and amorphous metal alloys.

Inelastic neutron scattering experiments, where the energy of neutrons changes after the interaction with the sample, are instead performed by the use of spectrometers.

5.3.1 ISIS: a pulsed neutron source

In the past, neutrons could be produced only by reactors but, in the last decades, a new kind of neutron sources has become available, based on the spallation process. In a spallation neutron source a heavy metal target is bombarded by pulses of energetic protons produced by powerful accelerators. In this way intense pulses of neutrons can be obtained with only a limited heat production in the target. On the contrary, one of the major drawbacks of reactors is the intense heat production in the core and this is also the main limit to further technological developments of this traditional reactor sources. Another important advantage of a pulsed source is that neutrons can be obtained in a wide range of energies that includes also epithermal neutrons, with energies greater than 500 meV.

ISIS is a spallation neutron source at the Rutherford Appleton Laboratory (Chilton-Didcot, UK)[2]. The production of neutron proceeds in this way: intense beams of protons, accelerated up to 800 MeV, bombard a heavy metal tantalum target; the hitted target nuclei are promoted to highly excited states, then they release the energy by evaporating some nucleons, most of all neutrons, that can leave the target or trigger

[2]http://www.isis.rl.ac.uk/

further reactions. For each proton hitting the target, approximately 30 neutrons are produced.

These neutrons have very high energies and hence velocities and, in order to use them for condensed matter studies, they must be slowed down by some moderators. Exploiting the large scattering cross section of hydrogen, neutrons at ISIS are undermoderated by surrounding the target with hydrogenous moderators such as ambient temperature water (316 K), liquid methane (100 K) or liquid hydrogen (20 K).

The spectral distribution of the produced neutrons depend on the moderators temperature and can be tailored for different kind of experiments. As an example, the energy spectrum of the neutron beam after crossing the ambient temperature water moderator is shown in figure 5.1 [97].

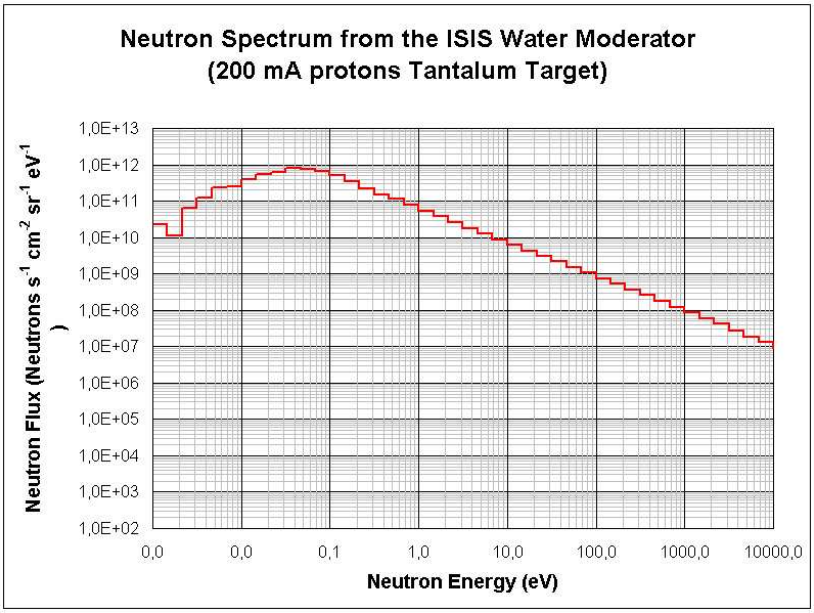

Figure 5.1: Energy spectrum of the neutron beam from the ambient temperature water moderator, at the ISIS spallation neutron source.

5.3.2 Direct and inverse geometry spectrometers

Inelastic neutron scattering experiments aim at measuring the intensity of the scattered neutrons as a function of the energy, $\hbar\omega$, and of the momentum, $\hbar q$, transferred from the incident neutrons to the sample; these measurements are obtained by spectrometers which, at a pulsed neutron source, operate via the time of flight technique.
To obtain the energy and the momentum transfers we should know the scattering angle,

2θ (see figure 5.2), and the incident and scattered neutrons velocities, v_0 and v_1,

$$\hbar\omega = E_0 - E_1 = \frac{1}{2}m(v_0^2 - v_1^2), \tag{5.23}$$

and

$$\hbar q = \hbar|\overrightarrow{k_0} - \overrightarrow{k_1}| = \hbar\sqrt{k_0^2 + k_1^2 - 2k_0k_1\cos(2\theta)} = m\sqrt{v_0^2 + v_1^2 - 2v_0v_1\cos(2\theta)}. \tag{5.24}$$

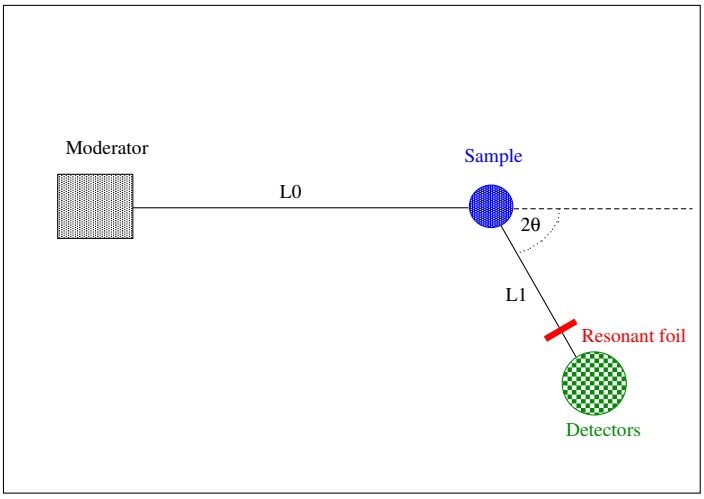

Figure 5.2: Schematic view of an inverse geometry spectrometer (the resonant foil monochromate the final neutron energy, as explained in the following section).

The time of flight technique consists in the measurement of the total time of flight for a neutron traveling from the moderator to the detector (see figure 5.2), given by

$$t = \tau + \frac{L_0}{v_0} + \frac{L_1}{v_1}, \tag{5.25}$$

where τ is the time delay introduced by the instrument electronics, L_0 is the distance from the moderator to the sample, L_1 is the distance from the sample to the detector and v_0 and v_1 are the incident and scattered neutron velocities. From the knowledge of the flight paths L_0 and L_1 and one of the neutron velocities (v_0 or v_1), and from the measurement of the total time of flight t, it is possible to obtain both the transferred energy and the transferred momentum.

Neutron spectrometers are conventionally divided in two categories depending on the energy selection: direct and inverse geometry instruments. Direct geometry spectrometers fix the incident neutron energy while in inverse geometry instruments the

final neutron energy is selected and the incident velocity is determined from t.
For a direct geometry spectrometer, where E_0 is fixed and $E_1 = E_0 - \hbar\omega$, from eq. (5.24) is simple to obtain

$$\frac{\hbar^2 q^2}{2m} = 2E_0 - \hbar\omega - 2\sqrt{E_0(E_0 - \hbar\omega)}\cos(2\theta). \tag{5.26}$$

For an inverse geometry spectrometer, E_1 is fixed and $E_0 = E_1 + \hbar\omega$ and eq. (5.26) becomes

$$\frac{\hbar^2 q^2}{2m} = 2E_1 + \hbar\omega - 2\sqrt{E_1(E_1 + \hbar\omega)}\cos(2\theta). \tag{5.27}$$

The main kinematic difference that arises from this two formulas is that in a direct instrument the energy loss is limited to E_0 while there is no upper limit, within the maximum energy of the incident neutron beam, to the transferred energy for an inverse geometry spectrometer. This is evidenced in figure 5.3 where the contour plots of equal scattering angles are plotted as a function of momentum and energy transfers both for a direct and for an inverse geometry instrument. For a complete description of neutron scattering instruments, see for example [98, 88].

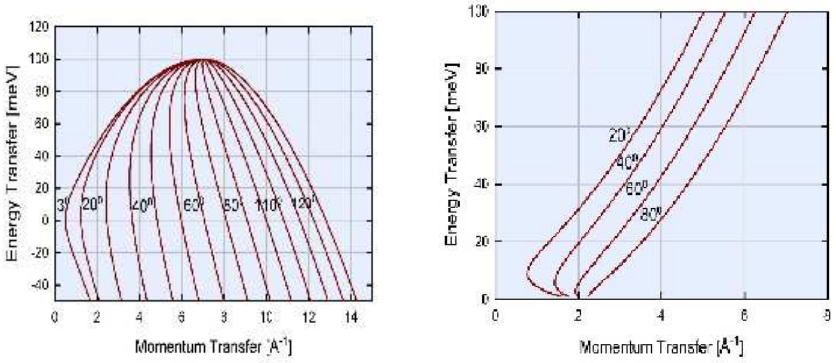

Figure 5.3: Contour plots of equal scattering angles as a function of momentum and energy transfers for a direct geometry instrument (on the left panel) and for an inverse geometry instrument (on the right panel).

5.3.3 Resonance foil technique

Both direct and inverse geometry spectrometers need to select a neutron energy window either in the primary beam, for direct geometry instruments, or in the secondary path, for inverse geometry ones. There are mainly three methods of energy selection in common use:

1. exploiting the Bragg's law of reflectivity with single crystals,

2. placing a chopper in the incident beam,

3. using the resonance foil technique.

The first two methods have the main drawback in the limited upper value of possible selected energies; in fact reflectivity of crystals decreases rapidly with increasing energies and the maximum rotational speed of choppers allows to select energies up to about 2 eV [98].

The resonance foil technique, exploited in this thesis work, consists in placing in the beam a nuclear resonance absorption foil which strongly absorb neutrons over narrow energy ranges. The absorption foil is usually cycled in and out of the neutron path and two measurements (with and without the foil) are taken. The difference between these two data sets provides the measurement of the neutrons with energy determined by the foil resonance. The resonance foil technique can be used to obtain neutron energy transfers up to 100 eV, depending on the choice of the resonance foil. It turns out that much better resolution can be obtained if the resonance foil method is employed on an inverse geometry instrument, with the foil in the secondary flight path [3], and this is actually the method employed at ISIS on the VESUVIO spectrometer.

5.3.4 VESUVIO spectrometer

VESUVIO[4] is an inverse geometry neutron spectrometer operating at the ISIS pulsed source since the year 2002. It exploits the resonance foil technique to monochromate the scattered neutron energy and the standard time of flight technique to determine the incident energy of neutrons. With this instrument, energy transfers in the range (1-100) eV and momentum transfers between 5 $Å^{-1}$ and 200 $Å^{-1}$ are achieved [100, 101]. The VESUVIO spectrometer is equipped both with ^6Li glass scintillators to reveal directly the scattered neutrons and with γ scintillators, as the YAP ($YAlO_3$) detectors, in the resonance detector (RD) configuration. We will describe just the first technique, in the experimental arrangement which has been used in this thesis work; details about the resonance detector technique can be found in [102].

When neutron detectors (such as ^6Li glass scintillators) are employed, two experimental arrangement are possible: the Single Difference (SD) method and the Double Difference (DD) method. In the "resonant filter - single difference" configuration, two measurements are taken, the first one with the absorbing filter between the sample and the detector and the second one without the foil. The raw data are given by the

[3] A comparison of the efficiency of the resonance foil technique on direct and inverse geometry instruments can be found in [99]

[4] http://www.isis.rl.ac.uk/molecularSpectroscopy/vesuvio/

difference among these two measurements.
The second experimental arrangement, known as Double Difference (DD) method, consists in taking three measurements: one without the resonant foil and the other two with two filters of different thickness. In this way better resolutions are reached but at the price of lower count rates. For a detailed description of these techniques see, for example, [103].

The resolution function of an inverse geometry spectrometer exploiting the resonance foil technique, as VESUVIO, is mainly due to two components [104]: a first one (geometrical) related to the uncertainties in the neutron flight paths, scattering angles and time of flight measures and a second one generated by the resonance width of the analizer foil. The geometrical component is constituted by several distinct distribution and is assumed to be Gaussian. The energetic component can instead be modeled by a Voigt function given by the convolution of a Gaussian and a Lorentzian function. The former takes into account the Doppler broadening coming from the lattice motion while the latter is due to the intrinsic shape of the nuclear resonance of the foil. This term of the model represents the main resolution limitation because of its extensive wings and its infinite second moment.
Since the functional form of the wings scales with the thickness of the foil, it is possible to overcome this problem via the DD method, by an appropriate weighted difference of two measurements with foils of different thickness. In this way, a finite second moment of the energetic component and much narrower resolution functions are obtained, even if at the expenses of the count rates.

Chapter 6

Sample description and experimental details

In this chapter we will provide details about the Deep Inelastic Neutron Scattering experiments that have been performed in order to study the single particle dynamics of confined water. In the first part of the chapter we will illustrate the samples characteristics and preparation, from the synthesis to the hydration procedure. We will then give a detailed description of the instruments and of the experimental setup exploited in these experiments.

6.1 The sample: water confined in nanoporous xerogel matrices

This part of the thesis regards the study of the single particle dynamics of water confined in silica xerogel matrices. In particular we examined the momentum distribution of the protons by embedding water in the pores of xerogel powders. We analyze samples with two different pore dimensions, namely xerogel with average pore diameter d=24 $\pm$ 7 Å and d=82 $\pm$ 11 Å; for both sizes, measurements were performed on the hydrated sample and on the dry powder too.

6.1.1 Xerogel synthesis and characterization

Silica xerogel are transparent materials which can be produced in a wide range of macroscopic densities with controlled porosity. They are obtained by porous glasses originally produced from *Sol-Gel* bulk samples. In the *Sol-Gel* process the starting components are metalloid elements, like tetraethoxysilane (TEOS) or tetramethylorthosilicate (TMOS) surrounded by various solvents as water and ethanol [105]. Specific catalysts and control chemicals are often added in order to improve the process. Final solutions are then stirred and stored at room temperature for some weeks, in order to

Alkoxide precursor	**Average pore size** (Å)	**Total pore volume** (cm^3/g)	**Specific surface area** (m^2/g)
TEOS	24	0.348	727
TMOS	82	1.10	500

Table 6.1: Physical parameters of the two xerogel samples used in the experiments, as derived from BET analysis [107].

complete the polymerization process. The final drying process gave rise to the dried *gel*, called xerogel.

Our samples have been synthesized at the NEMO Laboratory[1] at the Physics Department of the University of Rome Tor Vergata. The synthesis procedure involved different alkoxide precursors (both TEOS and TMOS), water and ethanol solvents, nitric acid as catalyst and different control chemicals and give rise to two different xerogel samples, with average pore diameters $d = 24\,\text{Å}$ and $d = 82\,\text{Å}$. Both samples, after the drying treatment, have been grinded and reduced to powders. Details about the synthesis procedure can be found in [106].

After grinding, the xerogel powders are formed by little spheres which present a microporous structure. Their characterization can be obtained in terms of both pore size distribution and surface area, via an analysis named Brunauer-Emmet-Teller (BET) [107], based on the measurements of the N_2 adsorption/desorption isotherms. The BET analysis on our xerogel powders have been realized at the University of Trento and give the results listed in table 6.1.

6.1.2 Xerogel hydration

Xerogel powders are hygroscopic materials, i.e. when exposed to air, they tend to adsorb water vapour until equilibrium is reached. Obviously, this process occurs just if the vapour pressure of water inside the xerogel is lower than the one relative to the atmosphere the powder is exposed to.
For both our samples, water has been adsorbed in dry xerogel powder by an hydration protocol in a controlled environment. The hydration procedure made use of three Petri dishes filled with dry xerogel powder and a fourth Petri dish containing a saturated solution of potassium nitrate (KNO_3) and water; all dishes were introduced in a desiccator to ensure an insulated environment during all the hydration process time. The sample was maintained in this controlled environment for about 96 hours, saturated with aqueous solution of KNO_3. The level of hydration was determined by weight measurements. Once the equilibrium between the xerogel and the solution was

[1] http://optoweb.fis.uniroma2.it/opto/index.html

Average pore size (Å)	**Hydration level** %	**Pore filling** %
24	26.4	76
82	108	98

Table 6.2: Hydration parameters of the two xerogel samples used in the experiments. The hydration level is defined as the ratio between water and dry xerogel weights.

reached, the xerogel with pore size of 24 Å and 82 Å were hydrated at a water content of 26.4% and 108 % of the dry weight, respectively. Due to the hygroscopic properties of materials with these pore dimensions, one can assume that water is completely adsorbed by the pores of the powders. Assuming the water molecule to be a sphere with diameter of 3.16 Å, the corresponding pore filling values can be calculated: 76% and 98% for xerogel with average pore size of 24 Å and 82 Å, respectively (see table 6.2).

6.2 Experimental setup

DINS experiments on confined water have been performed on the inverse geometry spectrometer VESUVIO at the ISIS spallation neutron source[2]. This spectrometer allows to explore a range of energy and momentum transfers with $\hbar\omega > 1$eV and $q > 25\,\text{Å}^{-1}$. In order to measure the proton momentum distribution, looking at equation (5.16) about the scattering from hydrogen atoms, detector banks with ^{6}Li detectors in forward scattering direction have been used. The final energy has been determined via the resonance filter technique in the single difference configuration, using a gold analyzer foil. All samples were contained in flat cylindrical Al cans, with section diameter of 5 cm and internal thickness of 0.1 cm. The main parameters of the experimental setup of VESUVIO are summarized in table 6.3.

6.2.1 Detectors

Neutron detection has been achieved through the use of ^{6}Li glass detectors at forward scattering direction. Four banks of 8 detectors each have been used covering the angular range between 30° and 70°. They were placed at a distance of about 0.7 m from the sample and 0.35 m from the gold analyzer foil. The exact angular positions and distances from the sample[3] are listed in table 6.4 for all the 32 detectors.

Lithium glass detectors are scintillation type detectors which emit light in response to the excitation due to ionizing radiation [108, 102] and are suitable for neutron

[2]A detailed description of the neutron source and of the spectrometer is given in chapter 5.

[3]These numbers are listed in the experimental IPfile which is assigned at each experiment: 0621 and 0711 for the measure on the xerogel 24 Å and 82 Å, respectively.

VESUVIO experimental setup	
Instrument	inverse geometry spectrometer
Energy selection	resonance foil technique
Neutron detectors	32 ^{6}Li detectors
Detectors angular range	$30° - 70°$
Initial flight path L_0	11.055m
Final flight path L_1	~ 0.7m
Recoil momentum transfer	$q_{rec} > 30\,\text{Å}^{-1}$

Table 6.3: Main parameters and characteristics of the VESUVIO spectrometer exploited in the experiments for the measurement of confined water momentum distribution.

detection. These detectors are silicate-based glasses which contain small percentage of lithium (enriched in the isotope ^{6}Li) and of an activator species, like an oxide of cerium. The detectors used in our experiments had a surface of $25\,\text{cm}^2$ and a thickness of 10 mm.

The pulses from the scintillator are then collected in a photomultiplier through an aluminum light guide and hence stored by the Data Acquisition Electronics (DAE) [108].

6.2.2 Resolution functions

In the last chapter, in section 5.3.4, we described the functional form of the resolution of an inverse geometry spectrometer exploiting the resonance foil technique, like VESUVIO. This instrument can operate in two distinct configurations, namely in the single difference and in the double difference configurations. DINS experiments on confined water have been performed exploiting the resonance foil technique in the single difference configuration. The resonance foil was a gold ^{197}Au filter of 3 mm thickness; its resonance shape is shown in figure 6.1. The resolution of this kind of spectrometers has a geometrical component, due to the uncertainties in the neutron flight paths, scattering angles and time of flight measures and an energetic component related to the nuclear resonance of the foil. The geometrical component is assumed to be Gaussian, $G_{geom}(y)$. The energetic component is instead a Voigt function given by the convolution of an intrinsic Lorentzian lineshape, $L(y)$, and of a Gaussian function that takes into account the Doppler broadening coming from the lattice motion, $G_{Dopp}(y)$.

For the gold analyzer foil, the Breit-Wigner nuclear resonance can be approximated

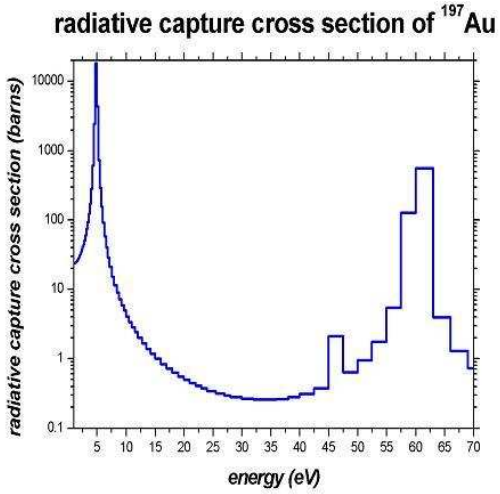

Figure 6.1: Nuclear resonance lineshape for a gold (^{197}Au) foil.

by a Lorentzian of the form:

$$L(E) = \frac{1}{\pi}\left[\frac{\frac{\Gamma_E}{2}}{(\frac{\Gamma_E}{2})^2 + (E - E_1)^2}\right], \tag{6.1}$$

where E_1 is the resonance energy and $\frac{\Gamma_E}{2}$ is the resonance Half Width at Half Maximum (HWHM). The overall resolution function, for each individual detector, can hence be expressed as the convolution of the Gaussian and of the Lorentzian contributions, as

$$R(y,q) = G(y,q) \otimes L(y,q) = \int d\eta\, G(\eta,q) L(y-\eta,q); \tag{6.2}$$

from now on, with the symbol $\otimes$ we will denote the convolution with respect to the y variable. $G(y,q)$ is in turn the convolution of all the gaussian components

$$G(y,q) = G_{geom}(y,q) \otimes G_{Dopp}(y,q). \tag{6.3}$$

The q dependence derives from the fact that the wavevectors transfer accessible in real experiments are always finite (see section 5.2.3). Parameters characterizing the resolution function for each detector are listed in table 6.4.

Xerogel, 24 Å pore size					Xerogel, 82 Å pore size				
2θ (degree)	L_1 (m)	$\bar{q}$ (Å^{-1})	σ_G (Å^{-1})	$\frac{\Gamma_E}{2}$ (Å^{-1})	2θ (degree)	L_1 (m)	$\bar{q}$ (Å^{-1})	σ_G (Å^{-1})	$\frac{\Gamma_E}{2}$ (Å^{-1})
32.1	0.704	30.6	0.71	1.24	32.5	0.689	31.2	0.67	0.74
33.8	0.692	32.6	0.71	1.18	33.6	0.691	32.4	0.67	0.71
34.5	0.699	33.5	0.70	1.14	34.4	0.688	33.4	0.67	0.69
35.9	0.684	35.3	0.71	1.08	35.6	0.685	35.0	0.67	0.66
36.6	0.695	36.3	0.69	1.06	36.4	0.678	36.0	0.68	0.64
38.2	0.687	38.3	0.69	1.00	37.5	0.685	37.7	0.67	0.62
38.7	0.682	39.1	0.70	1.00	38.2	0.686	38.7	0.67	0.60
40.0	0.680	40.9	0.69	0.94	39.7	0.674	40.5	0.67	0.57
40.7	0.698	42.0	0.68	0.92	40.4	0.684	41.9	0.66	0.56
42.0	0.697	43.9	0.67	0.88	41.7	0.669	43.6	0.68	0.54
43.0	0.689	45.4	0.68	0.86	42.5	0.684	45.0	0.66	0.52
44.4	0.694	47.7	0.67	0.82	43.9	0.687	47.0	0.66	0.50
45.0	0.693	48.8	0.67	0.80	44.7	0.688	48.4	0.66	0.49
46.3	0.697	51.0	0.67	0.76	45.7	0.693	50.5	0.65	0.47
47.2	0.690	52.7	0.67	0.74	46.7	0.690	52.2	0.65	0.45
48.4	0.703	55.1	0.66	0.71	47.7	0.685	54.1	0.66	0.44
51.5	0.691	61.4	0.66	0.64	51.2	0.688	61.6	0.65	0.39
52.7	0.696	64.1	0.65	0.62	52.7	0.693	64.5	0.65	0.37
52.9	0.695	64.7	0.66	0.61	53.4	0.682	66.5	0.66	0.36
53.6	0.692	66.3	0.66	0.60	54.7	0.680	69.6	0.66	0.34
54.7	0.683	69.1	0.66	0.57	55.3	0.680	71.9	0.66	0.34
55.8	0.686	71.8	0.66	0.55	56.8	0.692	75.3	0.64	0.32
56.8	0.686	74.6	0.66	0.53	57.4	0.679	77.5	0.66	0.31
57.9	0.678	77.8	0.66	0.51	58.9	0.680	81.5	0.65	0.30
59.2	0.697	81.9	0.65	0.49	59.6	0.670	84.3	0.66	0.29
59.9	0.684	84.3	0.66	0.48	60.9	0.689	88.4	0.65	0.28
61.2	0.690	89.1	0.65	0.45	61.6	0.679	91.9	0.66	0.27
61.9	0.684	91.5	0.66	0.44	62.9	0.688	96.4	0.65	0.26
63.3	0.700	97.5	0.64	0.42	63.8	0.680	100.4	0.65	0.25
64.5	0.692	102.8	0.65	0.40	64.9	0.692	105.5	0.64	0.24
65.6	0.704	108.1	0.64	0.38	65.7	0.687	110.1	0.65	0.23
67.3	0.709	117.2	0.63	0.34	66.5	0.705	114.0	0.63	0.22

Table 6.4: For each detector, the scattering angle 2θ and the final flight path L_1 are listed, for both xerogel powders. The wavevector transfer $\bar{q}$ corresponding to the maximum of the recoil peak, i.e. to $y = 0$ (see sec. 5.2.2), are also reported. Parameters describing the resolution function $R(y)$ on VESUVIO are also listed: σ_G indicates the standard deviation of the whole Gaussian component (energy plus geometrical contributions) whereas $\Gamma_E/2$ is the Half Width at Half Maximum (HWHM) of the Lorentzian energy contribution.

Chapter 7

Proton microscopic dynamics of confined water

In this chapter we present the results obtained by the DINS experiments we performed on confined water. In the first part of the chapter we illustrate the procedures followed for the initial data reduction. Then we describe all the steps which have characterized the data analysis, stressing the physical meaning of the main assumptions. The last part of the chapter is devoted to the description and discussion of the results.

7.1 Data reduction

DINS experiments on confined water have been performed on the inverse geometry spectrometer VESUVIO at the ISIS spallation neutron source. Detector banks with 32 ^{6}Li detectors in forward scattering direction have been used and the final energy has been determined via the resonance filter technique in the single difference configuration, using a gold analyzer foil. Both hydrated and dry xerogel powders with average pore diameter d of 24 Å and 82 Å have been measured. All samples were contained in flat geometry Al cans. Experimental data were recorded by the DAE; the total integrated proton currents for the various measurements are reported in table 7.1. In the following the reduction procedure applied to these data sets will be described.

7.1.1 Foil-in/foil-out subtraction

As already mentioned, VESUVIO is an inverse geometry spectrometer which allows to perform DINS measurements by selecting the neutron final energy through the resonance filter technique. In the single difference configuration (see also section 5.3.4), two data sets are recorded: the first one with the resonance foil in front of the detectors (foil-in) and the second one without the foil (foil-out). The difference between the foil-in

Sample	Integrated proton current [μAh]
Hydrated xerogel - $d = 24$ Å	22315
Hydrated xerogel - $d = 82$ Å	15473
Dry xerogel - $d = 24$ Å	8578
Dry xerogel - $d = 82$ Å	7811

Table 7.1: Integrated proton currents for the DINS experiments on confined water, for various kind of measurements.

and foil-out data sets provides the measurement of the neutron with energy determined by the filter and constitutes the experimental time of flight (*tof*) spectrum.

The first steps of the data reduction are given by the proper subtraction of the foil-in/foil-out data sets and by a subsequent rebinning and normalization procedure. This part of the reduction has been performed exploiting the standard VESUVIO routines [109] through the commands **ndiff**, **reb** and **norm**. During the foil-in/foil-out subtraction, for each scattering angle, data have been normalized between 550 μs and 600 μs where no recoil peaks are present. This normalization procedure is generally preferred with respect to normalize to incident beam monitor counts; the reason is that small drifts in the monitor detector efficiency, which may occur with time, would introduce a spurious background in the difference spectra.

Examples of time of flight spectra, obtained in this way, are shown in figure 7.1 for three selected values of scattering angles. We can observe that, at each angle, two peaks are present: the first one, at smaller *tof*, is the recoil peak associated to the hydrogen atoms present in the sample, both belonging to water molecules and to silanol groups of the xerogel matrix; the second peak, centered at about 370 μs, is instead due to the recoil from all the heavy masses in the sample (silicon, oxygen and the aluminum from the can). It is worth noticing that the two peaks tend to be closer for smaller scattering angles.

7.1.2 Multiple scattering and non-hydrogenous peak subtractions

Two unwelcome contributions have to be removed from the *tof* spectra: the multiple scattering signal and the non-hydrogenous recoil peak. The small sample thickness (0.1 cm) guarantees a small contribution of multiple scattering signal. This has been evaluated by a Monte Carlo simulation [110] which considers the final neutron energy fixed by the gold analyzer foil at $E_1 = 4908 \pm 148$ meV, takes into account the geometrical parameters of the detectors and of the aluminum can and treats the sample as constituted of hydrogen, oxygen, silicon and aluminum atoms with the proper concentrations. An example of multiple scattering signal obtained by the Monte Carlo

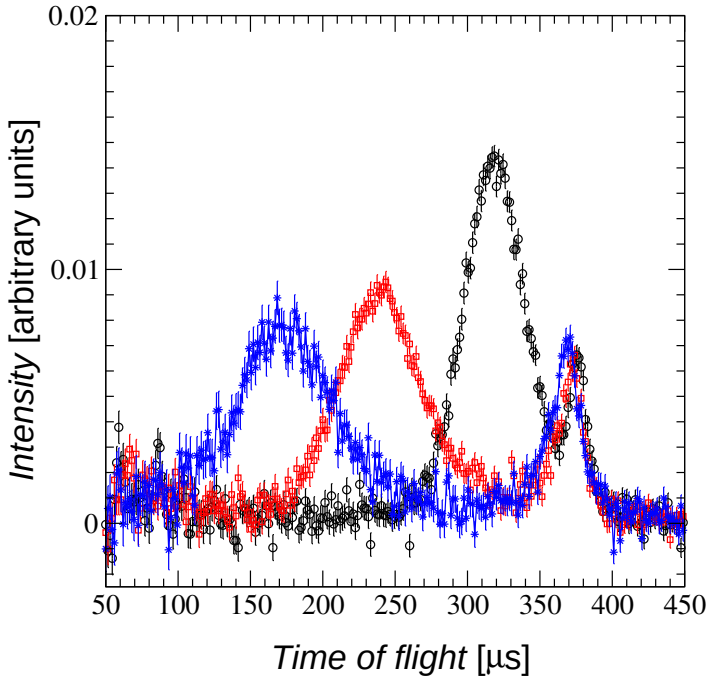

Figure 7.1: Time of flight DINS spectra from water confined in a xerogel powder with average pore size of 24 Å, for three scattering angles: 34.5° (black circles), 52.9° (red squares), 65.6° (blue stars).

simulation is reported in figure 7.2. Second and third order scattering events have been then subtracted for each scattering angle.

In order to obtain spectra with better statistics, data from xerogel powder with average pore diameter of 24 Å, recorded at scattering angles within 2 degrees have been summed together.

The last step of *tof* data reduction consists of subtracting the recoil peak due to the non-hydrogenous masses. This has been done by fitting the data through two close Gaussian or Voigt functions and hence by removing the lineshape of the unwanted peak. Sometimes we noticed the opportunity of fitting the data with a three peaks function (one for the hydrogens and the other two for the other masses) and this is justified by the presence of different masses in the second recoil peak (silicon, aluminum and oxygen).

At the end of the data reduction, we transformed the *tof* spectra in y-spectra (see section 5.2.2). This last step has been done exploiting the standard VESUVIO routine **ytrans**. Examples of y-spectra at three different scattering angles are shown in figure

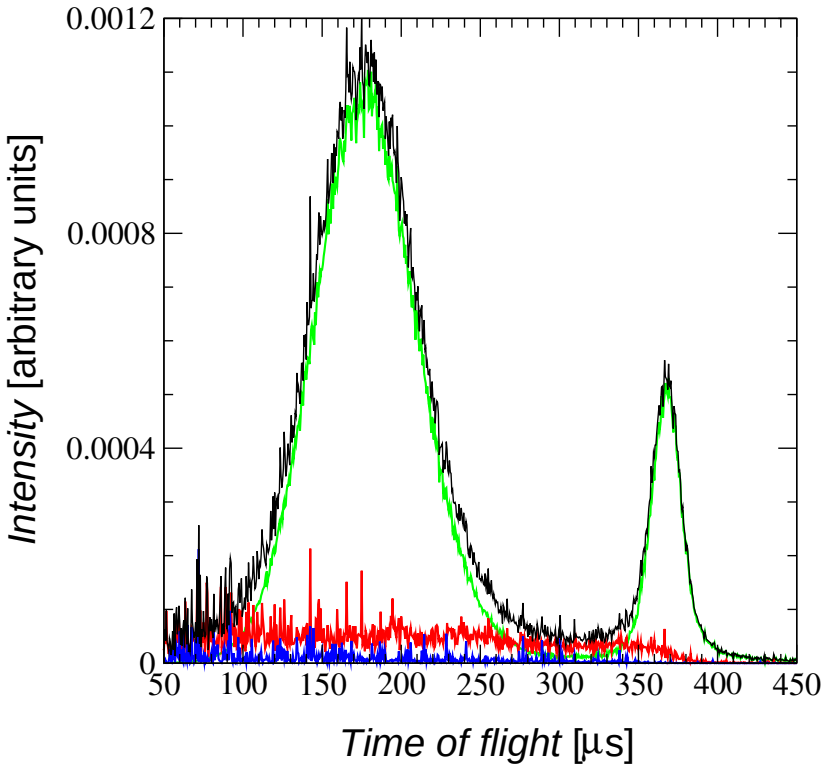

Figure 7.2: DINS spectra obtained from the Monte Carlo simulation. The first (green line) second (red line) and third (blue line) order scattering contributions are shown, together with the total scattering signal (black line).

7.3, for both powders. From this figure one can observe that, by increasing the scattering angle (from top to bottom), the right tail of the spectra (at $y > 0$, corresponding to $tof < 100\mu s$) has a worse statistics; simultaneously the recoil peak moves towards a value centered at $y = 0$, as expected within the Impulse Approximation. It has to be noted that, even for the smaller scattering angles (top panels), the spectra are centered at $y \simeq 0$ and this is the first indication of a likely absence of final state effects.

7.1.3 Spectrometer resolution functions

Within the convolution approximation [92], the experimental response function, $F_n^{exp}(y, 2\theta)$, can be expressed as a convolution of the proton response function, $J(y, 2\theta)$, introduced in section 5.2.2, and of the resolution function, $R_n(y, 2\theta)$:

$$F_n^{exp}(y, 2\theta) = J(y, 2\theta) \otimes R_n(y, 2\theta), \tag{7.1}$$

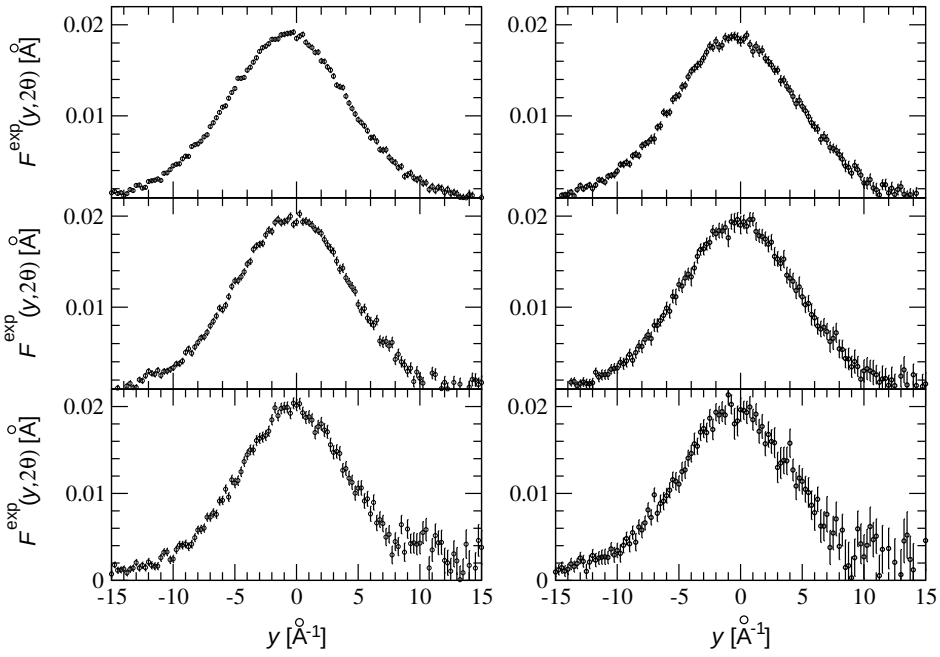

Figure 7.3: Experimental y-spectra, with error bars, for water confined in xerogel with average pore diameter $d = 24$ Å, for three scattering angles: 38.4° (left-top panel), 52.4° (left-central panel), 63.9° (left-bottom panel); and for water confined in xerogel with average pore diameter $d = 82$ Å, for three similar scattering angles: 38.2° (right-top panel), 52.7° (right-central panel), 63.8° (right-bottom panel).

where the index n run over the 32 detectors and 2θ is the scattering angle. Before analyzing the data, we have also generated the experimental resolution functions. Their functional form, given by the convolution of a Gaussian and a Voigt functions has been described in sections 5.3.4 and 6.2.2. To obtain the resolution functions we have exploited the parameters in table 6.4. An example of y-spectrum together with its resolution function is shown in figure 7.4.

7.1.4 Constant q spectra

In order to interpret data in terms of dynamical structure factor and Neutron Compton profile

$$S(q,\omega) = \frac{\hbar q}{M} J(y,q), \tag{7.2}$$

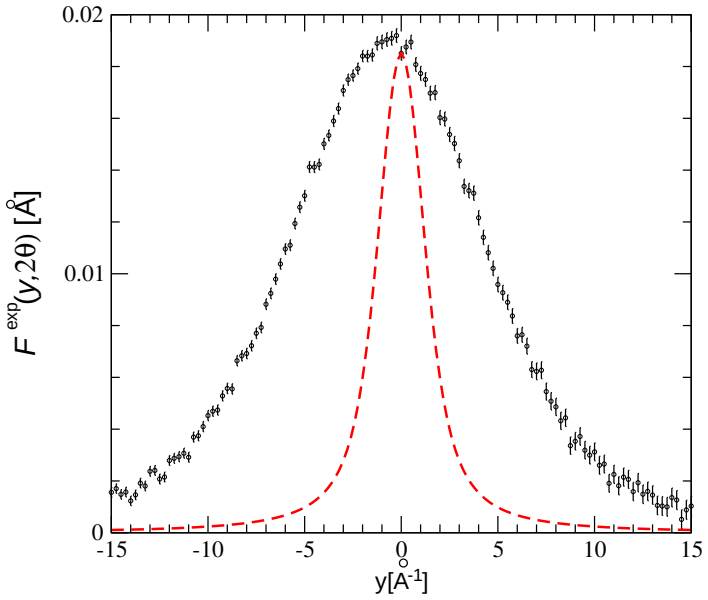

Figure 7.4: Experimental y-spectrum, with error bars, for water confined in xerogel with average pore diameter $d = 24\,\text{Å}$, for a scattering angle $2\theta = 38.4°$; the relative resolution function (red dashed line) is also shown.

where q is fixed, it is useful to express experimental spectra in terms of constant wavevector transfer $\hbar q$. Triple-axis-spectrometers have the advantage to directly record constant q data. On VESUVIO, this goal has been achieved by converting constant angle spectra to constant wavevector ones. This conversion involves the application of the Jacobian factor, always required when there is a change of variables of a function [111]. Since

$$S(q,\omega) = S(2\theta,\omega)\left|\frac{\partial(2\theta)}{\partial q}\right|, \tag{7.3}$$

where $S(2\theta,\omega)$ is the fixed angle dynamical structure factor, then

$$J(y,q) = \frac{q}{M}\left|\frac{\partial(2\theta)}{\partial q}\right| S(2\theta,\omega). \tag{7.4}$$

To this aim, an algorithm has been developed which reads out all the spectra recorded by detectors at different angles and groups together those data with associated momentum transfer within a small window of q values. These constant-q data are then rebinned onto y-bins, weighted by their errors. This procedure transforms intensities versus constant scattering angle to intensities versus constant wavevector transfer in a

unique way, which depends only on the choice of the width in q. A set of four $F_n^{exp}(y,q)$ spectra, in y space, have been obtained for the following values of momentum transfer: $q = 38 \pm 2\,\text{Å}^{-1}$, $q = 45 \pm 2\,\text{Å}^{-1}$, $q = 53 \pm 3\,\text{Å}^{-1}$ and $q = 70 \pm 5\,\text{Å}^{-1}$. An identical procedure has been used to express the resolution function at each individual angle in terms of constant q values. The convolution approximation [92] has then been applied. Examples of $F_n^{exp}(y,q)$ spectra at constant q are shown in figure 7.5 together with the corresponding resolution functions.

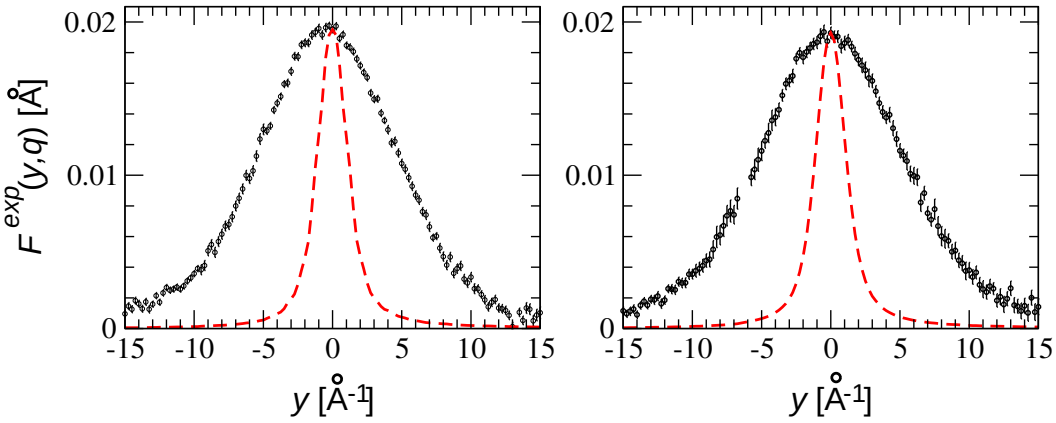

Figure 7.5: Experimental response functions, $F^{exp}(y,q)$ (with error bars) and corresponding resolution functions (dashed lines), for water confined in xerogel with average pore size of 24 Å (left panel) and 82 Å (right panel), at constant momentum transfers $q = 53 \pm 3\,\text{Å}^{-1}$.

7.2 Data analysis

In order to derive the proton momentum distribution and mean kinetic energy, a several steps analysis has been performed. The main objective of this work is to determine the response functions for two distinct kinds of hydrogen atoms, with overlapping recoil peak: hydrogens belonging to water molecules, which are (for our purpose) the more interesting ones, and silanol-hydrogens belonging to the confining xerogel matrix.

At first, the contribution due to silanol-hydrogens have been evaluated using dry xerogel data sets (hereafter indicated with suffix D). A second step consisted in calculating the contributions from both water-hydrogens and silanol-hydrogens using the hydrated xerogel data sets (hereafter indicated with suffix H). The percentage of

silanol-hydrogens with respect to the total number of hydrogens, has then been estimated and a combined analysis of dry and hydrated xerogel data sets allowed to obtain information about water hydrogens only (hereafter indicated with suffix W).

7.2.1 Hydrated and dry samples data analysis

Previous DINS experiments on water [112, 113, 114] have shown that a simple Gaussian model is not adequate to accurately describe the single particle proton dynamics. For this reason, the individual spectra for dry and hydrated xerogel data sets, at both constant wavevector transfer ($F^{exp}(y,q)$) and constant scattering angle ($F_n^{exp}(y,2\theta)$), have been fitted using a general model distribution function [115]. It can be regarded as a non-Gaussian function expressed by a Gaussian lineshape multiplied by a truncated series of even Hermite polynomials, $H_n(x)$, as in equation (7.5).

$$J_{mdf}(y,\chi) = \frac{\alpha}{\sqrt{2\pi\sigma^2}} e^{-u^2} \left[1 + c_4 \frac{2}{3} H_4(u) + c_6 H_6(u) + \ldots \right] \tag{7.5}$$

with χ being 2θ or q, and $u = \frac{(y-y_0)}{\sqrt{2\sigma^2}}$. α is a normalization factor, σ^2 and y_0 are the second moment and the centroid of the Gaussian function, respectively, and c_n are the Hermite polynomials coefficients.

As explained in section 5.2.3, at finite wavevector transfer q, some deviations from the impulse approximation occur, which are generally referred to as Final Sate Effects (FSE). According to Sears [93], these effects can be accounted for through a series of powers of $1/q$. Hence, in order to consider also these deviations from the impulse approximation, we added to the model distribution function of equation (7.5) corrective polynomials multiplied by powers of $1/q$:

$$J_{mdf}(y,\chi) = \frac{\alpha}{\sqrt{2\pi\sigma^2}} e^{-u^2} \left[1 + c_4 \frac{2}{3} H_4(u) + c_6 H_6(u) + \ldots + k_3 \frac{1}{q} H_3(u) + k_4 \frac{1}{q^2} H_4(u) + \ldots \right]. \tag{7.6}$$

In order to fit the experimental spectra, the model distribution function of equation (7.6) have also to be convoluted with the experimental resolution functions:

$$F^{exp}(y,\chi) = J_{mdf}(y,\chi) \otimes R_n(y,\chi). \tag{7.7}$$

This is the distribution function used through all the data analysis in this work and it had been already successfully employed for liquid H_2O [116, 92] and for ice [116]. The fitting parameters are α, y_0, σ, and the Hermite polynomials coefficients c_4, c_6, k_3 and k_4.

In the following, it will be shown that just few terms in the expansion of equation (7.6) have to be retained in order to obtain a good fit of the experimental spectra; in particular, for this case of confined water, we can neglect the FSE terms (asimmetries

in the peaks are accounted for by the centroid shift which take care of possible errors in angles calibration) and truncate the Hermite polynomials expansion just at the H_4 term. Therefore, all results presented in the next section (where not else specified) have been obtained by fitting the experimental response functions through the following expression:

$$F^{exp}(y,\chi) = \frac{\alpha}{\sqrt{2\pi\sigma^2}} e^{-u^2} \left[1 + c_4 \frac{2}{3} H_4(u)\right] \otimes R_n(y,\chi). \tag{7.8}$$

It has to be stressed that for a truncated expansion as in equation (7.8), where just the fourth Hermite polynomial is present, two interesting relations regarding the second, μ_2, and fourth moment, μ_4, of the distribution turn out. The second moment is indeed given by the square of the standard deviation, $\mu_2 = \sigma^2$, as in a simple Gaussian function and the first non Gaussian coefficient, c_4, is related to the fourth momentum of the distribution by:

$$c_4 = \frac{1}{64}\,\delta, \quad \delta = \frac{\mu_4 - 3\langle\mu_2^2\rangle^2}{\langle\mu_2^2\rangle^2} \tag{7.9}$$

where δ is the kurtosis of the single particle momentum distribution.

We want also to recall that the single particle mean kinetic energy, $\langle E_K\rangle$, is related to the second moment of the Compton profile, σ^2, via the equation 5.15:

$$\sigma^2 = \frac{2M}{3\hbar^2}\langle E_K\rangle. \tag{7.10}$$

7.2.2 Combined data analysis: water contribution

In the last part of the data analysis, results from hydrated and dry samples data sets have been combined, with the aim of deriving the response function associated to water protons only. One has to note that in DINS measurements, recoil peaks from different types of hydrogen do appear at the same time of flight and y range. Thus, within the incoherent approximation, one can express the response functions for hydrated samples in terms of hydrogens belonging to water and to silanol groups: hence, for each individual detector, $F_H^{exp}(y,2\theta)$ may be expressed as a weighted sum of these two components, $F_W^{exp}(y,2\theta)$ and $F_D^{exp}(y,2\theta)$:

$$F_H^{exp}(y,2\theta) = c\,F_D^{exp}(y,2\theta) + (1-c)\,F_W^{exp}(y,2\theta). \tag{7.11}$$

From this relation it follows, from the distributive property of convolution, that

$$J_H(y,2\theta) = c\,J_D(y,2\theta) + (1-c)\,J_W(y,2\theta), \tag{7.12}$$

with a second moment given by:

$$\sigma_H^2 = c\,\sigma_D^2 + (1-c)\,\sigma_W^2. \tag{7.13}$$

Pore diameter d (Å)	c obtained from fit (eq. (7.11)) %	c obtained from recoil peaks intensities and weight/volume ratio (see text) %
24	–	26
82	29± 2	31

Table 7.2: Values of the fraction of silanol/total hydrogens in the samples, c, obtained from a two lineshape fit as in equation (7.11) and from some considerations about theoretical densities of the samples, experimental weight/volume ratio and relative intensities of the hydrogen recoil peak with respect to the second peak due to silicon, aluminum and oxygen.

Subscripts W and D label hydrogen contributions associated to water and silanol groups; subscript H refers to all hydrogens together. The coefficient c represents the fraction of silanol/total hydrogens in the samples.

For both hydrated xerogel samples, experimental response functions, $F_H^{exp}(y, 2\theta)$ have been fitted, referring to equation (7.11), keeping $F_D^{exp}(y, 2\theta)$ lineshape fixed to the value obtained from the dry data sets analysis and with c, σ_W and c_{4W} (for $F_W^{exp}(y, 2\theta)$) as free parameters. This procedure allowed to reliably fit the hydrated spectra only for the xerogel with larger pore diameter (82 Å) while, in the case of the hydrated sample confined in smaller pore (24 Å), the fitting procedure did not allow to fit all parameters with sufficient accuracy. Therefore, in both cases, c has also been determined by combining information from the adsorbed water content and from spectra intensities, both by comparison of theoretical densities of the samples and experimental weight/volume ratio and from the relative intensities of the hydrogen recoil peak with respect to the second peak due to silicon, aluminum and oxygen. These approaches provide values of $c = 31\%$ for xerogel with average pore diameter $d = 24$ Å and $c = 26\%$ for $d = 82$ Å, as shown in table 7.2. Advancing the results of the combined fitting procedure, which will be illustrated in the next section, we report the value of the c coefficient obtained for the xerogel 82 Å: $c = 29\%$. It has to be noted that for higher pore diameter sample, values of c obtained in the two ways agree well with each other (see table 7.2).

We also stress that, if c, $F_D^{exp}(y, 2\theta)$ and $F_H^{exp}(y, 2\theta)$ are determined independently, $F_W^{exp}(y, 2\theta)$ can be reconstructed by inverting equation (7.11):

$$F_W^{exp}(y, 2\theta) = \frac{F_H^{exp}(y, 2\theta) - cF_D^{exp}(y, 2\theta)}{1 - c} \tag{7.14}$$

and then, by exploiting the relation (5.14) between the response function and the momentum distribution, one can calculate the "water proton" momentum distribution

$n_W(p)$ as:

$$n_W(p) = -\frac{1}{2\pi\hbar^3 y}\frac{d}{dy}J_W(y)|_{\hbar y=p}. \tag{7.15}$$

7.3 Results and discussion

In the following we present and discuss all the results obtained with the data analysis described in the previous sections. For all the samples (both dry and hydrated powders for both pore sizes) we have performed two distinct sets of fits. Presenting the results, we refer to *single fits* when we talk about fits performed on individual spectra (both at constant angle and momentum transfer); global results, in this case, are obtained through a weighted average of all the individual results. *Simoultaneous fits* refer to fits performed on the whole set of spectra by exploiting a unique model distribution function $J_{mdf}(y, 2\theta)$ (same σ and c_4 parameters for all scattering angles), convoluted with the individual resolution functions.

7.3.1 Hydrated and dry samples results

Examples of the results obtained from the single fits on the hydrated and dry samples for the powder with average pore size of 24 Å are reported in table 7.3 for six scattering angles. In figure 7.6, two examples of experimental spectra, for a scattering angle of 38.4 degrees, together with the resulting fitting function are reported, the first one, in the left panel, relative to the dry xerogel powder while the second one, in the right panel, corresponding to the hydrated sample.

In tables 7.4 and 7.5 are instead reported the results of all kind of fits performed on the xerogel with average pore diameter $d = 24\,\text{Å}$ and $d = 82\,\text{Å}$, respectively. Results relative to single fits at constant scattering angle and constant momentum transfer are obtained through a weighted average of the individual fit parameters.

From the previous two tables (7.4 and 7.5) we can note that the values of the quantities σ, $\langle E_K \rangle$ and c_4 are in quite good agreement within the statistical uncertainties. This feature demonstrates the internal consistency of the individual (both at constant scattering angle and at constant wavevector transfer) and simultaneous fitting procedures. Moreover, the simultaneous fits reduce the uncertainties in the whole set of physical quantities, allowing a more reliable lineshape analysis of both the response function and the momentum distribution function, with special regards for the non Gaussian components.

The third Hermite polynomial, $H_3(u)$, the first one needed to take into account the Final State Effects, does not modify appreciably the results and is not reported nor considered any more in the following data analysis. At the same time, the non Gaussian term c_4H_4 is the only term which needs to be included in the whole fitting procedures in order to reproduce the experimental data with good accuracy.

Single fits						
	Dry powder			Hydrated powder		
Angle deg	σ_D [Å^{-1}]	$\langle E_K\rangle_D$ [meV]	c_{4D} x 10^{-2}	σ_H [Å^{-1}]	$\langle E_K\rangle_H$ [meV]	c_{4H} x 10^{-2}
38.4	6.41±0.26	256±21	3.12±0.46	5.61±0.07	196±5	2.18±0.15
40.3	6.74±0.14	283±12	2.73±0.22	5.71±0.06	203±4	2.50±0.11
44.7	7.24±0.15	327±14	2.46±0.20	5.86±0.07	213±5	2.54±0.13
47.3	7.09±0.13	313±12	2.61±0.19	5.54±0.12	191±8	2.01±0.24
56.8	6.71±0.18	281±15	2.95±0.29	6.01±0.08	225±6	2.73±0.15
61.5	7.09±0.23	313±20	3.14±0.35	5.90±0.13	216±9	2.58±0.24

Table 7.3: Examples of results obtained from single fits of $F^{exp}(y,2\theta)$ data sets for both the dry (denoted by suffix D) and hydrated (denoted by suffix H) xerogel samples with average pore size of 24 Å. σ and $\langle E_K\rangle$ represent standard deviation of $n(p)$ and mean kinetic energy of the hydrogen atoms while c_4 is the coefficient of the fourth Hermite polynomial, as in equation (7.8).

	Dry powder			Hydrated powder		
	σ_D [Å^{-1}]	$\langle E_K\rangle_D$ [meV]	c_{4D} x 10^{-2}	σ_H [Å^{-1}]	$\langle E_K\rangle_H$ [meV]	c_{4H} x 10^{-2}
Single (2θ)	7.05±0.15	311±16	2.70±0.12	5.78±0.07	209±4	2.58±0.11
Simult (2θ)	6.90±0.05	296±5	2.87±0.08	5.95±0.03	221±2	2.81±0.05
Single (q)	6.73±0.07	282±5	2.98±0.12	5.81±0.03	210±2	2.90±0.06

Table 7.4: Results obtained from fits of $F^{exp}(y,2\theta)$ and $F^{exp}(y,\mathrm{q})$ data sets for both the dry (denoted by suffix D) and hydrated (denoted by suffix H) xerogel samples with average pore size of 24 Å. Both simultaneous and single fits (averaged) results are reported. σ and $\langle E_K\rangle$ represent standard deviation of $n(p)$ and mean kinetic energy of the hydrogen atoms while c_4 is the coefficient of the fourth Hermite polynomial, as in equation (7.8).

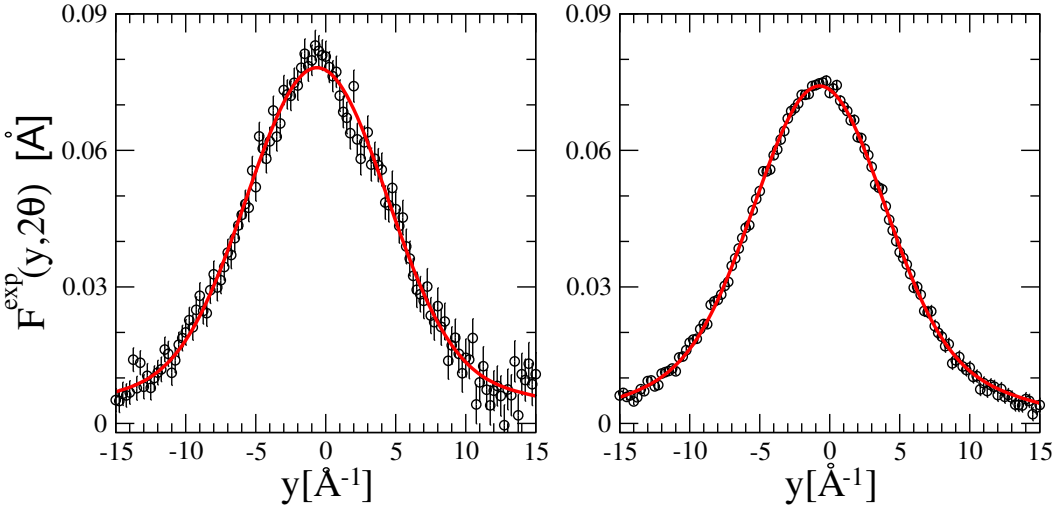

Figure 7.6: Examples of experimental spectra (circles with error bars) for dry (left panel) and hydrated (right panel) xerogel powders with average pore diameter $d = 24\,\text{Å}$, at a scattering angles of 38.4 degrees. The resulting fitting functions (red continuous line) are also shown.

A last comment regards the comparison of the results for the xerogel with pore size of 24 Å and 82 Å. Both the mean kinetic energy $\langle E_K \rangle$ and the fourth Hermite polynomial coefficient c_4 are higher for the smaller pore with respect to the larger one. The larger value of c_4, in particular, is an indication of a more pronounced non Gaussian character, with higher kurtosis, of the momentum distribution. Moreover, dry samples parameters are different for the two pore sizes, indicating a microscopic hydroxyl dynamics changing for different pore diameters.

7.3.2 Combined analysis results

In the last part of the work, a combined analysis of hydrated and dry samples data sets have been performed in order to derive the response function associated to water protons only. In section 7.2.2 we explained the methods exploited to obtain c, i.e. the fraction of silanol hydrogens with respect to the whole hydrogens in the samples. We said that for the powder with larger pores, the experimental response functions of the hydrated sample, $F_H^{exp}(y, 2\theta)$, have been fitted, referring to equation (7.11), keeping $F_D^{exp}(y, 2\theta)$ lineshape fixed to the value obtained from the dry data sets analysis (table 7.5, simultaneous fits results) and with c, σ_W and c_{4W} (for $F_W^{exp}(y, 2\theta)$) as free parameters. Results obtained with this fitting procedure are shown in the left part of

	Dry powder			Hydrated powder		
	σ_D [Å^{-1}]	$\langle E_K\rangle_D$ [meV]	c_{4D} x 10^{-2}	σ_H [Å^{-1}]	$\langle E_K\rangle_H$ [meV]	c_{4H} x 10^{-2}
Single (2θ)	6.56±0.35	267±29	2.40±0.60	5.46±0.42	185±29	1.56±0.71
Simult (2θ)	6.60±0.08	271±7	2.76±0.13	5.47±0.02	186±1	1.56±0.07
Single (q)	6.51±0.27	264±10	2.63±0.47	5.49±0.10	187±6	1.53±0.21

Table 7.5: Results obtained from fits of $F^{exp}(y,2\theta)$ and $F^{exp}(y,\mathrm{q})$ data sets for both the dry (denoted by suffix D) and hydrated (denoted by suffix H) xerogel samples with average pore size of 82 Å. Both simultaneous and single fits (averaged) results are reported. σ and $\langle E_K\rangle$ represent standard deviation of $n(p)$ and mean kinetic energy of the hydrogen atoms while c_4 is the coefficient of the fourth Hermite polynomial, as in equation (7.8).

From fit (see eq. (7.11))				From equations (7.13)		
d [Å]	c %	σ_W [Å^{-1}]	$\langle E_K\rangle_W$ [meV]	c %	σ_W [Å^{-1}]	$\langle E_K\rangle_W$ [meV]
24	–	–	–	31± 3	5.48 ± 0.06	187 ± 4
82	29± 2	4.94 ± 0.04	152 ± 3	26 ± 3	5.01 ± 0.04	156 ± 3
bulk [92]	–	4.87 ± 0.05	147 ± 3	–	4.87 ± 0.05	147 ± 3

Table 7.6: Values of σ_W and $\langle E_K\rangle_W$ relative to protons from confined water molecules, obtained from equation (7.13), (right part of the table) and by a two lineshape fit, referring to equation (7.11) (left part of the table). Last row reports value obtained from previous DINS measurements in bulk water [92].

table 7.6 together with values obtained by previous DINS measurements on bulk water [92], as a reference.

For both powders, c has also been determined through theoretical/experimental considerations (see section 7.2.2); within this approach we obtain values of $c = 31\%$ for xerogel with average pore diameter $d = 24$ Å and $c = 26\%$ for $d = 82$ Å. Exploiting the relations (7.13) and (7.14) and the results obtained for the hydrated and dry samples response functions (simultaneous fits results in tables 7.4 and 7.5), we are able to reproduce the response function of water hydrogens only, $J_W(y, 2\theta)$, and to calculate its second moment σ_W and kinetic energy, $\langle E_K\rangle_W$. These results are shown in the right part of table 7.6 together with values obtained by previous DINS measurements on bulk water [92], as a reference.

A plot of $\langle E_K\rangle_W$ values as a function of pore diameters is reported in figure 7.7, together with the value obtained from previous DINS experiments on bulk water [92].

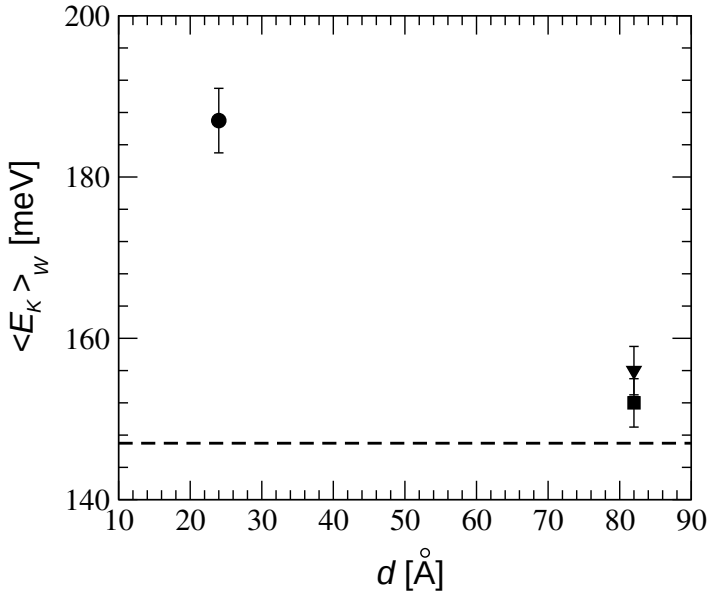

Figure 7.7: Kinetic energies of protons in water confined in xerogel matrices, $\langle E_K \rangle_W$, as a function of the pore diameter. The dashed line represents the value obtained from previous DINS experiments on bulk water [92].

From table 7.6 and figure 7.7 one can observe that the $\langle E_K \rangle_W$ values of water confined in xerogel matrices are always higher than in bulk water. In particular, for the smaller pore diameter sample, this value is about 40 meV higher than for bulk water. It is possible that the additional kinetic energy is largely due to the molecules near the surface being strongly bonded to the pore surface. In the smaller pores the fraction of water molecules interacting closely with the confining matrix surfaces is larger. One can estimate about 12% and 35% of water molecules "on the first adsorption layer" in pores with diameter of 82 Å, and 24 Å, respectively. Moreover we have just observed that both the kinetic energy, $\langle E_K \rangle_D$, and the second moment of the momentum distributions σ_D^2 of the dry samples are different for the two pore sizes. Thus the water proton dynamics of molecules close to the pore surface is modified by both geometrical effects of confinement and proximity to hydroxyl species of different microscopic dynamics.

7.3.3 Momentum distribution function and Born-Oppenheimer potential

In the last section, we noted that, if c, $F_D^{exp}(y, 2\theta)$ and $F_H^{exp}(y, 2\theta)$ are determined independently, $F_W^{exp}(y, 2\theta)$ and $J_W(y, 2\theta)$ can be reconstructed through equation (7.14). In this way, using values of tables 7.4 and 7.5 (results of simultaneous fits), we determined the water protons response functions, for both pore sizes.

Exploiting the relation between the response function and the momentum distribution (equation (5.14)), one can hence calculate the $n(p)$ for the protons in water confined in xerogel matrices. The resulting plots of spherical averages of the proton momentum distributions, $4\pi p^2 n(p)$, are shown in figure 7.8. Uncertainties in $n(p)$

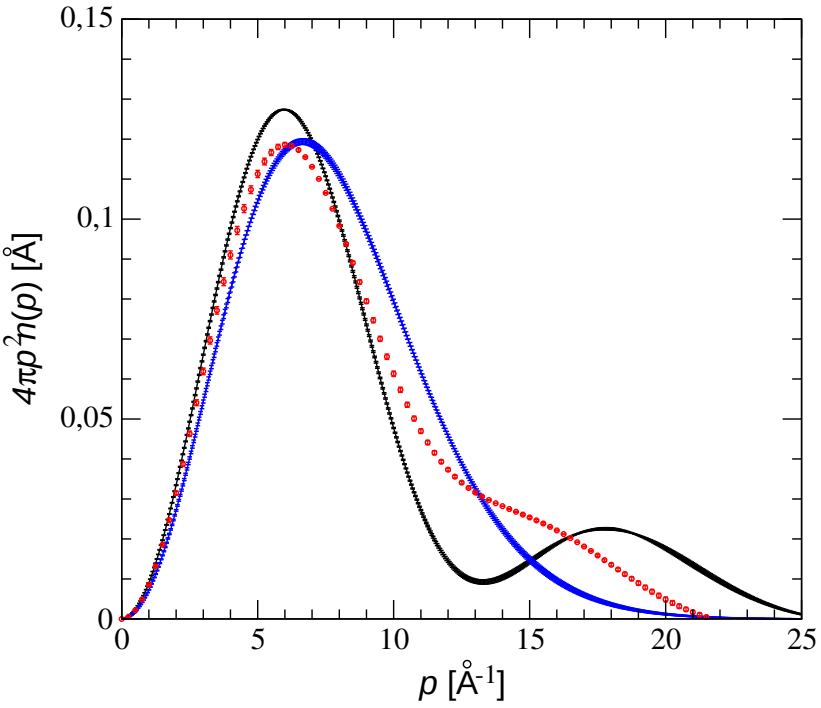

Figure 7.8: Spherical averages, $4\pi p^2 n(p)$, of the proton momentum distribution for water confined in xerogel matrices, for pore diameters of 24 Å (black line), 82 Å (red dotted line) and for bulk water (blue line, from [92]).

functions, $\sqrt{\langle \delta n(p)^2 \rangle}$, are obtained by the following expression [92]:

$$\langle \delta n(p)^2 \rangle = \sum_{i,j} \frac{\partial n(p)}{\partial \rho_i} \frac{\partial n(p)}{\partial \rho_j} \langle \delta \rho_i \delta \rho_j \rangle, \tag{7.16}$$

where ρ_i and ρ_j stand for fit parameters, $\frac{\partial n(p)}{\partial \rho_i}$ is the partial derivative of the momentum distribution relative to the *i-th* parameter, and $\langle \delta \rho_i \delta \rho_j \rangle$ is the element of the covariance matrix relative to *i-th* and *j-th* parameters.

From figure 7.8 it can be noticed that the momentum distribution of confined water differs substantially from that of bulk liquid. In particular, it can be observed that lineshapes narrow in the range 10 $\text{Å}^{-1} \div 15\,\text{Å}^{-1}$, and a second structure in the range 15 $\text{Å}^{-1} \div 20\text{Å}^{-1}$ develops. This behaviour is more evident for the smaller pore powder, with a minimum for $p \simeq 13\,\text{Å}^{-1}$ and a second maximum for $p \simeq 18\,\text{Å}^{-1}$. In this case, the bi-modal distribution suggests that changes in the local structure around protons occur, such as distortions of the hydrogen-bond network. These effects are related to the local proton potential (see also section 5.2.4).

We inferred the shape of this Born-Oppenheimer effective potential by fitting the momentum distribution with a model describing the motion along the bond by a wavefunction that corresponds in real space to two Gaussians separated by a distance δ [116]. When $\delta \neq 0$ one has an anisotropic momentum distribution given by:

$$n(p_x, p_y, p_z) = \frac{2cos^2(\frac{p_z \delta}{2\hbar})}{1 + e^{-\frac{\delta^2 \sigma_z^2}{2\hbar^2}}} \prod_i \frac{e^{-\frac{p_i^2}{2\sigma_i^2}}}{(2\pi\sigma_i)^{\frac{1}{2}}} \tag{7.17}$$

This lineshape has been spherically averaged and fitted using as fit parameters σ_z, δ and, for the transverse direction, $\sigma_x = \sigma_y$ [116]. In figure 7.9 we show the spherical average of the water proton momentum distribution together with the fit obtained from equation (7.17). From the figure we can observe that a good fit of momentum distribution is obtained with values of fitting parameters given by $\sigma_z = 8.67\,\text{Å}^{-1}$, $\sigma_x = \sigma_y = 4.12\,\text{Å}^{-1}$, and $\delta = 0.304\,\text{Å}$. Following section 5.2.4, the effective potential along the bond, that gives rise to this momentum distribution, has been calculated. In figure 7.10, this Born-Oppenheimer potential and the relative ground state wavefunction are shown, demonstrating clearly the bimodal nature of the ground state that leads to the oscillation seen in figure 7.8.

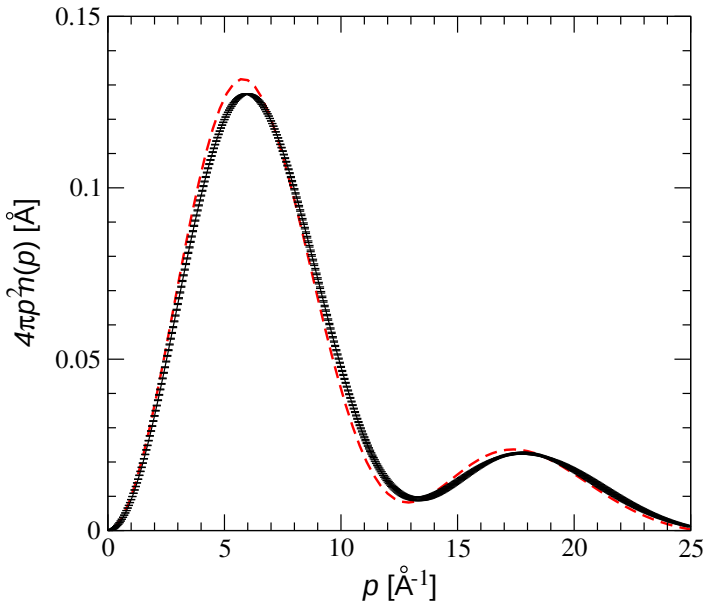

Figure 7.9: Water proton radial momentum distribution, $4\pi p^2 n(p)$, for water confined in xerogel matrices with average pore diameters $d = 24$ Å, obtained fitting the experimental data (continuous line with error bar) with a spherically averaged model function, as in equation (7.17) (dashed line).

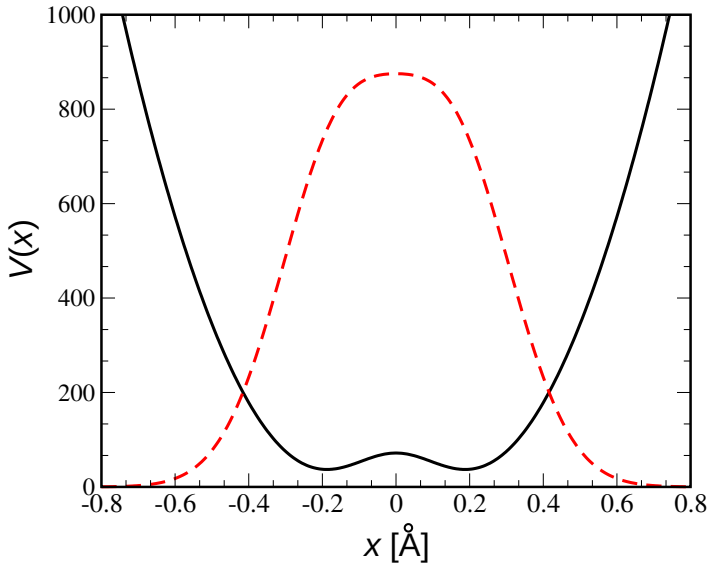

Figure 7.10: Effective single particle potential (continous line) and wave function (dashed line) for protons in water confined in xerogel matrices, for pore diameters $d = 24\,\text{Å}$.

Conclusions

Despite its apparent simplicity and its importance for biological, chemical and industrial processes and for the advancement in many research fields, liquid water still presents several anomalous and not fully understood properties. In the last years great effort has been devoted to the comprehension of structural and ground state properties of liquid water and to the study of water in various confined geometries such as in nanoporous systems, or in proximity of macromolecules and surfaces.

The present thesis work is based on the study of various properties of water faced with different investigative approaches: the excited state properties of liquid water, both electronic and optical, have been studied with *ab-initio* theoretical methods whereas the microscopic proton dynamics of confined water has been investigated with Deep Inelastic Neutron Scattering experiments.

Proton microscopic dynamics of confined water

DINS experiments on water confined in nanoporous xerogel powders with average pore diameter d of 24 Å and 82 Å have been performed on the inverse geometry spectrometer VESUVIO at the ISIS spallation neutron source. Both the hydrated and the dry samples have been measured.

After an accurate data reduction, the experimental spectra have been fitted using a general model distribution function given by a Gaussian lineshape multiplied by a truncated series of even Hermite polynomials, $H_n(x)$. The final state effects, which turn out at finite momentum transfer q, have been also accounted for through a series of powers of $1/q$.

The hydrated and dry samples have been first analyzed separately and the response functions of all the hydrogen atoms and of silanol-hydrogens alone have been obtained. Then the percentage of silanol-hydrogens with respect to the total number of hydrogens has been estimated and a combined analysis of dry and hydrated xerogel data sets has been performed in order to obtain information about water hydrogens only. For all the samples (both dry and hydrated powders for both pore sizes) we performed single fits on the individual spectra at constant scattering angle and at constat wavevector

transfer and simultaneous fits on the whole sets of spectra.

We determined the water protons response function and hence we calculated its momentum distribution; by fitting this momentum distribution we also inferred the shape of the local proton potential.

The main results and conclusions are now shortly recalled:

- just few terms in the expansion of the model response function have to be retained in order to obtain an accurate fit of the experimental spectra; in particular, we can neglect the final state effects and truncate the Hermite polynomials expansion just at the H_4 term. The fact that the longitudinal momentum distribution is well described by a non-gaussian lineshape reflects the anharmonic short-scale structure surrounding the protons.

- For what concerns the separated analysis of the hydrated and dry samples, both the mean kinetic energy $\langle E_K \rangle$ and the fourth Hermite polynomial coefficient c_4 are higher for the smaller pore sample with respect to the larger one. This is an indication of a more pronounced non Gaussian character, with higher kurtosis, of the momentum distribution. Moreover, dry samples parameters are different for the two pore sizes, indicating a microscopic hydroxyl dynamics changing for different pore diameters.

- Results regarding water hydrogens, both for the mean kinetic energy and for the c_4 coefficient, are always higher than in bulk water (for the smaller pore sample $\langle E_K \rangle$ is about 40 meV higher). This is partially due to the molecules near the surface, strongly bonded to the confining matrix, more numerous for the xerogel with pore diameter of 24 Å. Moreover, the proton dynamics of these molecules is modified both by geometrical effects of confinement and by proximity to hydroxyl species of different microscopic dynamics.

- The proton momentum distribution of confined water presents substantial differences from that of bulk water, especially for the smaller pore sample. In this case, a second structure evidently develops for $p \simeq 18 \text{Å}^{-1}$. This bi-modal distribution suggests that changes in the local structure around protons occur, such as distortions of the hydrogen-bond network, related to the local proton potential.

- The Born-Oppenheimer potential and the relative ground state wavefunction clearly confirm the bimodal nature of the ground state that leads to the oscillation in the momentum distribution.

The main conclusion is that the layers of water near the confining surface are strongly perturbed. This perturbation penetrates the entire pore in the smaller pore case, but is limited to a surface layer in the larger pore sample. The changes in

the water dynamics clearly depends on the interaction of water with the hydrophilic substrate but the nature of this interaction is still not clear.

Hydrogen bond network responds to impurities or disorder induced by confinement by developing effective double well potentials leading to coherent motions of protons in the two wells. We note that coherence has also been seen in water confined in carbon nanotubes at low temperatures [117] and for water on the surface of lysozime [118]. Evidently the coherence is developing in the surface layers.

In order to explore the nature of this surface layer and to achieve a better comprehension of the interaction between water and hydrophilic substrate, further experiments with lower hydration levels and hence lower coverage of the pore surface would be needed.

Excited state properties of liquid water

The electronic and optical properties of water have been studied with *ab-initio* theoretical methods. To simulate liquid water, that is a disordered system, instead of using a huge unit cell, we exploited several molecular dynamics snapshots in a smaller unit cell and averaged the results over these configurations. In particular, we used 20 configurations of 17 water molecules in a cubic unit cell with 15 a.u. side, obtained by classical molecular dynamics simulations.

The calculations have been performed on more steps. We started with DFT to obtain the Kohn-Sham eigenvalues and eigenvectors and the independent-particle (DFT-RPA) absorption spectrum. Then we corrected the energy levels using the Green's function perturbative approach, with the exchange-correlation self-energy calculated within the GW approximation. The third step consisted in the calculation of the optical absorption spectrum by solving the Bethe-Salpeter equation. We also tried less expensive calculation methods, such as Time Dependent-LDA and the RORO kernel, without success.

We now present the main results and conclusions.

- We averaged all our results over 20 molecular dynamics configurations and obtained good agreement with the experiments, both for what concerns the structural properties such as the radial distribution functions and regarding the excited state properties of water. Moreover, we found that the optical absorption spectrum of water is quite good already averaging over just five snapshots.

- Looking at the energy loss spectrum of water, we obtained really good agreement for what concerns the peak position and lineshape, already at the independent-particles DFT level; anyway, in the low energy region of the spectrum, where excitonic effects are more important, the agreement is less satisfactory as expected.

- The electronic gap, defined as the difference between the energy levels of the HOMO and LUMO, averaged over both the 8 k-points and the 20 molecular dynamics snapshots, turns out to be 5.09 eV within DFT-GGA, in good agreement with previous DFT calculations [1] but strongly underestimating the experimental gap (8.7 $\pm$ 0.5 eV [81]). GW corrections open the gap up to 8.4 eV, well within the experimental range [81].

- The optical absorption spectrum calculated at the independent-particles DFT level does not compare in a satisfactory way with the experimental one. GW corrections, in this case, do not improve the agreement, since their effect is just to shift the spectrum towards higher energies. In order to obtain a good absorption spectrum it has been necessary to include the electron-hole interaction through the solution of the Bethe-Salpeter equation. We observed that dramatic many-body effects are present in water and the first absorption peak is due to a strongly bound exciton with a binding energy of 2.4 eV. Time dependent-DFT, both with the ALDA and with the RORO exchange and correlation kernels, is not able to reproduce the experimental spectrum.

- GW corrections turned out to be almost independent with respect to the molecular dynamics configuration and it has been possible to calculate them just for one snapshot.

- We found that also the optical absorption spectrum is not so much sensible to screening details and therefore the spectra of the various molecular dynamics snapshots could be calculated using always the same screening function.

- Also a constant screening works well, giving an optical absorption spectrum almost identical to the one calculated with the full screened electron-hole interaction.

This work is the first study of excited state properties of a liquid system with *ab-initio* methods, beyond simple DFT. The main idea, which has allowed such kind of calculation, has been to average the results over many "small" unit cell configurations instead of exploiting a huge unit cell.

Our findings concerning the stability of GW and Bethe-Salpeter calculations with respect to the configuration may have important consequences on future calculations for water (and maybe for other liquids), since the ab-initio evaluation of the dynamical dielectric matrix is the real bottleneck of many-body calculations, and its evaluation for many different snapshots makes this approach too cumbersome for becoming a state of the art method. Hence, to be able to determine accurate optical spectra for many configurations using the same dielectric constant to screen the electron-hole interaction, will enormously speed up future calculations.

The main perspective in this field is the study of excited state properties of aqueous solutions of biological interest, since biological systems live in solution and not in vacuum. Solvent shifts, fluorescent proteins and rhodopsin photo-cycle are just few examples of possible future applications of these methods.

Acknowledgments

Molte sono le persone che sento di dover ringraziare per essermi state vicine, in vari modi e a vario titolo, in questi tre anni di dottorato.

I maggiori ringraziamenti vanno ai miei quattro relatori interni che mi hanno assistito per tutto il tempo con pazienza e disponibilitá e sopratttutto con amicizia: Carla Andreani, Rodolfo Del Sole, Olivia Pulci e Roberto Senesi.

Molto utili sono state anche le collaborazioni con Silvia Imberti, Antonino Pietropaolo, Michele Cascella, David Fernandez Cañoto e George Reiter.

Un grande ringraziamento per tante interessanti discussioni, scientifiche e non solo, va a Margherita Marsili, Mauro Bruno, Letizia Chiodo, Fabrizio De Fausti, Conor Hogan e Claudia Pantalei.

Un grazie particolare va anche a Carlo Cavazzoni che con la sua grande disponibilitá e gentilezza ha risolto vari problemi che si sono presentati con la gestione del mio acccount presso il CINECA.

Ultimi, ma non per importanza, i ringraziamenti per le persone che piú mi vogliono bene.
Mio marito Andrea che mi é sempre stato vicino, mi ha incoraggiata nei momenti di insicurezza e ha sopportato pazientemente i momenti di maggiore stress.
I miei genitori che non hanno mai dubitato delle mie possibilitá e nell'ultimo periodo, insieme ai miei suoceri, mi hanno aiutato nella gestione familiare.
Sara e Lorenzo che, poco interessati alla fisica, hanno ascoltato con pazienza il mio primo seminario in inglese e hanno provato a leggere qualche pagina di questa tesi.
Gli altri amici piú cari, con i quali ho potuto rilassarmi, giocare e stare in allegria.
Infine Silvia e il nascituro Leonardo che in pochi mesi sono riusciti a stravolgere completamente la mia vita, diventarne il centro assoluto e riempirla di tantissima felicitá.

GRAZIE

****

The theoretical work has been supported by the EU's 6th Framework Programme through the NANOQUANTA NoE (NMP4-CT-2004-500198). I also acknowledge MIUR for financial support (NANOSIM and PRIN2005), and INFM for CINECA cpu time.

The experimental work has been supported within the CNR-CCLRC Agreement No. 01/9001 concerning collaboration in scientific research at the spallation neutron source ISIS.

Bibliography

[1] K. Laasonen, M. Sprik, M. Parrinello, and R. Car, J. Chem. Phys. **99**, 9080 (1993).

[2] O. Christiansen, T. M. Nymand, and K. V. Mikkelsen, J. Chem. Phys. **113**, 8101 (2000).

[3] J. C. Grossman, E. Schwegler, E. W. Draeger, F. Gygi, and G. Galli, J. Chem. Phys. **120**, 300 (2004).

[4] M. E. Tuckerman, K. Laasonen, M. Sprik, and M. Parrinello, J. Phys.: Condens. Matter **6**, A93 (1994).

[5] H. Sato and F. Hirato, J. Chem. Phys. **111**, 8545 (1999).

[6] P. L. Silvestrelli and M. Parrinello, J. Chem. Phys. **111**, 3572 (1999).

[7] B. Chen, I. Ivanov, M. L. Klein, and M. Parrinello, Phys. Rev. Lett. **91**, 215503 (2003).

[8] P. Raitieri, A. Laio, and M. Parrinello, Phys. Rev. Lett. **93**, 087801 (2004).

[9] L. Bernasconi, J. Blumberger, M. Sprik, and R. Vuilleumier, J. Chem. Phys. **121**, 11885 (2004).

[10] D. Prendergast, J. C. Grossman, and G. Galli, J. Chem. Phys. **123**, 014501 (2005).

[11] R. Zangi, J. Phys.: Condens. Matter **16**, S5371 (2004).

[12] L. D. Gelb, K. E. Gubins, R. Radhakrishnan, and M. S. Bartkoviak, Rep. Prog. Phys. **61**, 1573 (1999).

[13] F. Bruni, M. A. Ricci, and A. K. Soper, J. Chem. Phys. **109**, 1478 (1998).

[14] F. Venturini, P. Gallo, M. A. Ricci, A. R. Bizzarri, and S. Cannistraro, J. Chem. Phys. **114**, 10010 (2001).

[15] V. Crupi, D. Majolino, P. Migliardo, and V. Venuti, J. Phys. Chem. B **106**, 10884 (2002).

[16] S. Mitra, R. Mukhopadhyay, I. Tsukushi, and S. Ikeda, J. Phys.: Condens. Matter **13**, 8455 (2001).

[17] A. Cupane, V. Levantino, and M. G. Santangelo, J. Phys. Chem. B **106**, 11323 (2002).

[18] A. Scodinu and J. T. Fourkas, J. Phys. Chem. B **106**, 10292 (2002).

[19] U. Raviv and J. Klein, Nature **413**, 51 (2001).

[20] U. Raviv, S. Giasson, J. Frey, and J. Klein, J. Phys.: Condens. Matter **14**, 9275 (2002).

[21] E. Spohr, C. Hartnig, P. Gallo, and M. Rovere, Journal of Molecular Liquids **80**, 165 (1999).

[22] P. Gallo, M. Rovere, and E. Spohr, Phys. Rev. Lett. **85**, 4317 (2000).

[23] P. Gallo, M. Rovere, and E. Spohr, J. Chem. Phys. **113**, 11324 (2000).

[24] L. H. Thomas, Proc. Cambridge Phil. Soc. **23**, 542 (1927).

[25] E. Fermi, Z. Phys. **48**, 73 (1928).

[26] P. Hohenberg and W. Kohn, Phys. Rev. B **13**, 864 (1964).

[27] W. Kohn and L. J. Sham, Phys. Rev. A **140**, 1113 (1965).

[28] R. M. Dreizler and E. K. U. Gross, *Density Functional Theory* (Springer Verlag Heidelberg, Berlin, 1990).

[29] M. Born and J. M. Oppenheimer, Ann. Phisyk **84**, 457 (1927).

[30] D. R. Hartree, Proc. Cambridge Phil. Soc. **24**, 89 (1928).

[31] V. Fock, Z. Phys. **61**, 126 (1930).

[32] E. H. Lieb, Int. J. Quant. Chem. **24**, 243 (1983).

[33] D. C. Langreth and J. P. Perdew, Phys. Rev. B **21**, 5469 (1980).

[34] J. P. Perdew, J. A. Chevary, S. H. Vosko, K. A. Jackson, M. R. Pederson, D. J. Singh, and C. Fiolhais, Phys. Rev. B **46**, 6671 (1992).

[35] D. M. Ceperley and B. J. Alder, Phys. Rev. Lett. **45**, 566 (1980).

[36] J. P. Perdew and A. Zunger, Phys. Rev. B **23**, 5048 (1981).

[37] J. P. Perdew, Phys. Rev. Lett. **55**, 1665 (1985).

[38] O. Gunnarsson, M. Jonson, and B. I. Lundqvist, Phys. Rev. B **20**, 3136 (1979).

[39] N. W. Ashcroft and N. D. Mermin, *Solid state physics* (Saunders college publishing, Orlando, 1976).

[40] A. Baldereschi, Phys. Rev. B **7**, 5212 (1973).

[41] R. Mokov, G. Shah and M. C. Payne, Phys. Rev. B **53**, 15513 (1996).

[42] E. Fermi, Il nuovo cimento **11**, 157 (1934).

[43] J. C. Phillips and L. Kleinman, Phys. Rev. **116**, 287 (1959).

[44] D. R. Hamann, M. Schlüter, and C. Chiang, Phys. Rev. Lett. **43**, 1494 (1979).

[45] S. Goedeker, M. Teter, and J. Hutter, Phys. Rev. B **54**, 1703 (1996).

[46] V. Olevano and L. Reining, Phys. Rev. Lett. **86**, 5962 (2001).

[47] A. A. Abrikosov, L. P. Gorkov, and I. E. Dzyaloshinski, *Methods of Quantum Field Theory in Statistical Physics* (Courier Dover Publications, Dover, 1975).

[48] L. D. Landau and E. M. Lifšits, *Fisica Statistica, teoria dello stato condensato* (Editori Riuniti, Roma, 1981).

[49] G. Onida, L. Reining, and A. Rubio, Rev. Mod. Phys. **74**, 601 (2002).

[50] B. Farid, *Electron Correlation in the Solid State* (N.H. March, Imperial College Press, Oxford, 1999).

[51] L. Hedin, Phys. Rev. **139**, A796 (1965).

[52] L. Hedin and S. Lundqvist, Solid state Phys. **23**, 1 (1969).

[53] M. S. Hybertsen and S. G. Louie, Phys. Rev. Lett. **55**, 1418 (1985).

[54] M. S. Hybertsen and S. G. Louie, Phys. Rev. B **34**, 5390 (1986).

[55] O. Pulci, F. Bechstedt, G. Onida, R. Del Sole, and L. Reining, Phys. Rev. B **60**, 16758 (1999).

[56] M. Rohlfing and S. G. Louie, Phys. Rev. B **62**, 4297 (2000).

[57] R. W. Godby and R. J. Needs, Phys. Rev. Lett. **62**, 1169 (1989).

[58] M. Marsili, PhD Thesis, University of Rome, Tor Vergata .

[59] R. Del Sole, L. Reining, and R. W. Godby, Phys. Rev. B **49**, 8024 (1994).

[60] S. L. Adler, Phys. Rev. **126**, 413 (1962).

[61] N. Wiser, Phys. Rev. **129**, 62 (1963).

[62] E. Runge and E. K. U. Gross, Phys. Rev. Lett. **52**, 997 (1984).

[63] E. K. U. Gross, J. F. Dobson, and M. Petersilka, *Density functional theory* (Springer, New York, 1996).

[64] R. van Leeuwen, Int. J. Mod. Phys. B **15**, 1969 (2001).

[65] L. Reining, V. Olevano, A. Rubio, and G. Onida, Phys. Rev. Lett. **88**, 066404 (2002).

[66] S. Botti, F. Sottile, N. Vast, V. Olevano, L. Reining, H. C. Weissker, A. Rubio, G. Onida, R. Del Sole, and R. W. Godby, Phys. Rev. B **69**, 155112 (2004).

[67] R. Del Sole, O. Pulci, V. Olevano, and A. Marini, Phys. stat. sol. b **242**, 2729 (2005).

[68] G. Adragna, R. Del Sole, and A. Marini, Phys. Rev. B **68**, 165108 (2003).

[69] F. Sottile, V. Olevano, and L. Reining, Phys. Rev. Lett. **91**, 056402 (2003).

[70] A. Marini, R. Del Sole, and A. Rubio, Phys. Rev. Lett. **91**, 256402 (2003).

[71] W. L. Jorgensen, J. Chandrasekhar, J. D. Madura, R. W. Impey, and M. L. Klein, J. Chem. Phys. **79**, 926 (1983).

[72] S. J. Nosé, J. Chem. Phys. **81**, 511 (1984).

[73] W. G. Hoover, Phys. Rev. **31**, A1695 (1985).

[74] A. K. Soper, F. Bruni, and M. A. Ricci, J. Chem. Phys. **106**, 247 (1997).

[75] M. Bockstedte, A. Kley, J. Neugebauer, and M. Scheffler, Comput. Phys. Comm. **107**, 187 (1997).

[76] J. P. Perdew and Y. Wang, Phys. Rev. B **33**, 8800 (1986).

[77] G. D. Kerr, R. N. Hamm, M. W. Williams, R. D. Birkoff, and L. R. Painter, Phys. Rev. A **5**, 2523 (1972).

[78] L. R. Painter, R. N. Hamm, E. T. Arakawa, and R. D. Birkoff, Phys. Rev. Lett. **21**, 282 (1968).

[79] R. Haydock, Comput. Phys. Comm. **20**, 11 (1980).

[80] P. H. Hahn, W. G. Schmidt, K. Seino, M. Preuss, F. Bechstedt, and J. Bernholc, Phys. Rev. Lett. **94**, 037404 (2005).

[81] A. Bernas, C. Ferradini, and J. P. Jay-Gerin, Chem. Phys. **222**, 151 (1997).

[82] H. Hayashi, N. Watanabe, Y. Udagawa, and C. C. Kao, J. Chem. Phys. **108**, 823 (1997).

[83] M. A. Elliot and R. J. Kanehisa, Phys. Rev. B **35**, 2228 (1987).

[84] K. Kobayashi, J. Phys. Chem. **4317**, 2228 (1983).

[85] P. C. Hohenberg and P. M. Platzmann, Phys. Rev. **152**, 198 (1966).

[86] G. K. Ivanov and Y. S. Sayasov, Usp. Fiz. Nauk. **90**, 47 (1966).

[87] G. K. Ivanov and Y. S. Sayasov, Soviet Phys. Uspekhi **9**, 670 (1967).

[88] S. W. Lovesey, *Theory of thermal neutron scattering from condensed matter* (Clarendon Press, Oxford, 1987).

[89] G. I. Watson, J. Phys.: Condens. Matter **8**, 5955 (1996).

[90] G. B. West, Phys. Rep. **18C**, 263 (1975).

[91] G. Reiter, J. Mayers, and J. Noreland, Phys. Rev. B **65**, 104305 (2002).

[92] C. Andreani, D. Colognesi, J. Mayers, G. F. Reiter, and R. Senesi, Advances in Physics **54**, 377 (2005).

[93] V. F. Sears, Phys. Rev. B **30**, 44 (1984).

[94] R. Silver and G. F. Reiter, Phys. Rev. B **35**, 3647 (1987).

[95] J. Mayers, C. Andreani, and G. Baciocco, Phys. Rev. B **39**, 2022 (1989).

[96] G. Reiter and R. Silver, Phys. Rev. Lett. **54**, 1047 (1985).

[97] T. Broome, private communication .

[98] C. G. Windsor, *Pulsed neutron scattering* (Taylor and Francis, London, 1981).

[99] R. M. Brugger, A. D. Taylor, C. E. Olsen, J. A. Goldstone, and A. K. Soper, Nucl. Instr. and Meth. **221**, 393 (1984).

[100] M. Tardocchi, A. Pietropaolo, C. Andreani, A. Bracco, A. D'Angelo, G. Gorini, S. Imberti, R. Senesi, N. J. Rhodes, and E. M. Schooneveld, Nucl. Instr. and Meth. A **526**, 477 (2004).

[101] R. Senesi, C. Andreani, Z. Bowden, D. Colognesi, E. De Giorgi, A. L. Fielding, J. Mayers, M. Nardone, J. Norris, M. Praitano, N. J. Rhodes, W. G. Stirling, J. Tomkinson, and C. Uden, Physica B **200**, 276 (2000).

[102] C. Andreani, A. Pietropaolo, R. Senesi, G. Gorini, M. Tardocchi, A. Bracco, N. J. Rhodes, and E. M. Schooneveld, Nucl. Instr. and Meth. A **481**, 509 (2002).

[103] C. Andreani, D. Colognesi, E. De Giorgi, A. Filabozzi, M. Nardone, and E. Pace, Nucl. Instr. and Meth. A **497**, 535 (2003).

[104] C. Andreani, G. Baciocco, R. S. Holt, and J. Mayers, Nucl. Instr. and Meth. A **276**, 297 (1989).

[105] C. J. Brinker and G. W. Scherer, *Sol-Gel Science: The Physics and Chemistry of Sol-Gel Processing* (Academic Press, San Diego, 1990).

[106] D. Fernandez-Cañoto, European Ph.D. Thesis, University of Vigo (Spain), University of Rome Tor Vergata (Italy) .

[107] S. Brunauer, P. H. Emmett, and E. Teller, J. Am. Chem. Soc. **60**, 309 (1938).

[108] A. Pietropaolo, Ph.D. Thesis, University of Rome Tor Vergata (Italy) .

[109] A. L. Fielding and J. Mayers, Nucl. Instr. and Meth. A **480**, 680 (2002).

[110] J. Mayers, A. L. Fielding, and R. Senesi, Nucl. Instr. and Meth. A **481**, 454 (2002).

[111] K. H. Andersen, W. G. Stirling, R. Scherm, A. Stunault, B. Fak, H. Godfrin, and A. J. Dianoux, J. Phys.: Condens. Matter **6**, 821 (1994).

[112] C. Andreani, E. De Giorgi, R. Senesi, F. Cilloco, D. Colognesi, J. Mayers, M. Nardone, and E. Pace, J. Chem. Phys. **114**, 387 (2001).

[113] A. Pietropaolo, C. Andreani, A. Filabozzi, R. Senesi, G. Gorini, E. Perelli-Cippo, M. Tardocchi, N. J. Rhodes, and E. M. Schooneveld, Journal of Instrumentation **1**, P04001 (2006).

[114] C. Andreani, D. Colognesi, E. De Giorgi, and M. A. Ricci, J. Chem. Phys. **115**, 11243 (2001).

[115] V. F. Sears, Phys. Rev. **185**, 200 (1969).

[116] G. F. Reiter, J. C. Li, J. Mayers, T. Abdul-Redah, and P. Platzman, Brazilian Journal of Physics **34**, 142 (2004).

[117] G. Reiter, D. Homouz, C. Burnham, P. Platzman, J. C. Li, and A. Kolesnikov, to be published in Phys. Rev. Lett .

[118] R. Senesi, A. Pietropaolo, A. Bocedi, S. E. Pagnotta, and F. Bruni, submitted to Phys. Rev. Lett .